Investigations of the $Al_{1-x}Ga_xFeO_3$ family and other oxide materials

A thesis submitted in partial fulfillment

for the degree of

𝔐𝔞𝔰𝔱𝔢𝔯 𝔬𝔣 𝔖𝔠𝔦𝔢𝔫𝔠𝔢

as a part of the

MS - Ph. D. Programme

(Chemical Science)

by

Ajmala Shireen P.

New Chemistry Unit

Jawaharlal Nehru Centre for Advanced Scientific Research

(A Deemed University)

Bangalore, India
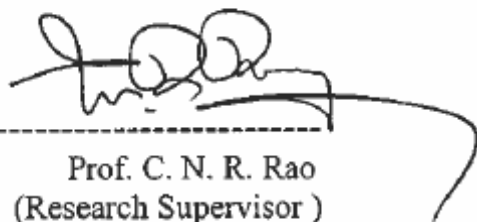
March 2012

DECLARATION

I hereby declare that the matter embodied in this thesis entitled **"*Investigations of the $Al_{1-x}Ga_xFeO_3$ family and other oxide materials*"** is the result of investigations carried out by me under the supervision of Prof. C. N. R. Rao, FRS at the New Chemistry Unit, JNCASR, Bangalore, India and that it has not been submitted elsewhere for the award of any degree or diploma.

Keeping with the general practice in reporting scientific observations, due acknowledgement has been made wherever the work described is based on the findings of other investigators.

Ajmala Shireen P.

CERTIFICATE

I hereby certify that the matter embodied in this thesis entitled **"Investigations of the Al$_{1-x}$Ga$_x$FeO$_3$ family and other oxide materials"** has been carried out by Ms. Ajmala Shireen P. at the New Chemistry Unit, Jawaharlal Nehru Centre for Advanced Scientific Research, Bangalore, India under my supervision and it has not been submitted elsewhere for the award of any degree or diploma.

Prof. C. N. R. Rao

(Research Supervisor)

Acknowledgements

PREFACE

This thesis covers studies of different aspects of the chemistry of materials. Part 1 mainly focuses on exploring the multiferroic nature of various oxides. Multiferroics are technologically quite important as there is a co-existence of more than one ferroic property in them. Part 2 deals with size effects in ferroelectrics and Part 3 with transparent conducting oxides. Final sections of this thesis, namely Part 4 and Part 5, discusses ongoing work and other works done by the author, respectively. The thesis is hence divided into five parts.

Part 1 comprises a study of structure, magnetism, multiferroic and magnetoelectric properties of $Al_{1-x}Ga_xFeO_3$ family of oxides. Our study establishes the structure and magnetic features of these oxides and shows them to be multiferroic and magnetoelectric at low temperatures. Spin-phonon coupling along with anti-site disorder is suggested to be responsible for the interesting properties exhibited by these oxides. Ball milling of these oxides unravelled interesting phase transitions stabilizing metastable phases at room temperature. Mn^{3+} ions when doped into specific sites of $GaFeO_3$ showed different signatures in magnetic properties. The magnetic transition temperature could also be raised to a temperature above room temperature by increasing the Fe content in $Al_{1-x-y}Ga_xFe_{1+y}O_3$. Interestingly all these oxides are ferroelectric.

Part 2 deals with the dielectric properties of narrow $BaTiO_3$ nanotubes. The effect of 1-dimensional confinement on the dielectric (ferroelectric) properties of $BaTiO_3$ nanotubes were studied here both experimentally and theoretically. This study has shown that ferroelectricity at room temperature is suppressed in nanotubes

when the wall thickness is below a critical limit. Instead we observe unusual dielectric transitions.

Part 3 consists of a study of transparent conducting oxides (TCOs). Here Ge^{4+} doping was done in various oxides like In_2O_3, Ga_2O_3 and $Ga_{1.4}In_{0.6}O_3$ aiming to make these host oxides transparent and conducting. This attempt was quite successful in Ge-doped In_2O_3 which turned out to be a potential TCO with conductivity values comparable to that of tin doped indium oxide (ITO).

Part 4 deals with the ongoing work and is subdivided into two sections. Section 4.1 deals with anion doping of ZnO to make it a potential photochemical catalyst. Preliminary studies shows that the band edge gets red shifted on anion doping. Further studies are in progress to improve and confirm the obtained results. Section 4.2 deals with magnetic and dielectric studies of $EuZrO_3$. Magnetic studies revealed it to be an antiferromagnet with interesting co-existence of ferromagnetism and antiferromagnetism as shown by a positive Weiss constant. Dielectric and magnetoelectric properties of this oxide are yet to be explored.

Part 5 gives a glimpse of other works done. The paper discusses the synthesis of highly pure inorganic nanoparticles using fluorous chemistry in a single step.

Contents

PART - I

Investigations of the Al$_{1-x}$Ga$_x$FeO$_3$ family of oxides: Structure, Phase transitions, Magnetic and Dielectric properties

*Summary**

Multiferroics have been a subject of great scientific interest in this century as various non-conventional phenomena uncovers to combine magnetism and ferroelectricity which are conventionally thought of to be mutually exclusive. In this regard, detailed studies of Al$_{1-x}$Ga$_x$FeO$_3$ family of oxides have been carried out to explore their multiferroic and magnetoelectric behavior. Al$_{1-x}$Ga$_x$FeO$_3$ family of oxides crystallizes in a non-centrosymmetric space group (*Pna2$_1$*).

These were investigated in detail along with structural aspects by employing X-ray and neutron diffraction techniques. These oxides are ferrimagnetic in nature and display interesting dielectric properties. Magnetic field is found to have profound effect on the dielectric properties. Magnetodielectric effect reaches a value of about 60 % in Al$_{0.5}$Ga$_{0.5}$FeO$_3$.

Pyroelectric studies have shown these oxides to be ferroelectric at lower temperature with substantial amount of magnetoelectric coupling. Raman studies reveal strong spin – phonon coupling in the system. First-principles density functional theory based calculations performed by Prof. U. V. Waghmare *et. al.*

show that magnetic ordering and related properties in these oxides are due to anti-site disorder at the cation sites. The origin of ferroelectricity and tendency of cations to disorder can be traced to their local structure and ionic sizes.

Ball milling of $Al_{1-x}Ga_xFeO_3$ (x = 0.0, 0.5) oxides displayed occurrence of interesting phase transitions stabilizing metastable phases. $AlFeO_3$ first transforms itself to $P2_12_12_1$ phase and then to $R\text{-}3c$ phase whereas $Al_{0.5}Ga_{0.5}FeO_3$ directly to $R\text{-}3c$ phase on milling. Thus metastable phases in turn depends on the nature of the A-site cation present as well as their concentration. $Al_{1-x}Ga_xFeO_3$ (x = 1) have been doped with Mn^{3+} ions site specifically and their magnetic properties were investigated. As Mn^{3+} is introduced to different sites, magnetic interaction that it effects differs and this had distinct signatures in the magnetic data. In an attempt to increase the magnetic transition temperature, Fe^{3+} content in these oxides were increased and a new family, $Al_{1-x-y}Ga_xFe_{1+y}O_3$, was explored. These oxides had raised the magnetic transition temperature above room temperature and also show ferroelectricity at lower temperatures.

1.1. Multiferroics and Magnetoelectrics - An Introduction

Multiferroics are materials in which more than one ferroic order is present simultaneously[1,2]. Ferroic properties are those properties which spontaneously order with an applied field and are switchable. These ferroic properties can be ferromagnetic if the material order magnetically under an applied magnetic field, it can be ferroelectric if it orders electrically under an applied electric field it can also be ferroelastic if stress can induce a reversible deformation in these materials. When any of these or their corresponding antiferroic properties co-exist in a material, they are termed *multiferroic* [1]. These materials are quite important from the technological point of view as they serves quite promising for use in memory devices, recording etc. and also equip us with an extra degree of freedom to tune the properties.

1.1.1. Magnetic Materials

The first magnetic material known to mankind was loadstone (magnetite, Fe_3O_4)[3]. The discovery of this dates back to 600 B.C. Magnetic materials are classified differently based on their response to magnetic field. If these materials repel the external field then they are termed *diamagnetic materials*[4]. These materials normally have filled atomic orbitals like in He, Ne, Ar etc. Materials whose moments

are randomly oriented but tend to align in the direction of the field when an external magnetic field is applied are called **paramagnetic materials** (Fig.1.1.1). These materials tend to possess unpaired electrons which interact with the applied field. According to Curie -Weiss Law, in a paramagnetic material, susceptibility is inversely proportional to temperature.

$$\chi = \frac{C}{T - \theta}$$

where C is called Curie's constant and θ the Weiss constant. θ is zero for a paramagnetic material but depending on the direction in which the molecular field interacts with the applied field it can take positive or negative values.
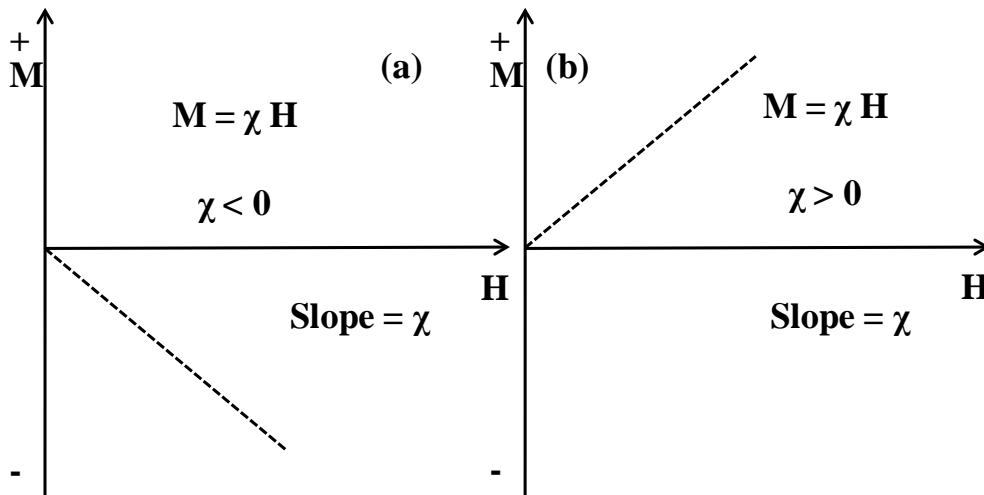
Fig.1.1.1: Variation of magnetization v/s magnetic field a) diamagnetic material b) paramagnetic material.

There is yet another class of compounds in which moments are coupled to each other through exchange forces. These materials exhibit magnetic domain structures. Magnetization will be uniform within each domain. Several of these domains arrange randomly giving a net zero magnetization in the absence of an external magnetic field. But when magnetic field is applied they tend magnetize spontaneously reaching a maximum value called saturation magnetization (M_s). Even after the removal of the field, these materials tend to retain the memory of the

applied field, which is called the remanant magnetization (M$_R$). These materials hence display a hysteretic behavior in an applied field. At very high temperature exchange forces are overcome by thermal fluctuations and hence these materials behave paramagnetically above T$_c$. These materials known as **ferromagnetic materials** (Fig.1.1.2) are characterized by a positive Weiss constant.
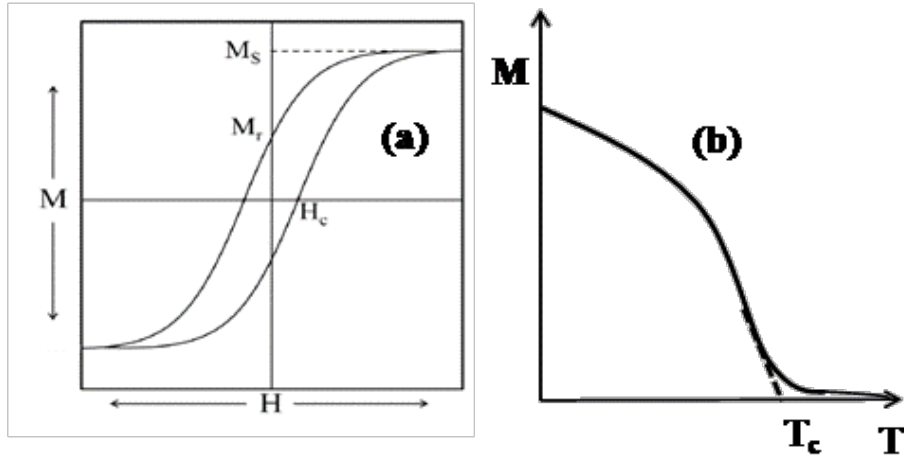
Fig.1.1.2: a) Hysteresis loop and b) Variation of magnetization as a function of temperature for a typical ferromagnetic material.

There are some materials in which neighboring domains are arranged anti-parallel to each other giving rise to a net zero magnetic moment. These are called **anti-ferromagnetic materials** (Fig.1.1.3). These materials are magnetically ordered below T$_N$ and behave paramagnetically above this temperature with a negative Weiss constant.
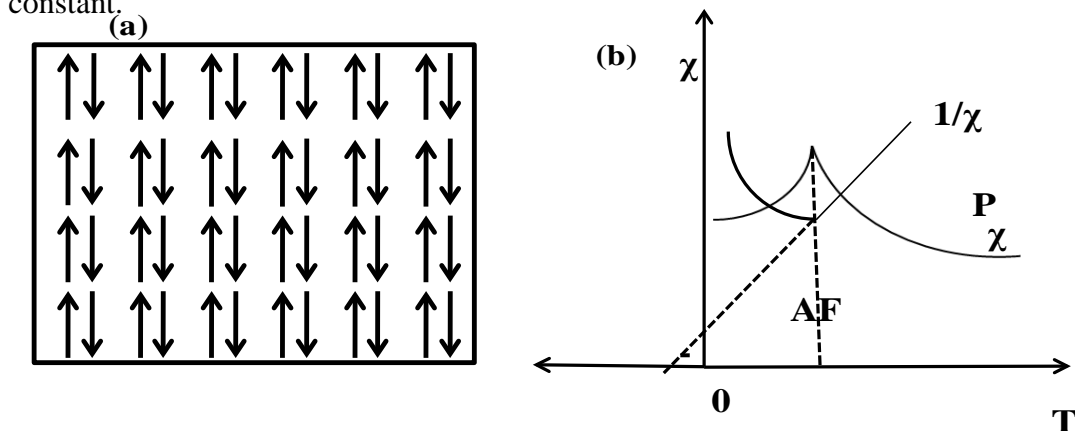
Fig.1.1.3: a) Arrangements of magnetic moments and b) Variation of susceptibility and inverse susceptibility with temperature for an antiferromagnetic material

If the moments in the oppositely aligned sub lattices are unequal then a weak ferromagnetic like behavior remains. These materials are called ***ferrimagnetic materials*** (Fig.1.1.4) and are similar to ferromagnetic materials in all respects.
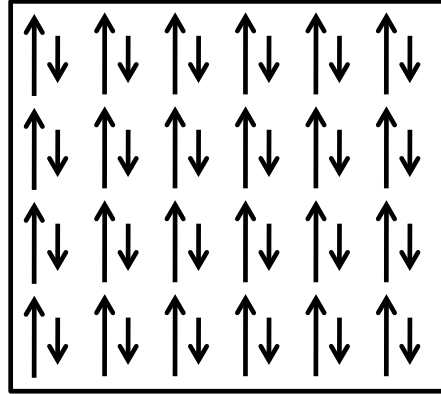
Fig.1.1.4: Arrangement of magnetic moments inside a ferrimagnetic material.

1.1.2. Ferroelectrics

Materials with spontaneous switchable electric polarization in an applied electric field are called ferroelectric materials. This phenomenon was first observed by Valasek in Rochelle salt[5]. The name ferroelectric arises from ferromagnets because of the analogous electric and magnetic properties these materials display. The prime requirement for a material to be ferroelectric is that they should have definite dipole moment values. This in turn necessitates the requirement for an absence of centre of symmetry. In addition, the polarization so developed should be switchable and hence two stable states should be accessible with moderate electric fields. Ground state of conventional ferroelectrics is normally made of a set of atomic displacements from the high temperature centrosymmetric - paraelectric phase.

Symmetry imposes restrictions on ferroelectrics. Out of the 32 point groups only those 21 space groups which does not have centre of symmetry are likely to have ferroelectricity. These non-centrosymmetric space groups are further divided

into chiral and polar space groups. Chiral space group is that which is devoid of inversion symmetry elements. Thus chiral space groups should only have rotational and translational components. These are namely point groups 1, 2, 3, 4, 6, 222, 422, 622, 32, 23 and 432. Polar point groups are those which have some polar directions which does not have any symmetry equivalent directions. These are point groups like 1, 2, 3, 4, 6, 3m, mm2.

Keeping all this in mind, it can be concluded that all ferroelectrics are pyroelectrics but all pyroelectrics are not ferroelectrics. There has to be switchability in the pyroelectric current to call it a ferroelectric. All pyroelectrics are peizoelectrics and this in turn makes all ferroelectrics peizoelectrics as well.

1.1.3. Multiferroics

Multiferroics according to H. Schmidt are materials that exhibit more than one primary ferroic order[1]. Ferroelectric and ferromagnetic properties are mutually exclusive as magnetism demands unpaired spins. The interaction between this unpaired spins gives rise to long range magnetic ordering. Ferroelectricity normally is found in transition metal cations with empty d orbital. Here covalent bonding occurs between filled orbital of oxygen and d orbital of transition metal cations. This is more energetically facile when cations have empty d orbital. This mutual exclusion of ferromagnetism and ferroelectricity makes the availability of multiferroics rare in nature.

Magnetoelectrics are a higher class of multiferroics in which there is coupling between electric and magnetic order parameters. This means one can influence magnetization (polarization) by electric (magnetic) field and vice-versa.

This coupling is actually independent of the nature of electric and magnetic state of the material and hence its presence never confirms the material as a multiferroic[6].
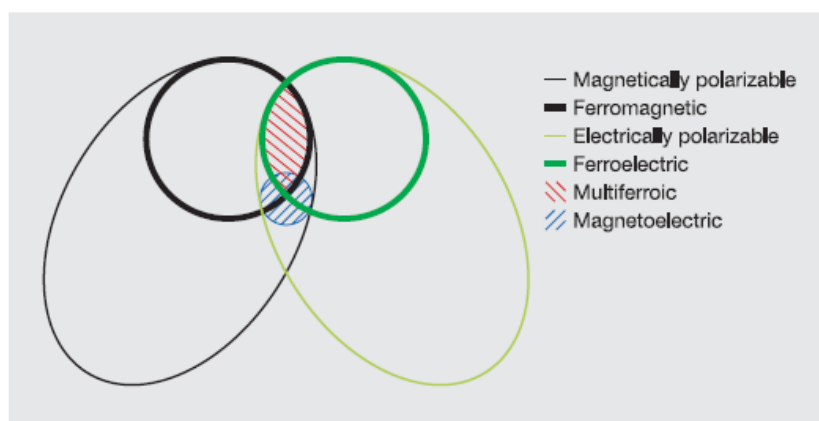
Fig.1.1.5: Relationship between magnetically polarizable and electrically polarizable materials to multiferroics and magnetoelectrics is depicted. Ferromagnetism comes as a subset of magnetically polarizable materials and so is ferroelectricity of electrically polarizable materials. When there is an overlap between this two ferroic properties, it becomes a multiferroic. Magnetoelectrics are another class of compounds where there is coupling between electric and magnetic order parameters. This arises irrespective of the magnetic/electric ground state of the material [6].[reprinted with permission from ref.6]

1.1.4. Types of multiferroics

Despite the mutual hatredness of ferromagnetism and ferroelectricity, there are many materials in which these properties co-exist. The rich physics and chemistry behind this co-existence have always lured scientists. One attempt of accomplishing this is to combine two different species which can act separately causing the properties to co-exist[7]. But as expected in these materials interaction / coupling between the two order parameters will remain weak and hence there is a requirement to improve on these[8]. Of late, there has been quite an interesting class of manganites coming up, in which ferroelectricity comes as an outcome of magnetic

interaction, the so called magnetically induced ferroelectrics like $TbMnO_3$[9], $TbMn_2O_5$[10], $DyMn_2O_5$[11] etc.. These materials are quite promising in terms of their interaction mechanism but they do so at low temperatures and often the resultant electric polarization is very low in magnitude. On the basis of the various mechanisms causing multiferroicity, materials have been broadly classified into four:

Table 1.1: Mechanisms for Multiferroics[12]:

Mechanism	Description	Examples
Lone-pair effects	In perovskites of general formula ABO_3, lone pair of electrons residing on the A cation distort the geometry of the BO_3 anion, leading to ferroelectricity.	$BiFeO_3$, $BiMnO_3$
Geometric frustration	Rotations of oxygen atoms and long-range dipole–dipole interactions generate a stable ferroelectric state.	$YMnO_3$
Charge ordering	'Non-centrosymmetric' arrangements of ions induce ferroelectricity in magnetic materials.	$LuFe_2O_4$
Magnetic ordering	Ferroelectricity results from the magnetic long-range order in which the arrangement of magnetic dipoles lacks reflection symmetry.	$TbMnO_3$, $DyMnO_3$, $TbMn_2O_4$

i)   Lone-pair effects

Bismuth and Lead based compounds are the prominent members of this category. These perovskites with A – cation bearing a stereochemically active lone-pair is known to be responsible for the ferroelectricity in these compounds. B-cation which is a transition metal with unpaired electrons imparts magnetism to these compounds. As already discussed, the origin of ferroelectricity and magnetism being from two different sources, they couple quite weakly. $BiFeO_3$ is an incommensurate antiferromagnet, with non-collinear spins taking long wavelength spiral form. It is also a commensurate ferroelectric at room temperature[13-15]. $BiMnO_3$ is a sole example for single phase material which is ferromagnetic and ferroelectric at room

temperature [16,17]. Orbital ordering is responsible for magnetism but since the material crystallizes in centrosymmetric $C2/m$ space group, ferroelectricity is attributed to local non-centrosymmetry as well, the reason of which is still debatable[18]. There are theoretical reports which suggests that magnetism along with spin-phonon coupling can give a plausible explanation for the local non-centrosymmetry[8,19]. $BiCrO_3$ is theoretically and experimentally found to be an antiferromagnet (< 123 K) with a weak parasitic ferromagnetic moment and anti-ferroelectric (440 K)[18,20].

ii)   Geometric frustration

There is a huge class of compounds in which ferroelectricity mainly arises from the geometrical arrangement. Important members of this group are hexagonal manganates. In these manganates, Mn^{3+} ions are located at the centre of a trigonal biprism and form a layered structure. Buckling of this MnO_5 biprisms leads to ferroelectricity in these compounds. Had there been a 3D connectivity in these manganates then, loss of inversion centre due to buckling have not been possible. The well known hexagonal manganate, $YMnO_3$[21] (space group: $P6_3cm$) is an
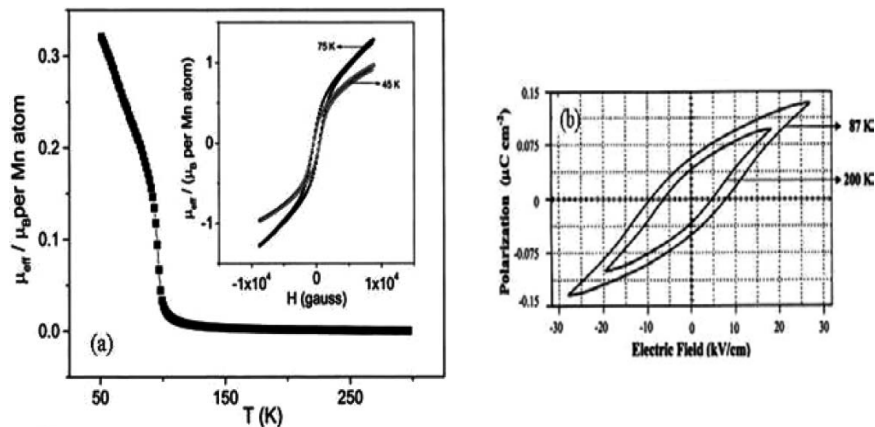
Fig.1.1.6: a) Temperature dependence of magnetization in BiMnO₃ [17]b) P-E hysteresis loop[17] [reprinted with permission from 16.]

improper ferroelectric (T_{FE} = 950 K) and has an A-type antiferromagnetic magnetic structure (T_N = 77 K) with non-collinear arrangement of Mn spins. As ferroelectricity in these compounds are a result of an attempt to close pack and an associated structural phase transition is also observed as expected at high temperatures (900 – 1000 K)[21]. Magnetoelectric coupling attributable to magneto-elastic coupling is also reported in this compound [22,23]. But since ferroelectricity and magnetism in these compounds have different origin, coupling between them cannot be very significant.
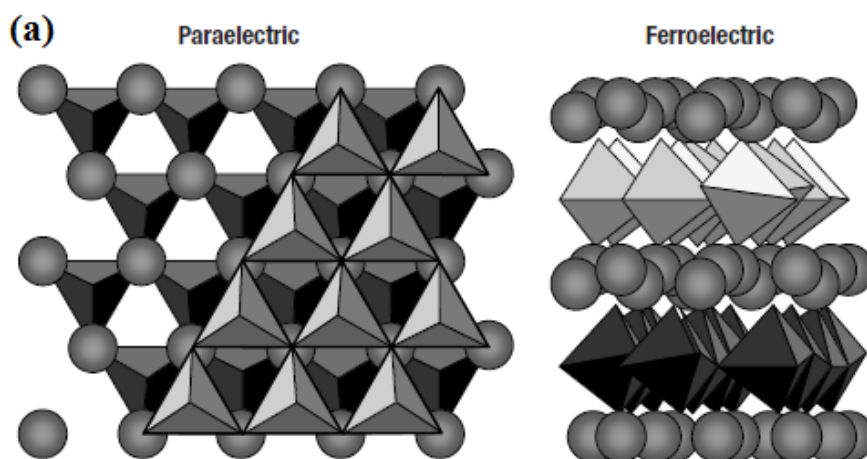
Fig.1.1.7: (a) Crystal structure for YMnO$_3$ for paraelectric and ferroelectric states are shown[21] [reprinted with permission from ref.20]

Hexagonal HoMnO$_3$ also exhibits dielectric anomaly at its T_N = 75 K[24,25]. Hexagonal LuMnO$_3$ also shows dielectric anomaly in the region of magnetic ordering with weak magnetoelectric coupling. Magnetic coupling in LuMnO$_3$ is in the a-b plane whereas electric dipole orientation is along hexagonal c-axis. These manganates (R= Ho,…Lu) can be forced into orthorhombic structure by applying pressure [26]. These orthorhombic manganates have E-type antiferromagnetic ordering which itself breaks inversion symmetry and leads to ferroelectricity which is purely electronic in nature[26].
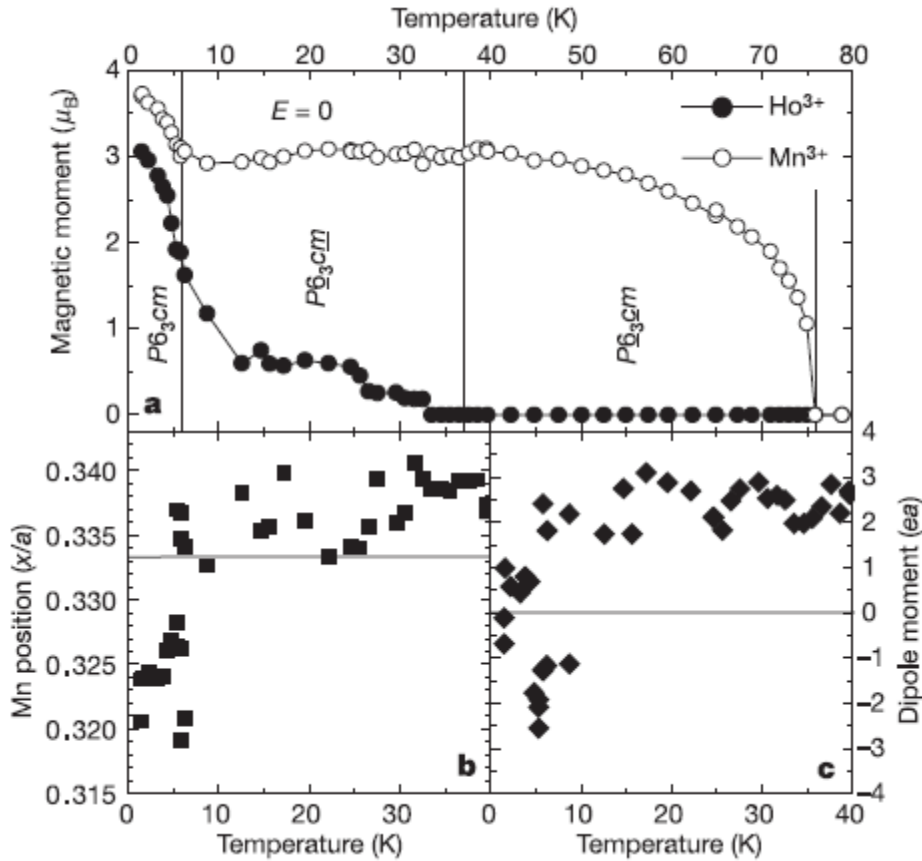
Fig.1.1.8: (a) Ordering of Ho^{3+} and Mn^{3+} moments $HoMnO_3$ (b)Mn^{3+} positions in the lattice and (c)Ferroelectric dipole moment in the unit cell are shown with an inset showing the relative change at 4.5 T^{25} . [reprinted with permission from ref.24]

iii)   Charge ordering

In charge ordered and orbital ordered perovskites, it was found that there exist a coupling between magnetic and charge ordering and this leads to magneto-ferroelectritciy[7]. The mechanism of this type of ferroelectricity can be explained as follows.

Charge ordering (CO) occurs in transition metal ions with mixed valancies or if there is an ordering of extra hole or electron in the lattice. Hence a half doped manganite, x= 0.5 with Mn^{3+} and Mn^{4+} can be shown as having a checkerboard pattern with site centered charge ordering. But this ordering is inefficient in breaking

the centre of symmetry and hence is not capable of inducing ferroelectricity (Fig.1.1.9a).

Another type of charge ordering occurs when the system dimerises. For eg. when there is Peierl's distortion present in the system. Here though sites are equivalent, bonds are not and hence bond-centered charge ordering takes place (Fig.1.1.9b). But even this cannot induce ferroelectricity[27].
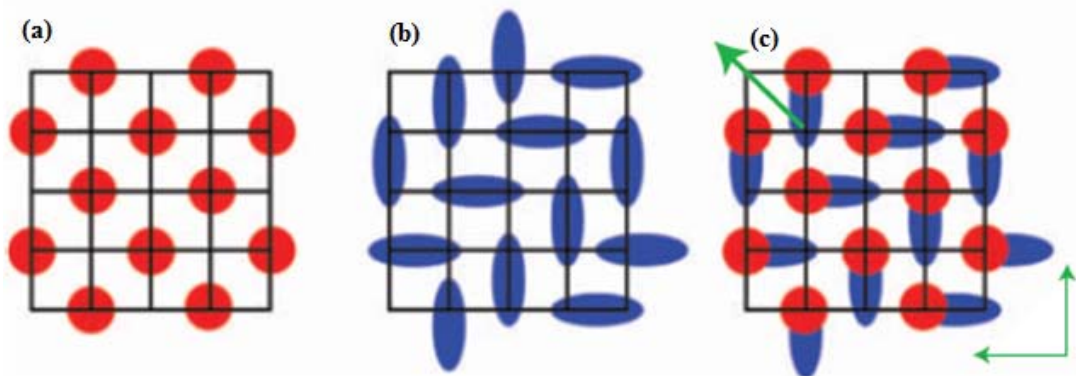
Fig. 1.1.9: (a) Site centered charge ordering (b) Bond centered charge ordering and (c) intermediate non-centrosymmetric state which is ferroelectric. Diagonal arrow showing the direction of net moment[28] . [reprinted with permission from ref.27]

Now, if there is an intermediate situation as shown in Fig.1.1.9c, in which site-centered and bond-cenetred ordering simultaneously co-exist, there is a destruction of centre of symmetry. As can be seen from the Fig. 1.1.9 left- and right- ,or up- and down- sides of the dimmers are inequivalent giving rise to a net dipole moment in the MnO_2 plane. This simultaneous occurrence of site-centered and bond-cenetred charge ordering can have many reasons. In some compounds where there are different valancies of cations present they can have site-centered charge ordering which after a structurally induced dimerisation can give rise to ferroelectricity. Or in a different scenario, structure can favour the existence of inequivalent bonds which

when aquires a spontaneous charge ordering below some ordering temperature can become a ferroelectric[7,29].

iv) Magnetic ordering

These are the class of compounds in which ferroelectricity is induced by magnetic ordering. $TbMnO_3$[9], $DyMnO_3$[30] and $GdMnO_3$[31] belong to this class of compounds. Taking the representative example of $TbMnO_3$[9], it can be seen that these compounds undergoes a series of low temperature magnetic transitions. It undergoes a incommensurate lattice modulation at T_N = 41 K; an incommensurate-commensurate (lock-in) transition at T_{lock} = 27 K ; and another one at still lower temperature (< 10K) due to ordering of R moments. It is only below 27 K that it
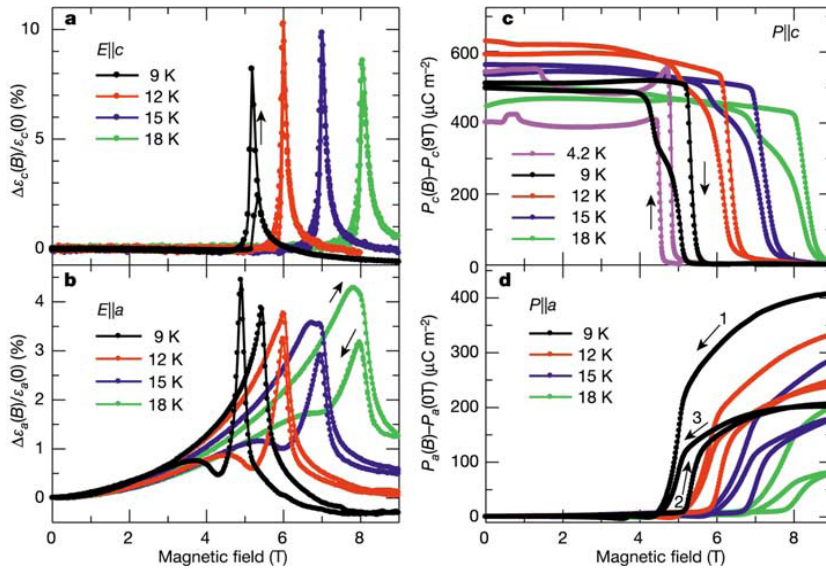
Fig. 1.1.10: (a) and (b) Magnetic field induced changes in dielectric constant along c and a direction (c) and (d) polarization along c and a direction in TbMnO₃ [9]. reprinted with permission from ref.9]

develops a finite electric polarization. This electric polarization so developed can be highly modulated by applied magnetic field. This manganites show a flop in electric polarization which is induced by a magnetic field [9]. Here the polarization direction

changes by 90° (from 'a' to 'c' direction) on the application of an external magnetic field.

In $TbMnO_3$[9], below T_{N1} = 41 K the magnetic structure is a sinusoidal spin-density wave, that is all the spins point in one direction, but the size of the local moment varies periodically in space (Fig.1.1.10). Here the centre of symmetry is not broken and the net dipole moment turns out to be zero. Below T_{N2} = 28 K, the Mn spins order in such a way that the tip of the spins sweep out a cycloid (Fig.1.1.11). When this magnetic structure changes from sinusoidal to helicoidal, then electric polarization appears in the system.
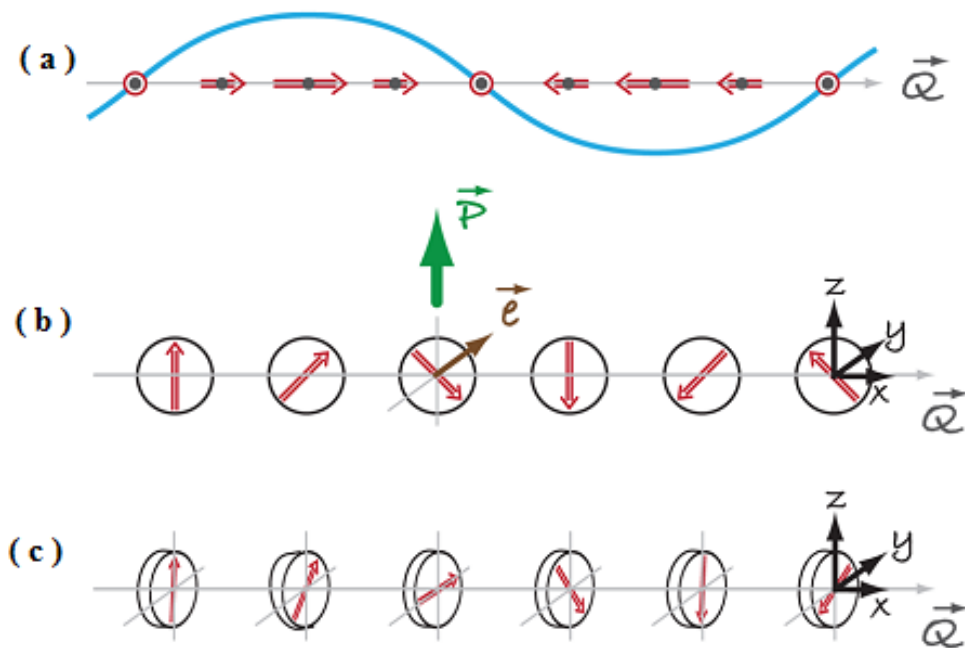
Fig.1.1.11: : Different types of spin structures (a) Sinusoidal spin density wave, in which spins varying in magnitude point along one direction. This structure is centrosymmetic and hence not ferroelectric. (b) The cycloidal spiral with the wave spins rotating in the (x,z) plane. Here one finds a nonzero polarization, $P_z \neq 0$. (c) The so-called "proper screw" the spins rotate in a plane perpendicular to Q. Inversion symmetry is broken here, but polarization rarely results[32,33] .[reprinted with permission from ref.[32] American Physical Society/Alan Stonebraker]

If the spin rotation axis **e** does not coincide with the wave vector of a spiral **Q** then polarization **P** appears and is proportional to the vector product of **e** and **Q**,

$$P \sim [Q \times e].$$

Hence, if a magnetic field forces the plane of a magnetic cycloid to flop by 90 degrees, the polarization **P** also flops by 90 degrees. From the above equation **P** lies in the plane of spins but perpendicular to **Q**. Thus in a spiral spin structure the inversion symmetry is already broken by some mechanism, most probably involving spin-orbit coupling.
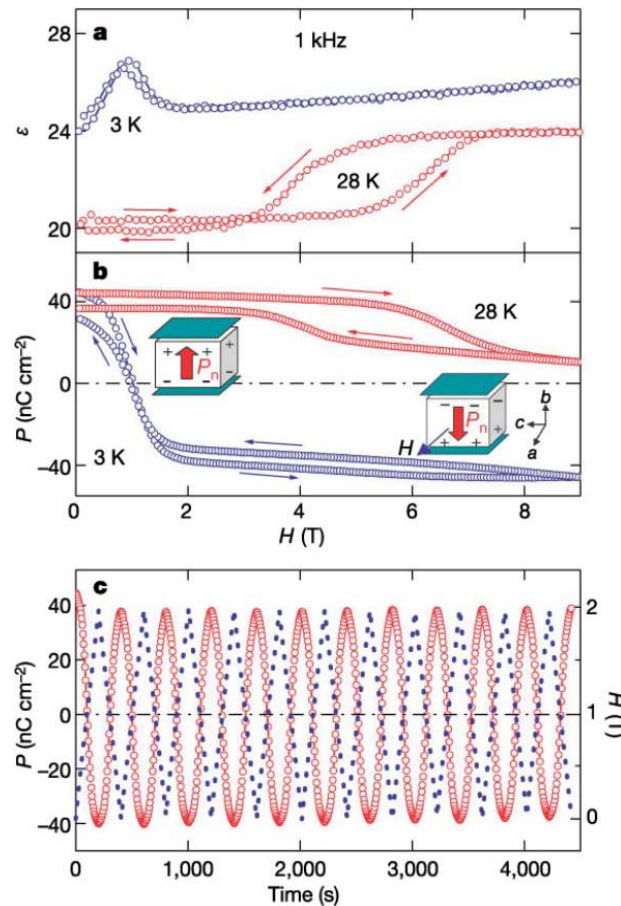
Fig.1.1.12: (a) Dielectric constant of $TbMn_2O_5$ at 3 K and 28 K plotted as a function of magnetic field. (b) Polarization at 3 K and 28 K as a function of magnetic field. (c) Polarization switching at 3 K at an applied field of 0-2 T [10].[reprinted with permission from ref.10]

Another class of compounds with non-classical spin structure are manganates of the general formula RMn_2O_5[34]. These manganites have edge-sharing MnO_6

octahedra running along the c-axis which are in-turn connected in the a-b plane by MnO_5 pyramidal units. These pyramids are believes to be responsible for ferroelectricity in these compounds. These compounds undergo a series of magnetic and electric phase transitions. There is also a re-entrant low temperature paraelectric phase which is highly tunable with applied magnetic field. $TbMn_2O_5$[10] shows switchable polarization as well as memory effect and $DyMn_2O_5$[35] shows colossal magnetodielectric effect (109 % at 3K).

1.1.5. Magnetoelectric effect

The discovery of magnetoelectric effect (ME effect) dates back to 18th century when Röntgen discovered[36] (1888) a moving dielectric getting magnetized in an electric field and the sooner realization of the reverse effect (1905)[37]. Curie in 1894 predicted the existence of intrinsic ME effect which he envisaged to be controlled by symmetry[38]. The ME effect was experimentally realized in Cr_2O_3 in 1960's[39-43].This was indeed a breakthrough in the research of multiferroics. These materials are quite promising as memory devices, optical diodes, for frequency conversion etc[44].

Magnetoelectric effect in a single phasic compounds can be described by Landau theory by expressing free energy of the system in terms of magnetic field, electric field and their cross-coupling terms as[6]:

$$-F(E,H) = \frac{1}{2}\varepsilon_0\varepsilon_{ij}E_iE_j + \frac{1}{2}\mu_0\mu_{ij}H_iH_j + \alpha_{ij}E_iH_j + \frac{\beta_{ijk}}{2}E_iH_jH_k + \frac{\gamma_{ijk}}{2}H_iE_jE_k + \cdots$$

Here first term describes the electric response of a material to the applied electric field where ε_0 is the permittivity of free space and ε_{ij} is the relative permittivity. Second term describes magnetic response with μ_0 as the permeability of free space and μ_{ij} as the relative permeability. Third term is for linear magnetoelectric coupling

and other terms are for higher order couplings involved. To establish magneto electric effect, if we differentiate F with respect to E_i and set E_i to zero, then we get P_i as a function of H_j as:

$$P_i = \alpha_{ij}H_j + \frac{\beta_{ijk}}{2} H_j H_k + \cdots$$

Similarly, differentiating F with respect to H_i and setting H_i to zero gives M_i as a function of E_j as:

$$\mu_o M_i = \alpha_{ji}E_j + \frac{\beta_{ijk}}{2} E_j E_k + \cdots$$

Linear magnetoelectric coupling constant α_{ij} can be written as $\alpha_{ij}^2 \leq \varepsilon_0\mu_0\varepsilon_{ii}\mu_{jj}$ and hence a multiferroic material that is simultaneously ferromagnetic and ferroelectric can be expected to show large linear magnetoelectric coupling because they tend to have huge values of permittivity and permeability.

In many materials linear magnetoelectric coupling will be small due to smaller values of either ε_{ij} or μ_{ij} or both. But this doesn't prevent the existence of higher order coupling terms like β_{ijk} or γ_{ijk}. This so called **non-linear coupling** is found mainly in materials with reduced dimensionality. There are other still complex coupling phenomena possible in which coupling is indirectly mediated through strain. This becomes important in the discussions of peizomagnets and peizoelectrics where magnetostriction and electrostriction becomes important.

1.1.6. Magnetodielectric effect

Magnetoelectric effects in materials are restricted by symmetry and hence in recent years a more general term called **magnetodielectric effect** has been introduced. It was first suggested by Lawas et.al[45]. This describes a more generalized coupling and hence there are no symmetry constraints. Such materials show

anomalies in dielectric constant/capacitance when an external magnetic field is applied.
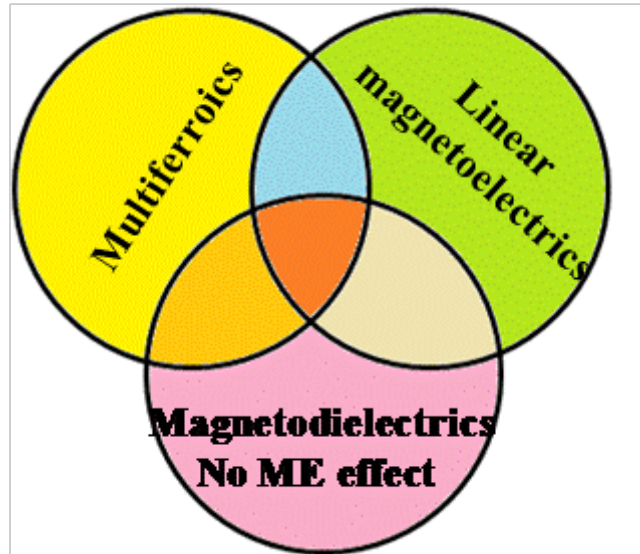
Fig.1.1.13: Relationship between magnetodielectrics and multiferroics is shown. Magnetodielectrics represent a broader category which is not restricted by symmetry.

Research in multiferroics has reached a very interesting forefront wherein even centrosymmetric materials show interesting signatures of ferroelectricity due to local non-centrosymmetry[19] . There has been coupling between electric and magnetic order parameters triggered externally by strain etc[14]. There is also tremendous work done in the field of composites, in which one component is responsible for magnetism and the other for ferroelectricity. Magnetoelectric multiferroics with considerable coupling between electric and magnetic order parameters are also being realized in multiferroics in which ferroelectricity is magnetically induced [9,10]. Unified theoretical and experimental efforts are underway for realization of room temperature magnetoelectric multiferroics.

1.2. Scope of the Present Investigations

Multiferroics and magnetoelectric materials are gaining importance in modern technology [46,47]. Though conventional knowledge about ferroelectricity and ferromagnetism reveals their mutually exclusive nature, as this century unfolds there has been numerous reports in which ferroelectricity arises due to unconvential reasons [6]. This has indeed opened up doors for research in this area, both experimental and theoretical. Many of the materials neglected in the past, demands reinvestigation. Multiferroics and magnetoelectric effect provides a rich area for exploring fundamental science. We have basically looked into the $Al_{1-x}Ga_xFeO_3$ (x = 0.0, 0.5) family of oxides. There have been previous reports about this oxide family but these are scattered and are not consolidated. We have conducted a detailed study of the structure, dielectric and magnetic properties of this family of oxides. An interesting phase transition was observed in these oxides upon ball-milling stabilizing metastable (corundum) phases. We have also doped it with Mn site-specifically and have studied their magnetic properties.

1.2.1. Structure, Magnetic Properties of $Al_{1-x}Ga_xFeO_3$ (x = 0 .0, 0.5)

Al_2O_3 and Fe_2O_3 which are the precursors for $AlFeO_3$, both crystallizes in corundum structure (R-$3c$). But $AlFeO_3$ is isomorphous with $GaFeO_3$ which has been already reported since 1960 by Remeika $et.al.,$[48]. This compound crystallizes in an

orthorhombic crystal structure with $Pna2_1$ space group [49-51]. Schieber *et.al.,* studied $Al_{2-x}Fe_xO_3$ family of oxides and concluded that the orthorhombic phase is stable in the range (x = 0.6 - 1.0) [52]. He also reported these oxides to be piezoelectric and magnetization in them to be composed of two non-equivalent sites having opposite magnetic moments. Bouree *et.al.,*[49] had done a detailed neutron diffraction study on $AlFeO_3$ and had found that this compound has four different cation sites which have octahedral and tetrahedral packing of oxygen atoms. They have found tetrahedral packing responsible for the piezoelectricity in this oxide. Fe^{3+} moment calculated by them turned out to be 3.4 ± 0.3 μ_B which is lower than expected. They have attributed this to the disordered occupancy of cations in the system. This motivated us to understand the basic structure and magnetic properties of $AlFeO_3$ and also Ga doped $AlFeO_3$ .We have investigated the chemical as well as magnetic structure of $AlFeO_3$ and $Al_{0.5}Ga_{0.5}FeO_3$ through neutron diffraction measurements. Magnetic properties of these compounds were also studied as a function of Ga^{3+} incorporation.

1.2.2. Phase transition in $Al_{1-x}Ga_xFeO_3$ (x = 0.0, 0.5)

Thermodynamically, the stable phase for $Al_{1-x}Ga_xFeO_3$ family of oxides is found to be orthorhombic with the non-centrosymmetric $Pna2_1$ space group [53]. The stability of this phase is attributed to the entropy contribution to free energy [53]. This entropy is believed to have a disorder related origin. We were interested in studying the phase transitions possible in this family of oxides. Nagai *et.al.,* have reported corundum (R-3c) phase being stabilized at high pressures [54]. To our surprise ball milling was able to stabilize metastable orthorhombic ($P2_12_12_1$) and rhombohedral (R-3c) phases.

1.2.3. Effect of Mn Doping in Ga/Fe sites of GaFeO$_3$

Doping of GaFeO$_3$ by magnetic ions can have substantial effect in the magnetic properties of these compounds. Mn^{3+} is a very interesting ion with respect to its magnetic moment and Jahn - Teller distortion. Though ionic sizes of Fe^{3+} and Mn^{3+} are identical, magnetically this doped system will be interesting. There has been a recent report in this regard [55]. They have doped Mn^{3+} in the Fe^{3+} site and found that transition temperature, saturation magnetization and coercivity were decreases. They have attributed this to the antiferromagnetic coupling between Mn^{3+} and Fe^{3+} ions [55]. We have done site specific doping of GaFeO$_3$ by controlled solid state method and the difference in the site specificity in interaction was monitored through magnetic studies.

1.2.4. Magnetic and ferroelectric properties of $Al_{1-x-y}Ga_xFe_{1+y}O_3$ compounds

Reports by Schieber *et.al.,* [52] states that $Al_{1-x}Fe_xO_3$ is stable in the orthorhombic phase for $0.6 < x < 1.0$ and $Ga_{1-x}Fe_xO_3$ in the range $0.8 < x < 1.2$. On these grounds, we modified $Al_{1-x}Ga_xFeO_3$ compositions to $Al_{1-x-y}Ga_xFe_{1+y}O_3$ aiming at an increase in the magnetic transition temperature. Ferroelectric properties of these compounds were also explored at low temperatures using pyroelectric measurements.

1.2.5. Dielectric and related properties of $Al_{1-x}Ga_xFeO_3$ (x=0.0, 0.5)

There have been very superficial dielectric studies on this system[50,51,56] but a detailed study of the multiferroic nature of these compounds has not been carried out to the best of our knowledge. There were reports on the isomorphous GaFeO$_3$ declaring them as magnetoelectric material (though ferroelectricity was not

satisfactorily probed) [57-59]. This motivated us to look into the dielectric, pyroelectric and subsequently the magnetoelectric properties of Al$_{1-x}$Ga$_x$FeO$_3$ (x = 0.0, 0.5). In the case of AlFeO$_3$, Raman studies were carried out to understand the nature of ferroelectricity and magnetoelectric coupling.

1.3. Experimental Section

1.3.1. Materials Synthesis

In this section different synthesis techniques used for the preparation of polycrystalline samples are discussed. This includes a description of conventional solid state method which was used to prepare the samples and ball milling which resulted in the phase transformation of these samples.

1.3.1.1. Solid state synthesis

Solid state synthesis is one of the widely used methods for the synthesis of polycrystalline samples. This method is known over years for its simplicity and versatility. Normally these reactions do not occur at room temperature and require high temperatures. There are thermodynamic and kinetic factors governing the formation of the product. Thermodynamics decide whether or not a particular reaction is feasible through free energy considerations whereas kinetics decide the rate at which the reaction occurs. There are three important factors that influence the rate of a solid state reaction[60], namely i) area of contact between the reactants ii) rate of nucleation and iii) rate of diffusion. Area of contact increases as the surface area of solids increases and this is achieved in a typical synthesis by prolonged grinding which reduces the grain size and pressing of the reactants into a pellet prior to heating. Rate of nucleation depends on the structural relationship between the reactants and products involved. Reaction temperature is often kept high in order to

increase the diffusion length. This in turn will have its effect in increasing the nucleation and diffusion rates. A solid state reaction normally occurs at the interface and hence possible rate determining steps are the rate at which matter is transported to the surface, rate at which the reaction happens at the surface and finally the rate at which matter is transported away from the surface[60].

Synthesis of AlFeO$_3$ and Al$_{0.5}$Ga$_{0.5}$FeO$_3$

These oxides were prepared by the solid state method. AlFeO$_3$ was prepared from α - Al$_2$O$_3$ and α - Fe$_2$O$_3$. These were preheated to a temperature of 1173 K. Stoichiometric amounts of Al$_2$O$_3$ and Fe$_2$O$_3$ were mixed thouroughly. Grinding, pelletizing and heating were repeatedly carried out through intermediate temperatures to 1673 K until phase pure compound was formed. Al$_{0.5}$Ga$_{0.5}$FeO$_3$ was prepared by heating the appropriate mixture of Al$_2$O$_3$, Ga$_2$O$_3$ and Fe$_2$O$_3$ at 1673 K for 5 h.

Synthesis of Ga$_{1-x}$Mn$_x$FeO$_3$ and GaFe$_{1-x}$Mn$_x$O$_3$

Site specific doping of GaFeO$_3$ was achieved by a two step solid state synthesis. To obtain GaFe$_{1-x}$Mn$_x$O$_3$ (x = 0.05, 0.1) compositions where the Fe site was substituted by Mn, α - Fe$_2$O$_3$ was substituted by appropriate quantities of Mn by calcining stoichiometric mixtures of Fe$_2$O$_3$ (Aldrich, 99.98%) and Mn$_2$O$_3$ (Aldrich, 99.0%) at 1273 K for 12 h. These pellets were then reground and mixed with stoichiometric amounts of β - Ga$_2$O$_3$ (Aldrich,99.99%) and sintered at 1573 K for 12 hours. Inorder to substitute Mn in the Ga site, β - Ga$_2$O$_3$ was mixed with stoichiometric amounts of Mn$_2$O$_3$. This mixture was then calcined at 1373 K (12 h). The pellets were reground and mixed with stoichiometric amounts of α - Fe$_2$O$_3$ and sintered at 1573 K for 12 hours. This yielded Ga$_{1-x}$Mn$_x$FeO$_3$ (x = 0.05, 0.1) compositions where Mn ions were substituted at the Ga site.

Synthesis of Al$_{1-x-y}$Ga$_x$Fe$_{1+y}$O$_3$

These oxides were prepared by the solid state method. Stoichiometric amounts of Al$_2$O$_3$, Fe$_2$O$_3$ and Ga$_2$O$_3$ were mixed thouroughly. Grinding, pelletizing and heating were repeatedly carried out through intermediate temperatures to 1673 K until phase pure compound was formed.

1.3.1.2. Ball Milling

A ball mill basically consists of a grinder which rotates around a horizontal axis. It will be filled with the material which has to be grinded along with the grinding medium (milling-balls). There is normally a supporting disk which performs a circular movement causing the vials to rotate around their own axes[61]. Since these rotations take place in opposite directions, centrifugal force will act in opposite directions causing the balls to move inside the vial (Fig.1.3.1). Balls are generally made of zirconia, chrome steel, agate etc. These balls will rotate at a particular speed which results in converting the material to a fine powder. There is a critical speed above which the balls will remain pinned to the walls of the vial, hence it is important that the maximum speed remains below this critical value.
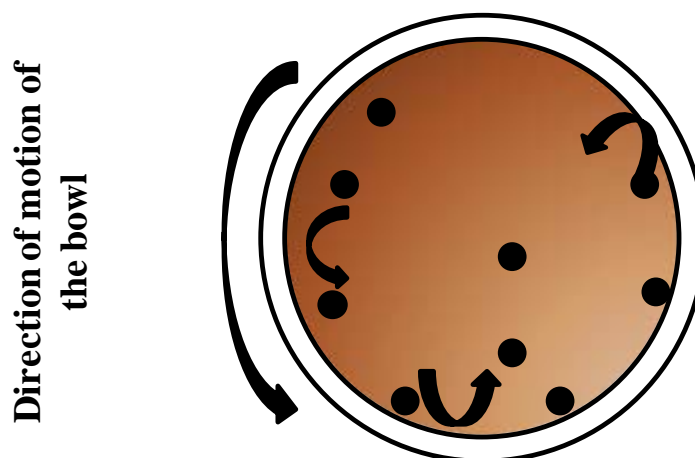
Fig.1.3.1: Schematic of motion of balls inside the vial.

Ball Milling of $Al_{1-x}Ga_xFeO_3$ (x = 0.0, 0.5)

$Al_{1-x}Ga_xFeO_3$ (x = 0.0, 0.5) prepared by conventional solid state method as described earlier was subjected to ball-milling using a planetary monomill (Fritsch Pulverisette-6, Berlin, Germany). A batch containing 2 g of the sample was taken in a 80mL capacity agate (99.9% SiO_2) bowl and was dry milled with the aid of 10-15 agate balls of 10 mm diameter at a speed of 400 rpm for 12 h. The ambient temperature during ball-milling was roughly around 673 K. These samples were then annealed in air at 973 K, 1273 K and 1623 K in order to confirm reversibility of the observed structural phase transition.

1.3.2. Characterization Techniques

1.3.2.1. Powder X-ray Diffraction

X-ray diffraction is used to determine the phase purity of the samples under study. X-ray diffraction pattern is a set of lines varying in intensity occurring at specific angles (2θ)[60]. These peaks corresponds to certain set of Bragg planes (Fig.1.3.2) present in the unit cell and its intensity depends on several factors like the atoms occupying that plane, systematic absences etc. The equation that relates the lattice spacing (d_{hkl}) with observed 2θ is called Bragg equation and is as follows:

$$2d_{hkl}\sin\theta = n\lambda$$

Here d_{hkl} is the spacing for a hkl plane, θ is the glancing angle, n the order of diffraction and λ the wavelength of x-ray used (1.54 Å for CuKα).

Thus for quantitative phase determination both peak position as well as peak intensity needs to be crucially analyzed. Phase purity of the sample is usually analyzed by comparing the observed experimental pattern against the database maintained by International Centre for Diffraction Data (ICDD). Further information

regarding the unit cell parameters namely cell dimensions like a, b, c, α, β, Υ can be obtained by profile matching the pattern against a simulated pattern using FULLPROF software.
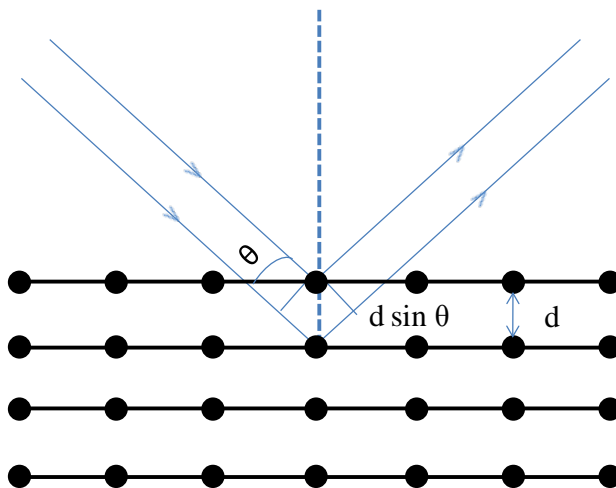
Fig.1.3.2: Schematic showing diffraction of x-rays from bragg planes at a grazing angle θ.

X-ray diffraction patterns of the samples were recorded with a Bruker D8 Advance X-ray diffractometer using a Cu Kα x-ray source to confirm the phase purity. Profile fitting was done with the help software package Fullprof.

1.3.2.2. Powder Neutron Diffraction

Neutron diffraction is a very sensitive and expensive technique used mainly for the characterization of lighter elements and magnetic structure of materials. In this technique sample, have to be impinged by a beam of thermal neutrons. Since neutron has spin quantum number ½ and has a magnetic moment, it can interact with the nucleus and unpaired electrons in the system enabling the determination of magnetic structure of the materials under investigation. Moreover, neutrons don't have any charge and hence it can penetrate the material quite easily. Unlike in x-ray diffraction there is no fall of intensity with θ in the neutron diffraction since the

interaction length is shorter than wavelength of neutron. Also, in neutron diffraction scattering power is not strongly influenced by the atomic number, as neutrons directly interact with the nucleus.

Magnetic structure is determined by collecting the data above and below the transition temperature. If there is magnetic ordering in the system, magnetic scattering will occur in that particular direction which can be indexed and from which magnetic unit cell can be determined.

Neutron powder diffraction measurements on polycrystalline samples were carried out using the five linear position sensitive detector (PSD) based powder diffractometer (λ=1.2443 Å) at Dhruva research reactor, Trombay, INDIA. The powdered samples were placed in a cylindrical vanadium container and a commercial closed cycle helium refrigerator was used for low temperature measurements. The analysis of the diffraction data were done by Rietveld refinement method using the FULLPROF program[62,63]. The representative theory was performed using the BASIREPS software [62,63].

1.3.3. Measurements of Physical Properties

1.3.3. 1. Magnetic Measurements

Different magnetometers are available for studying magnetic materials. Vibrating sample magnetometer is one among them which was invented by S. Foner in 1959[64]. This instrument working on the principle of flux change in a coil when a magnetized sample is vibrated near it, is used for magnetic measurements[65]. The sample here is attached to the end of a non-magnetic rod whose other end is attached to a mechanical vibrator. The resulting oscillating magnetic field will induce an

alternating emf in the detection coil. The amplitude of this induced emf will be proportional to the magnetic moment of the sample. This signal is then amplified by a lock-in amplifier.

Magnetic studies in thesis are carried out by using a vibrating sample magnetometer in a Physical Property Measurement System (PPMS) of Quantum Design, USA. Temperature dependence of Field-cooled (FC) and Zero field cooled (ZFC) magnetization are measured. In FC measurement, sample is cooled to low temperature in the presence of magnetic field and data were collected on heating the sample. In ZFC measurement, sample was cooled to low temperatures in the absence of magnetic field and data was collected while heating the sample in presence of an applied field. Hysteresis loops were recorded at temperatures below the transition temperature.

1.3.3.2. Dielectric Measurements

Dielectric is a material which has the ability to store charge under an external electric field. If a DC voltage source is applied across a parallel plate capacitor with a dielectric material, more charge will be stored inside the capacitor compared to when there is no material between the plates (Fig.1.3.3).

If C and C_o are the capacitances with and without a dielectric medium, then

$$C_o = \frac{A}{t}$$

$$C = C_o \kappa'$$

$$\kappa' = \frac{C}{C_o} = \epsilon'_r$$
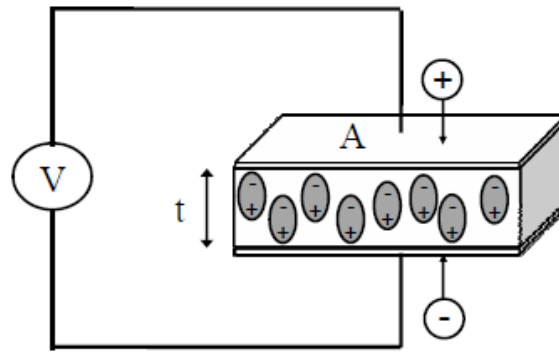
Fig. 1.3.3.: Parallel plate capacitor

κ' is the dielectric permittivity and A is the area of the capacitor and t is the distance between the parallel plates. Dielectric constant is equivalent to relative permittivity ε_r , which is the ratio of absolute permittivity (ε) to the permittivity of free space (ε_o).

$$\kappa = \frac{\varepsilon}{\varepsilon_0} = \varepsilon_r = \varepsilon'_r - i\varepsilon''_r$$

ε'_r is called the real part of dielectric constant and is a measure of amount of energy stored from an external magnetic field and ε''_r is called imaginary part of the dielectric constant and is a measure of how dissipative the material is to external electric field. When dielectric permittivity is drawn as a vector diagram with real and imaginary components going 90° out of phase and vector sum forming an angle δ with the real axis, then

$$\tan \delta = \frac{\varepsilon''_r}{\varepsilon'_r}$$

This is called relative lossiness and is a ratio between the energy lost to the energy stored.

For dielectric measurements, disc-shaped pellets were made and polished. These were then transformed to capacitor geometry by depositing gold/silver electrodes on either sides of the disc. Electrodes were then made using copper wire and fixed with silver paste. Dielectric measurements were carried out using Precision Impedance Analyzer (Agilent 4294 A). Frequency analysis was carried out on the samples in a frequency range of 100Hz - 1MHz.

1.3.3.3. Ferroelectric Hysteresis and Pyroelectric Measurements

Ferroelectric hysteresis measures induced polarization in presence of an applied electric field. A P-E hysteresis is the signature of a ferroelectric material.

Ferroelectric measurements here are carried out using a Radiant Technologies Precision Workstation. A Sawyer-Tower circuit is usually used for the measurement of P-E hysteresis loops. Here the capacitor to be measured is kept in series with a test capacitor. Triangular voltage waveform is applied in steps which induce current which is then integrated to obtain charge. This is then converted to polarization.

$$Q/Area = CV/Area = \mu C/cm^2$$

For leaky materials pyroelectric measurements are done to confirm the ferroelectricity. In these measurements, sample is cooled below ferroelectric transition temperature in presence of an applied field. At this temperature the sample is shotted to remove the stray charges. The current is then measured on heating the sample and is plotted as a function of temperature and time. This is converted to polarization as follows:

$$P = \frac{\int I dt}{A}$$

Pyroelectric measurements were done using a Keithley 6517A electrometer. This electrometer was interfaced with the temperature controller and pyroelectric current was measured against time and temperature simultaneously.

1.3.3.4. Magneto-Dielectric Measurements

A cryo cooled closed cycle superconducting magnet which can reach upto 14 T was used for magneto-dielectric measurements. This magnet is a single coil of multifilamentary Nb_3Sn and is wound on to stainless steel. The coil has a superconducting persistent mode switch to connect parallelly across the whole magnet and to maintain input/output current terminals. This wire is provided with resistive heaters which enable it to be resistive / superconducting. The leads here are made of 2223 ($Bi_2Sr_2Ca_2Cu_3O_{10}$) superconductor. Magnet can go upto 14 T in a temperature ranging from 20 K to 350 K.

In the samples under investigation magnetodielectric effect was measured in the temperature range 50 – 350 K. Samples mounted on a custom made sample holder was inserted into the cryo system. The samples were then cooled to lowest temperature and the measurement was done while heating it in presence of a magnetic field. Care was taken to stabilize the system at every temperature to avoid artifacts due to temperature fluctuations as much as possible.

1.3.3.5. Magnetoresistance measurements

Magnetoresistance measurements were done in Physical Property Measurement System (PPMS) of Quantum Design, USA using a four probe resistivity measurement set up so as to minimize contact resistance. There will be four probes attached to the sample. Current will be passed through outer two probes and voltage measured between inner two probes. Then using the relation,

$$V = I/R$$ where I is the current and V is the voltage developed.
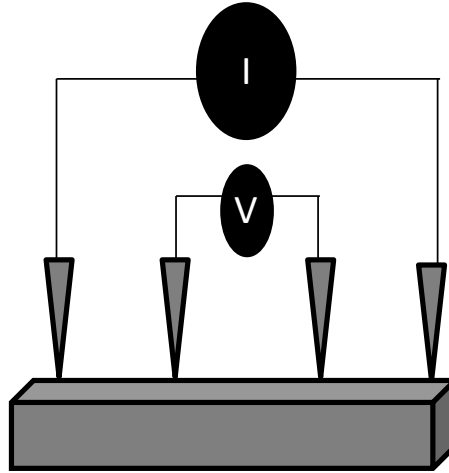
Fig. 1.3.5.: Four-probe set up for resistivity measurements

Knowing the dimensions of the sample used resistivity (ρ) can be calculated by using the formula,

$$\rho = R\frac{A}{l}$$ where A is the area and l is the distance between the inner probes.

Sample is cut into a rectangular pellet and contacts were given using copper wires connected with the help of silver paste. Resistance of this sample was then measured as a function of temperature. To determine magnetoresistance the same measurement was repeated in the presence of an applied constant field.

1.3.3.6. Raman measurements:

Raman spectroscopy relies on the inelastic scattering of light by the sample when it is illuminated by a light source. This effect occurs when the light incident on the material interacts with the electron cloud in the material exciting it to go to higher energy states. Molecular polarizability is a necessary condition for a molecule

to display Raman effect. In condensed matter physics, this tool is used to study various phase transitions by monitoring the low frequency Raman modes.

Basically the sample is illuminated by a light source (normally a laser). The light is then collected back through lenses and is sent to a monochromator. Wavelengths closer to the laser line, are filtered out and rest is collected using a detector.

Raman measurements discussed in this thesis were done in collaboration with Prof. A. K. Sood. These unpolarized micro-Raman measurements were performed in backscattering geometry using 514.5 nm line of an Ar-ion Laser (Coherent Innova 300) on a Raman spectrometer (DILOR XY) which was coupled to a liquid nitrogen cooled CCD detector. Temperature was varied from 5 K to 300 K, with a temperature accuracy of $\pm$ 0.1 K using continuous flow He cryostat (Oxford Instrument).

1.4. Results and Discussion

1.4.1: Structure and Magnetic Properties of $Al_{1-x}Ga_xFeO_3$ (x=0.0, 0.5)

Crystal structure of $AlFeO_3$ and $Al_{0.5}Ga_{0.5}FeO_3$ samples were analyzed using X-ray and neutron diffraction techniques. Both these samples were found to have the same crystal structure crystallizing in an orthorhombic space group. Magnetic structure was also investigated using neutron diffraction measurements. It was found that magnetic unit cell is similar to the chemical unit cell.

1.4.1.1. Structure Determination

(a) X-ray Diffraction Studies

X-ray diffraction measurements were carried out on $AlFeO_3$ and $Al_{0.5}Ga_{0.5}FeO_3$ samples which were prepared through conventional solid state method. These X-ray diffraction patterns show the phase purity of these samples. $AlFeO_3$ is isomorphous to $GaFeO_3$ and crystallizes in a non-centrosymmetric space group, $Pna2_1$. The intermediate compound $Al_{0.5}Ga_{0.5}FeO_3$ also crystallizes in the same space group. There was slight shift in 2θ values to the left as compared to those of $AlFeO_3$ due to the incorporation of bigger Ga^{3+} ion into the A-site. These XRD pattern were profile matched using FULLPROF software. Unit cell parameters obtained for $AlFeO_3$ are a = 4.9887(2), b = 8.5633(3), c = 9.2567(3) and $\alpha = \beta = \gamma =$

90°. Unit cell parameters obtained for $Al_{0.5}Ga_{0.5}FeO_3$ are a = 5.0293(1), b = 8.6438(1), c = 9.3158(1) and α = β = γ = 90°. It can be seen that the cell volume has slightly increased on incorporation of Ga^{3+} ion. In Fig.1.4.1, X-ray diffraction patterns of $AlFeO_3$ and $Al_{0.5}Ga_{0.5}FeO_3$ along with their profile fits and difference patterns are shown.
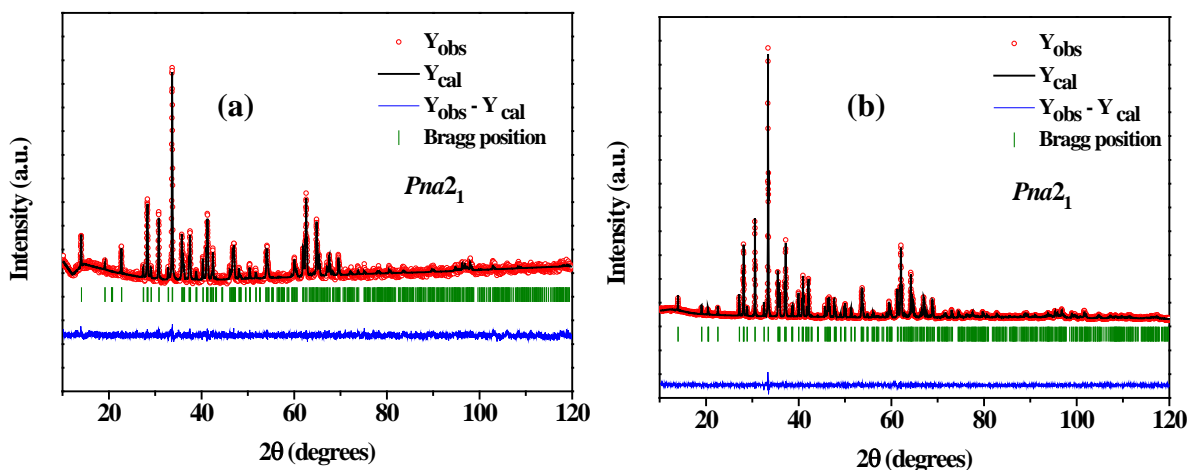
Fig.1.4.1: X-ray diffraction pattern along with profile matching is given for (a) $AlFeO_3$ and (b) $Al_{0.5}Ga_{0.5}FeO_3$.

(b) Neutron Diffraction Studies

Neutron diffraction was performed on both these samples from room temperature down to 5 K (Fig.1.4.2). At room temperature diffraction intensities matches with nuclear intensities only and hence the sample is paramagnetic at this temperature. Both $AlFeO_3$ and $Al_{0.5}Ga_{0.5}FeO_3$ have same crystal structure with only difference in the occupancy of the A-site cation[66]. Fig.1.4.2 shows the neutron data collected at different temperatures for $AlFeO_3$ and $Al_{0.5}Ga_{0.5}FeO_3$[66].

38
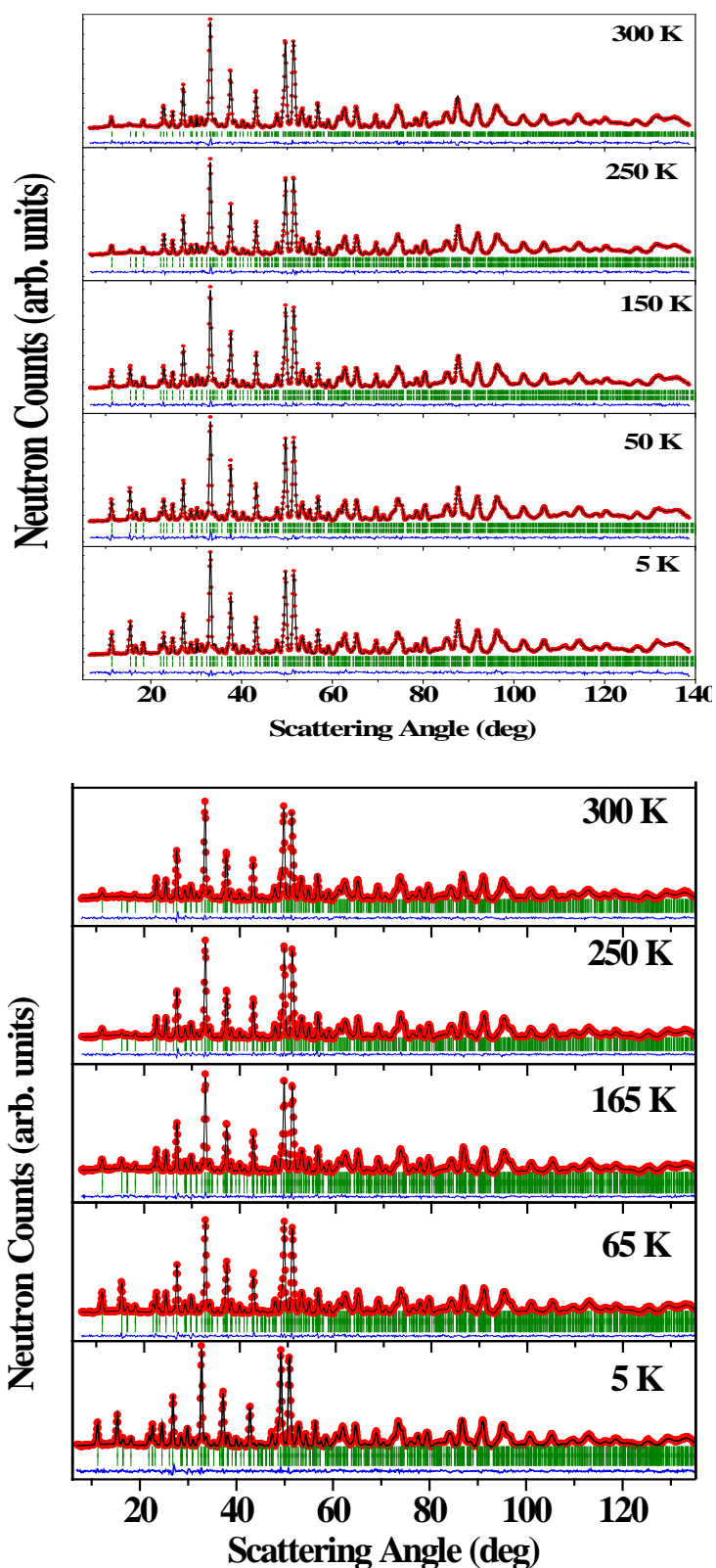
Fig.1.4.2: Observed neutron diffraction pattern (red solid circles) and calculated (solid lines) neutron diffraction patterns of the (a) AlFeO$_3$ (b)Al$_{0.5}$Ga$_{0.5}$FeO$_3$ compound at different temperatures.

Table 1.4.1. Atomic coordinates of AlFeO₃ at 300 K

Atoms	x/a	y/b	z/c	B_{iso}	Occ.
300 K					
Space Group: *Pna2₁* (Orthorhombic), a = 4.9806(3) Å , b = 8.5511(6) Å, and c = 9.2403(6) Å					
Fe1/Al	0.1876(6)	0.1502(4)	0.5827(9)	0.20(2)	0.83(2)/ 0.17(2)
Fe2/Al	0.6646(3)	0.0320(3)	0.7998(9)	0.38(3)	0.81(1) /0.19(1)
Al1/Fe	0.1686(2)	0.1545(3)	0.00000(0)	0.56(2)	0.85(1)/ 0.14(1)
Al2/Fe	0.8164(7)	0.1613(3)	0.3098(4)	0.56(4)	0.74(2)/ 0.26(2)
O1	0.8164(7)	0.1613(3)	0.3098(4)	0.53(5)	1.0
O2	0.9824(5)	0.3218(9)	0.4201(2)	0.53(3)	1.0
O3	0.5073(2)	0.4905(7)	0.4331(5)	0.80(2)	1.0
O4	0.6620(9)	0.0047(9)	0.2040(8)	0.50(1)	1.0
O5	0.1418(5)	0.1630(7)	0.1984(6)	0.66(2)	1.0
O6	0.8372(5)	0.1652(6)	0.6767(1)	0.50(3)	1.0
χ^2	2.13%				
R_p	5.49%				
R_{wp}	6.42%				
R_{exp}	4.40%				
R_{Bragg}	2.04%				

Table 1.4.2. Atomic coordinates of Al₀.₅Ga₀.₅FeO₃ at 300 K

Atoms	x/a	y/b	z/c	B_{iso}	Occ.
300 K					
Space Group: *Pna2₁* (Orthorhombic), a = 5.0306(1)Å , b = 8.6461(2) Å, and c = 9.3175(2)Å					
Fe1/Al/Ga	0.1894(8)	0.1547(7)	0.5829(7)	0.23(2)	0.73(2)/0.16(2)/0.11(2)
Fe2/Al/Ga	0.6721(2)	0.0327(5)	0.7987(9)	0.41(5)	0.71(1)/0.14(1)/0.15(1)
Al1/Ga/Fe	0.1775(5)	0.1513(9)	0	0.52(7)	0.43(2)/0.37(1)/0.20(1)
Al2/Ga/Fe	0.8119(7)	0.1620(9)	0.3050(1)	0.47(3)	0.35(2)/0.34(2)/0.31(2)
O1	0.9768(2)	0.3270(4)	0.4190(9)	0.61(5)	1.0
O2	0.5200(9)	0.4874(9)	0.4356(4)	0.87(6)	1.0
O3	0.6479(2)	0.0002(1)	0.2009(1)	0.59(9)	1.0
O4	0.1556(4)	0.1595(1)	0.1960(8)	0.58(3)	1.0
O5	0.8390(2)	0.1675(2)	0.6703(1)	0.61(9)	1.0
O6	0.5011(2)	0.1696(1)	0.9379(1)	0.44(7)	1.0
χ^2	3.32 %				
R_p	7.80 %				
R_{wp}	8.54 %				
R_{exp}	4.40%				
R_{Bragg}	3.34%				

Crystal structure consists of four cation sites two predominantly occupied by Fe in and the other by A-site cation (Al/Ga). These sites are name Fe1, Fe2, A1 and A2 respectively. Out of these Fe1, Fe2 and A2 are in octahedral oxygen environment

whereas A1 is in a tetrahedral environment. As can be seen from the Fig.1.4.3, octahedra are connected by edges while tetrahedra by corners.
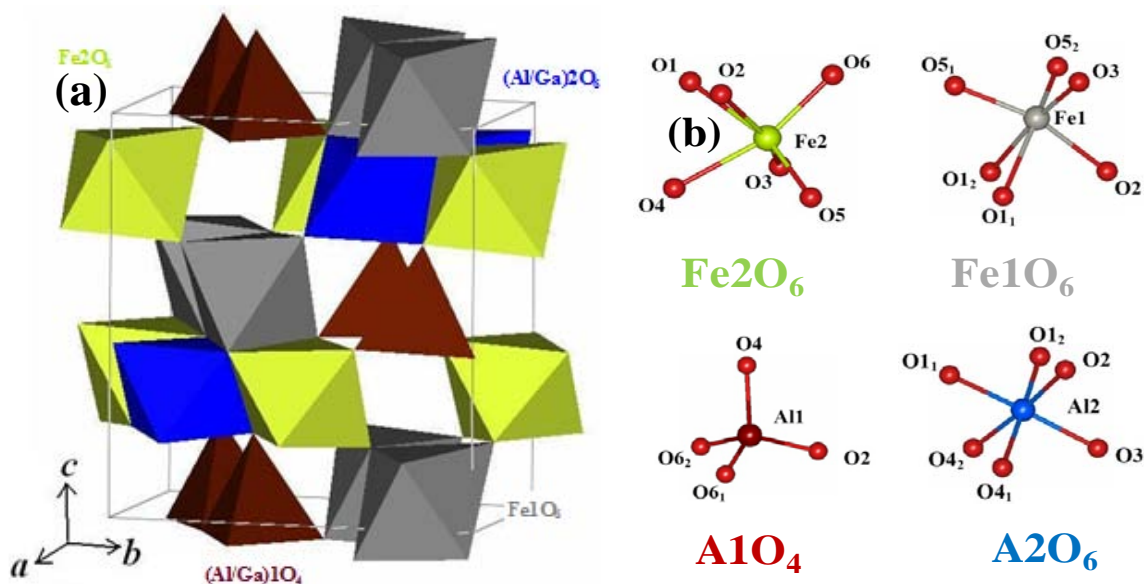
Fig.1.4.3: (a) Crystal structure of Al$_{1-x}$Ga$_x$FeO$_3$ is shown as determined from neutron diffraction measurements. (b) Four crystallographic sites, Fe1, Fe2, A1 and A2 are shown. As can be seen Fe1, Fe2 and A2 are octahedral and A1 is tetrahedral

Table 1.4.3. Bond lengths & Bond Angles of AlFeO$_3$: (300 K)

Site	Bond Length		Bond Angles	
Fe1	Fe1-O1$_1$*	2.337(11)	O1$_2$-Fe1-O3	174.4(8)
	Fe1-O1$_2$*	2.115(12)	O1$_1$-Fe1-O5$_2$	158.2(8)
	Fe1-O2	2.041(14)	O2-Fe1-O5$_1$	161.3(10)
	Fe1-O3	1.890(11)		
	Fe1-O5$_1$	1.954(11)		
	Fe1-O5$_2$	1.950(11)		
	Fe2-O1	2.236(10)	O1-Fe2-O5	165.0(8)
	Fe2-O2	2.076(14)	O2-Fe2-O3	158.8(10)
	Fe2-O3	1.879(11)	O4-Fe2-O6	163.8(9)
	Fe2-O4	2.142(11)		

Site	Bond Length		Bond Angles	
	Fe2-O5	1.824(11)		
	Fe2-O6	1.960(13)		
A1	Al1-O2	1.767(15)	O2-Al1-O4	110.1(10)
	Al1-O4	1.840(10)	O2-Al1-O6$_1$	115.7(10)
	Al1-O6$_1$	1.743(14)	O2-Al1-O6$_2$	108.3(9)
	Al1-O6$_2$	1.780(14)	O4-Al1-O6$_1$	112.1(10)
			O4-Al1-O6$_2$	103.7(9)
			O6$_1$-Al1-O6$_2$	106.0(10)
A2	Al2-O1$_1$	1.900(14)	O1$_1$-Al2-O3	179.0(10)
	Al2-O1$_2$	1.956(14)	O1$_2$-Al2-O4$_1$	175.3(9)
	Al2-O2	1.972(16)	O2-Al2-O4$_2$	173.0(10)
	Al2-O3	1.827(14)		
	Al2-O4$_1$	1.920(13)		
	Al2-O4$_2$	2.018(14)		

Table 1.4.4.Bond lengths & Bond Angles of $Al_{0.5}Ga_{0.5}FeO_3$: (300 K)

Site	Bond Length		Bond Angles	
Fe1	Fe1-O1$_1$	2.386(11)	O1$_2$-Fe1-O3	174.1(9)
	Fe1-O1$_2$	2.108(12)	O1$_1$-Fe1-O5$_2$	157.0(9)
	Fe1-O2	2.03 (13)	O2-Fe1-O5$_1$	161.5(10)
	Fe1-O3	1.917(12)		
	Fe1-O5$_1$	1.945(12)		
	Fe1-O5$_2$	1.894(12)		
Fe2	Fe2-O1	2.232(11)	O1-Fe2-O5	165.7(9)
	Fe2-O2	2.044(13)	O2-Fe2-O3	157.9(10)
	Fe2-O3	1.872(12)	O4-Fe2-O6	163.9(9)
	Fe2-O4	2.104(11)		
	Fe2-O5	1.87(12)		
	Fe2-O6	1.957(13)		

A1 	(Al/Ga)1-O2	1.833(12)	O2-(Al/Ga)1-O4	108.9(9)
	(Al/Ga)1-O4	1.831(7)	O2-(Al/Ga)1-O6$_1$	118.1(9)
	(Al/Ga)1-O6$_1$	1.734(13)	O2-(Al/Ga)1-O6$_2$	106.3(8)
	(Al/Ga)1-O6$_2$	1.875(12)	O4-(Al/Ga)1-O6$_1$	112.6(9)
			O4-(Al/Ga)1-O6$_2$	104.3(8)
			O6$_1$-(Al/Ga)1-O6$_2$	105.5(9)
A2 	(Al/Ga)2-O1$_1$	1.962 (13)	O1$_1$-(Al/Ga)2-O3	178.0(10)
	(Al/Ga)2-O1$_2$	1.995 (13)	O1$_2$-(Al/Ga)2-O4$_1$	177.2(9)
	(Al/Ga)2-O2	2.061 (14)	O2-(Al/Ga)2-O4$_2$	168.4(10)
	(Al/Ga)2-O3	1.892 (13)		
	(Al/Ga)2-O4$_1$	2.008 (13)		
	(Al/Ga)2-O4$_2$	2.006 (13)		

Table 1.4.5. Bond angles and cation-cation distances of AlFeO$_3$:

Bond Angles		Cation-Cation Distance	
Fe1-O1$_2$-Fe2	165.5(6)	Fe1-Fe2	4.539(6)
Fe1-O1$_1$-Al2	162.3(9)	Fe1-Al2	4.018(8)
Fe1-O2-Al1	116.7(9)	Fe1-Al1	3.246(12)
Fe2-O2-Al1	117.6(8)	Fe2-Al1	3.291(11)
Al1-O2-Al2	119.0(10)	Al1-Al2	3.224(15)
Fe1-O3-Fe2	120.3(7)	Fe1-Fe2	3.269(10)
Fe1-O3-Al2	131.6(9)	Fe1-Al2	3.390(12)
Al1-O4-Al2	126.6(8)	Al1-Al2	3.359(12)
Al1-O4-Al2	120.4(8)	Al1-Al2	3.348(12)
Fe1-O5-Fe2	131.1(7)	Fe1-Fe2	3.439(10)
Fe1-O5-Fe2	127.1(7)	Fe1-Fe2	3.379(9)
Fe2-O6-Al1	123.2(8)	Fe2-Al1	3.258(11)

Table 1.4.6. Bond angles and cation-cation distances of $Al_{0.5}Ga_{0.5}FeO_3$:

Bond Angles		Cation-Cation Distance	
Fe1-O1$_2$-Fe2	165.8 (6)	Fe1-Fe2	4.582(9)
Fe1-O1$_1$-(Al/Ga)2	164.1 (8)	Fe1-(Al/Ga)2	4.063(12)
Fe1-O2-(Al/Ga)1	118.4 (8)	Fe1-(Al/Ga)1	3.319(11)
Fe2-O2-(Al/Ga)1	117.8 (7)	Fe2-(Al/Ga)1	3.322(10)
(Al/Ga)1-O2-(Al/Ga)2	113.8 (8)	(Al/Ga)1-(Al/Ga)2	3.263(11)
Fe1-O3-Fe2	122.7 (7)	Fe1-Fe2	3.324(10)
Fe1-O3-(Al/Ga)2	128.7 (8)	Fe1-(Al/Ga)2	3.434(11)
(Al/Ga)1-O4-(Al/Ga)2	123.8 (7)	(Al/Ga)1-(Al/Ga)2	3.387(11)
(Al/Ga)1-O4-(Al/Ga)2	120.8 (7)	(Al/Ga)1-(Al/Ga)2	3.337(11)
Fe1-O5-Fe2	129.7 (7)	Fe1-Fe2	3.454 (10)
Fe1-O5-Fe2	127.1 (8)	Fe1-Fe2	3.369 (9)
Fe2-O6-(Al/Ga)1	125.3 (8)	Fe2-(Al/Ga)1	3.281(10)
Fe2-O6-(Al/Ga)1	119.7 (9)	Fe2-(Al/Ga)1	3.313(9)

Octahedra are highly distorted whereas tetrahedra are mostly regular. This distortions of the polyhedra are mainly due to difference in the ionic radii of Fe^{3+} and A-site cations (Al^{3+}/Ga^{3+}). These distortions have been calculated as

$$\Delta = (1/N)\sum_{1}^{N}\{(d_N - <d>)/<d>\}^2$$

where (Δ) is the distortion parameter of a coordination polyhedron AO_N (A: Fe1, Fe2, A1, and A2) and $<d>$ id the average value of the A-O bond length (Fig.1.4.4).
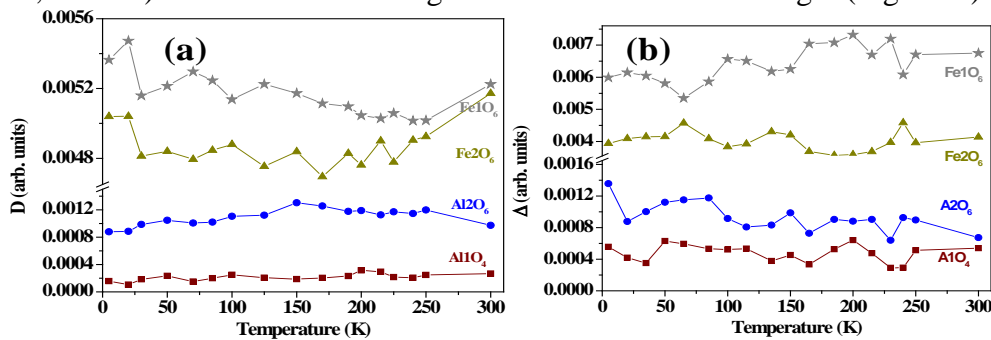
Fig.1.4.4: Distrotion parameters of polyhedra as a function of temperature for (a) $AlFeO_3$ and (b) $Al_{0.5}Ga_{0.5}FeO_3$.

Temperature dependence of lattice parameters show a dip around 150 K which signals negative thermal expansion (Fig.1.4.5.). Such expansion of lattices as the temperature is lowered is quite an unusual phenomenon.
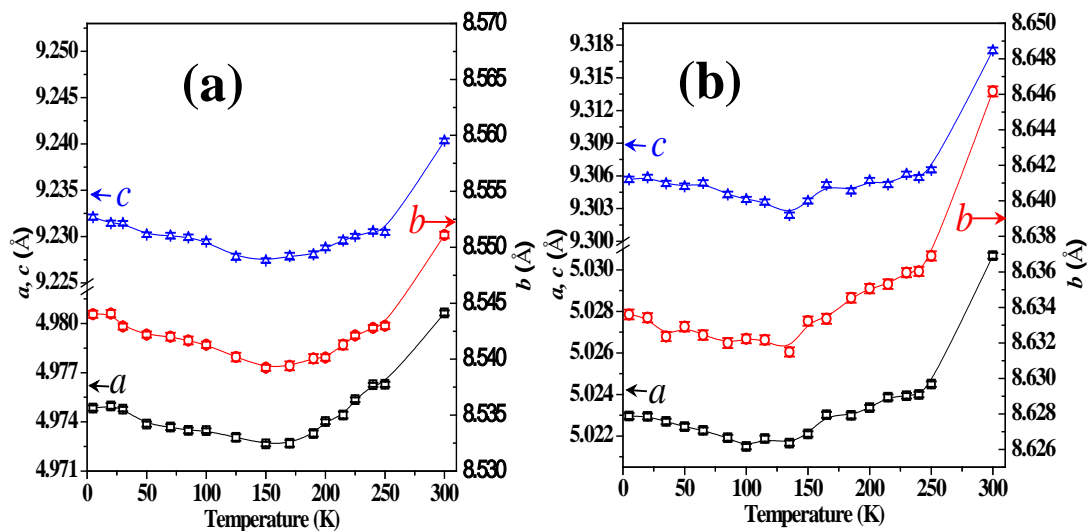
Fig. 1.4.5: (a) Variation of lattice parameters with temperature for (a) $AlFeO_3$ and (b) $Al_{0.5}Ga_{0.5}FeO_3$ is shown (b) Variation of unit cell volume of $Al_{0.5}Ga_{0.5}FeO_3$ with temperature is shown.
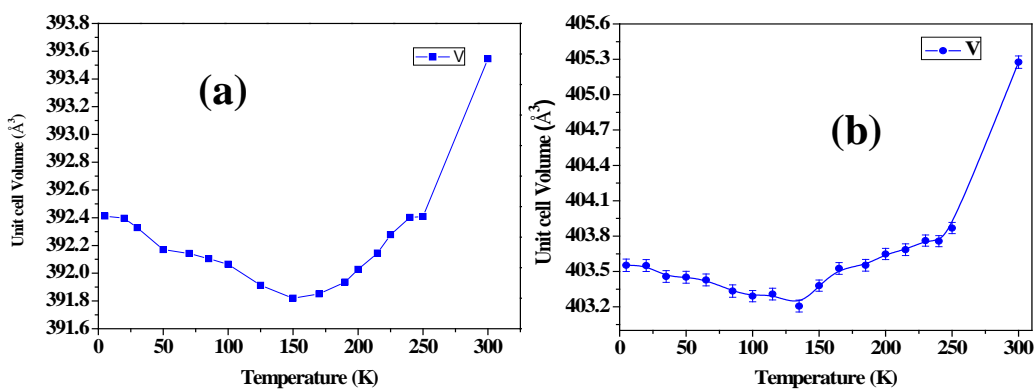
Fig. 1.4.6: Variation of unit cell volume of a) $AlFeO_3$ and (b) $Al_{0.5}Ga_{0.5}FeO_3$ with temperature is shown.

From neutron diffraction studies it is clear that $AlFeO_3$ and $Al_{0.5}Ga_{0.5}FeO_3$ crystallizes in the same space group and they show similar temperature dependent behavior. The only difference that exists is in terms of their site occupancy.

45

Magnetic structure was also determined from neutron diffraction studies. At lower temperatures fundamental Bragg peaks starts appearing suggesting ferrimagnetic structure. Magnetic structure is collinear ferrimagnetic in nature with the moments along the crystallographic *a* direction. Here Fe1 and A1 moments are parallel to each other whereas anti-parallel to Fe2 and A2 which are again parallel to each other (Fig.1.4.7.). The Néel sublattices being A = Fe1+ Ga1 and B = Fe2 + Ga2 with antiparallel moments.
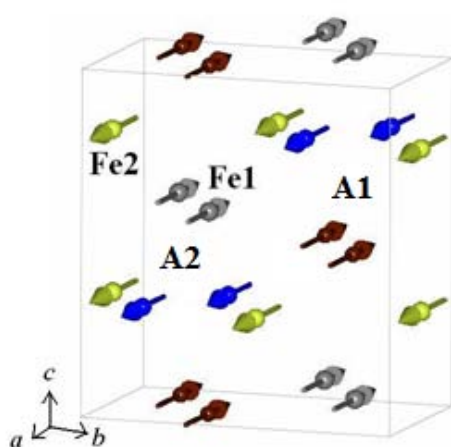
Fig.1.4.7: Magnetic structure of $Al_{0.5}Ga_{0.5}FeO_3$ showing two Néel sublattices being A = Fe1+ Ga1 and B = Fe2 + Ga2

Due to the mixed occupancy of cations in these crystallographic sites, site moments are unequal and hence a net moment results. Ordered moment for all the four sites of $Al_{0.5}Ga_{0.5}FeO_3$ are shown in Fig.1.4.8. Magnetic ordering occurs through cation-oxygen-cation antiferromagnetic interaction and it weakens as the bond-angle (180°) deviates. The important pathways for superexchange interaction are Fe1-[O1/O3/O5]-Fe2 and Fe1-[O1/O3]-A2.
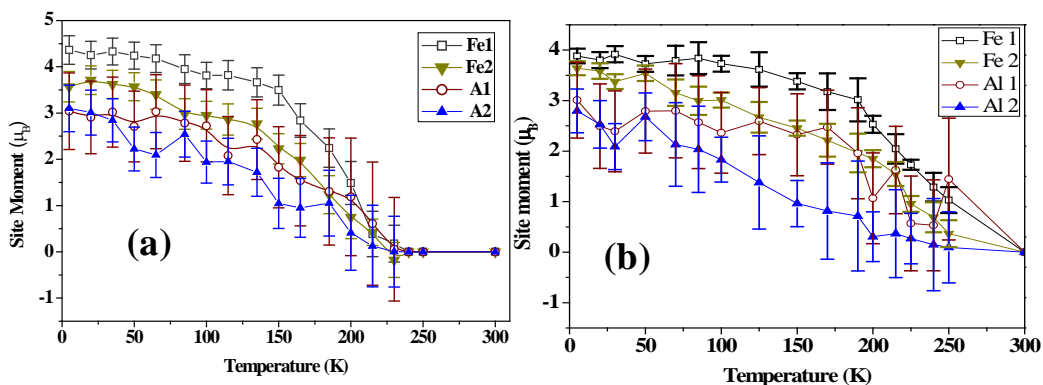
Fig.1.4.8. The temperature dependence of ordered site moments per Fe ion in Fe1, Fe2, A1 and A2 sites of (a)AlFeO$_3$ and (b) Al$_{0.5}$Ga$_{0.5}$FeO$_3$.

Evolution of magnetically important structural parameters like bond length and bond angles of Fe1-O1/O3/O5-Fe2 and Fe1-O1/O3-A2 with temperature are also studied carefully in Al$_{0.5}$Ga$_{0.5}$FeO$_3$ (Fig1.4.9.).

(1) Cases where the cations at the Fe1, and Fe2 sites connected via O5 ions; bond lengths (Fe1-O5 and Fe2-O5) and bond angles (Fe1-O5-Fe2).
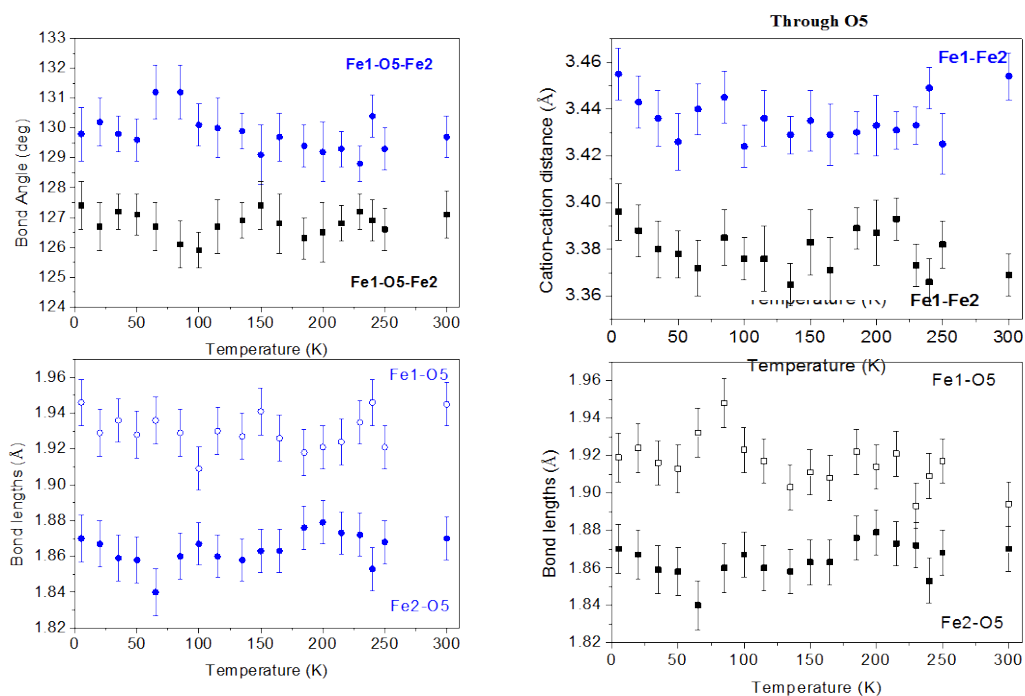
(2) Cases where the cations at the Fe1, Fe2, and Al2 sites connected via O3 ions; bond lengths (A-O3 and A´-O3) and bond angles (A-O3-A´) (where, A, A´ = Fe1, Fe2, and Al2 sites)
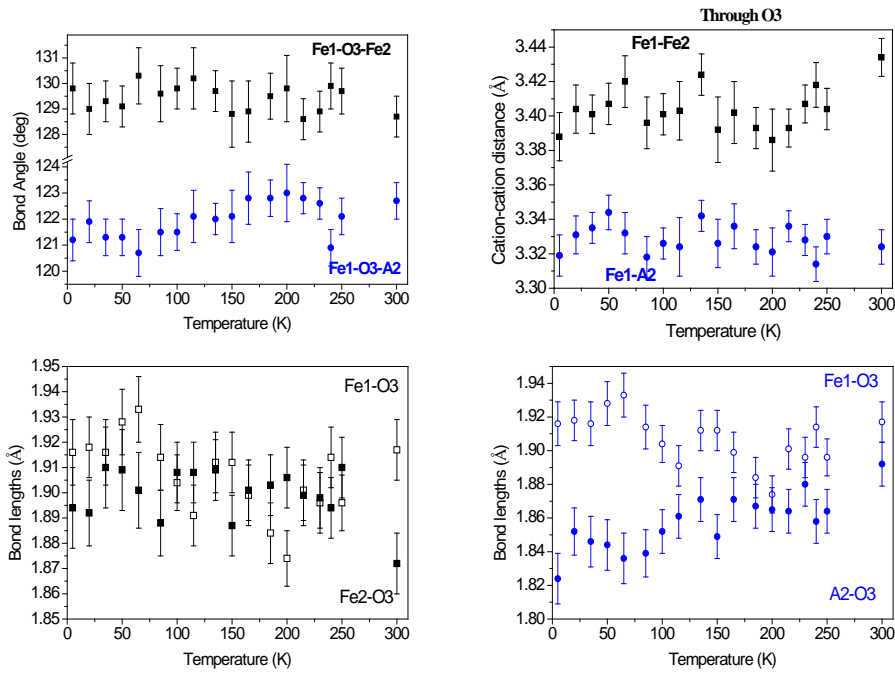
(3) Cases where the cations at the Fe1, Fe2, and Al2 sites are connected via O1 ions; bond lengths (*A*-O1 and *A´*-O1) and bond angles (*A*-O1-*A´*) (where, *A*, *A´* = Fe1, Fe2, and Al2 sites).
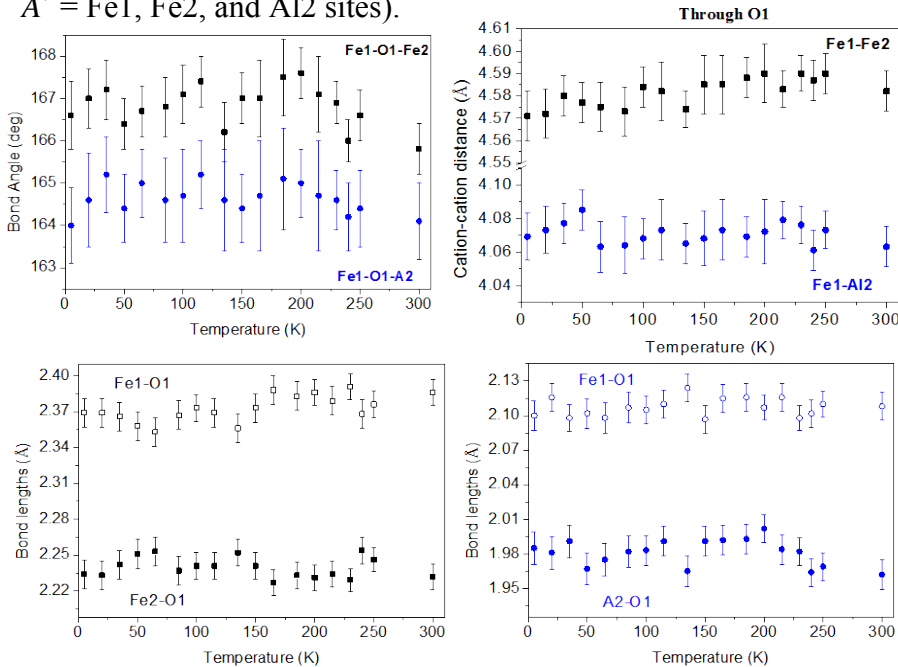
Fig.1.4.9: Evolution of magnetically important bond lengths and bond angles as a function of temperature is shown under different oxygen environments for Al$_{0.5}$Ga$_{0.5}$FeO$_3$.

1.4.1.2. Magnetic Properties

Magnetic measurements done on $AlFeO_3$ and $Al_{0.5}Ga_{0.5}FeO_3$ reveals a ferrimagnetic nature as have been predicted by neutron diffraction measurements. This ferrimagnetism arises from the mixed occupancy of cations in the available cationic sites. $AlFeO_3$ has a T_N of 233 K and $Al_{0.5}Ga_{0.5}FeO_3$ has a T_N of 220 K (Fig.1.4.10.). This decrease in T_N on Ga^{3+} introduction shows the weakening of magnetic interaction. This can be probably due the bigger size of Ga^{3+} ion.
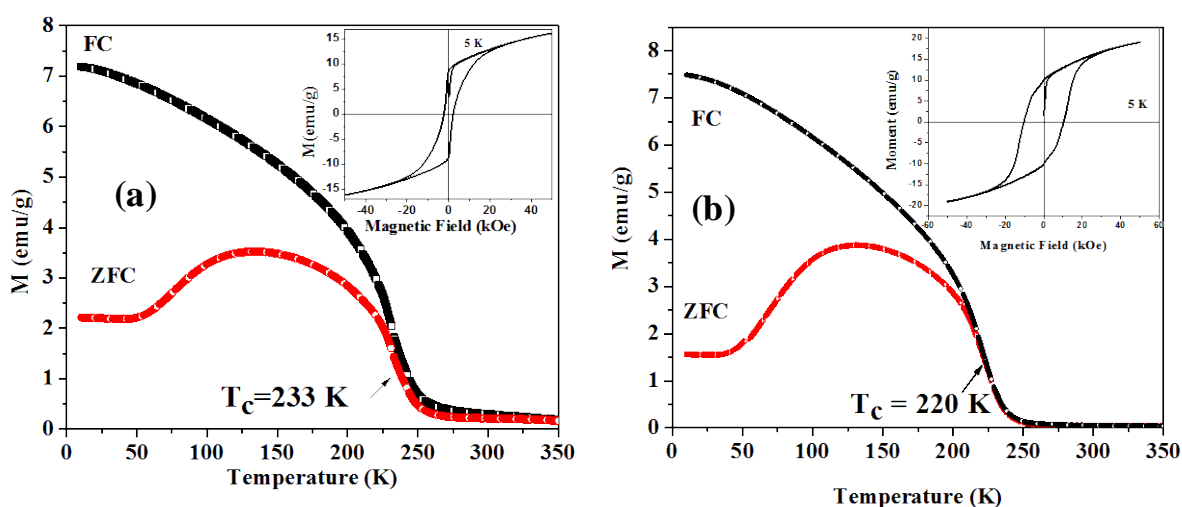
Fig1.4.10: Temperature dependent magnetization of (a) AlFeO₃ and (b) Al₀.₅Ga₀.₅FeO₃ under field- cooled (FC) and zero-field-cooled (ZFC) conditions are shown. Magnetic hysteresis at 5 K is shown in the inset.

Magnetic hysteresis measurements were done at 5 K for both the compounds and it shows a well saturated hysteresis curve. $AlFeO_3$ has a saturation magnetization (M_S) value of 16.03 emu/g, remanant magnetization (M_R) value of 9.05 emu/g and coercive field (H_C) of 12.9 kOe. On the other hand $Al_{0.5}Ga_{0.5}FeO_3$ shows a saturation magnetization (M_S) value of 19.07 emu/g, remanant magnetization (M_R) value of 10.02 emu/g and coercive field (H_C) of 10.26 kOe. These hysteresis curves show a pinched like shape which is commonly observed in exchange spring magnets with hard and soft magnetic centers. This has been earlier observed in $AlFeO_3$ [51,57]and

$GaFeO_3$[56]. In our samples this behavior is clearly seen in $AlFeO_3$. It has been explained [51,56,57] that the Fe in octahedral sites namely Fe1, Fe2 and A2 forms the hard phase with strong anisotropy and Fe occupying tetrahedral site forms the soft magnetic phase.

1.4.2. Phase transitions of $Al_{1-x}Ga_xFeO_3$ (0.0,0.5) on ball milling

$AlFeO_3$ samples were subjected to ball milling and interesting phase transitions were observed[67]. After 12 h of dry milling the x-ray diffraction pattern obtained was different from that of the parent crystallizing in $Pna2_1$ space group. This was different from that of α-Fe_2O_3 (R-3c) and 1:1 mixture of Al_2O_3 and Fe_2O_3 (Fig.1.4.11). This diffraction pattern could be indexed to $P2_12_12_1$ space group with lattice parameters a = 15.886 (11) Å, b = 11.408 (6) Å, and c = 7.803 (4) Å[67] (Fig.1.4.12a). Al_2O_3 is known to have a metastable phase crystallizing in the same space group $P2_12_12_1$ called δ-Al_2O_3[68]. This is a superstructure of a spinel with ordered cation vacancies and is different from δ^*-Al_2O_3 ($P222$)[69]. It is quite difficult to differentiate between these two phases from profile fitting. It is also possible that δ-Al_2O_3 of Levin and Brandon[68] could be same as δ^*-Al_2O_3 of Fargeot et al. Further milling the sample for 24 hours transformed it into R-$3c$ space group with a corundum structure[67]. It has lattice parameters a = 4.909(2) Å and c = 13.393(7) Å (Fig.1.4.12b). This is similar to the most stable structure of α-Al_2O_3. This phase transition was reversible and bulk $Pna2_1$ space group could be re-obtained by annealing the sample at 1623 K.
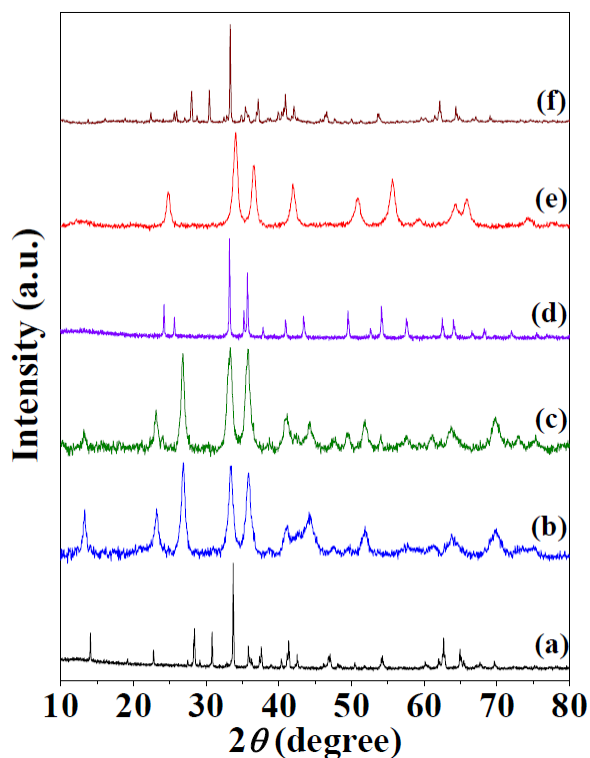
Fig.1.4.11: X-ray diffraction patterns are shown for (a) Orthorhombic AlFeO$_3$ sample; (b) ball-milled AlFeO$_3$ (12 h); (c) 12 h ball-milled AlFeO$_3$ annealed at 973 K; (d) mixture of α-Fe$_2$O$_3$ + α-Al$_2$O$_3$ (1:1) and (e) ball-milled AlFeO$_3$ (24 h) and (f) ball-milled AlFeO$_3$ annealed at 1623 K.
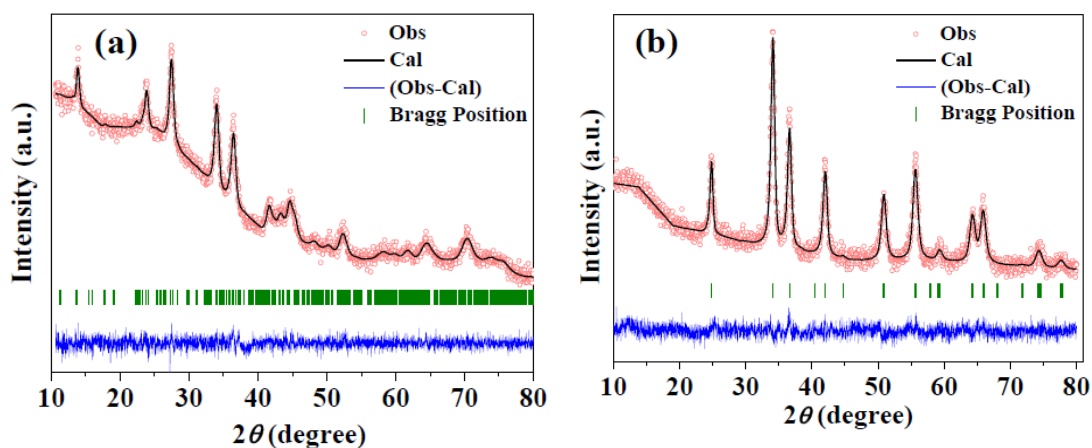
Fig.1.4.12: XRD patterns for ball-milled AlFeO$_3$ in (a) δ-Al$_2$O$_3$ structure (P2$_1$2$_1$2$_1$) and (b) R -3c structure along with profile fits.

Raman spectra were recorded on these samples and phase transition was observed. Raman spectra of the sample ball milled for 12 h is distinct from that of

parent sample and it remained the same when the sample was annealed to 973 K. Further ball milling for 24 h showed different raman spectra signaling a different phase (Fig.1.4.13).
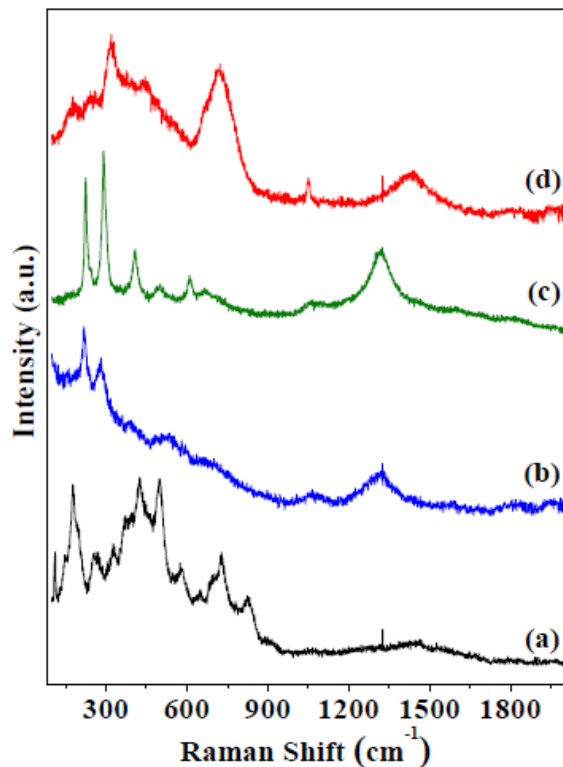
Fig.1.4.13:Raman spectra is shown for (a) Orthorhombic AlFeO₃ sample; (b) ball-milled AlFeO₃ (12 h) ;(c) 12 h ball-milled AlFeO₃ annealed at 973 K and (d) ball-milled AlFeO₃ (24 h).

Magnetic studies were carried out for all these samples and it was found that these are quite different from that of parent AlFeO₃ sample with a ferromagnetic transition around 233 K. The sample crystallizing in $P2_12_12_1$ space group showed divergence in FC and ZFC measurements below 390 K (Fig.1.4.14a) and a hysteresis at 5K whereas the sample crystallizing in *R-3c* space group show a ferromagnetic transition at 225 K (Fig.1.4.14b), which is lower than that of the parent compound[67].
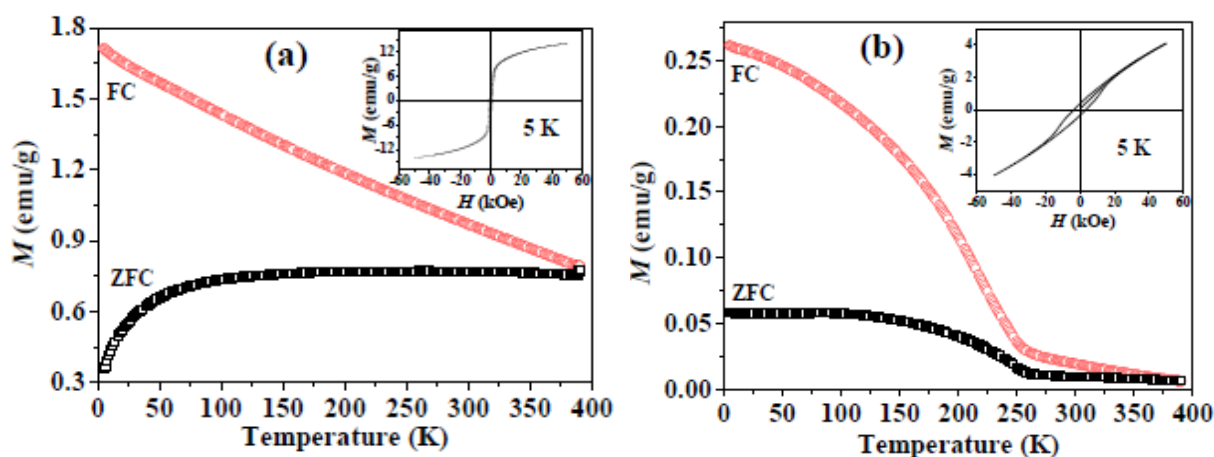
Fig.1.4.14: Magnetization is plotted as a function of temperature for ball-milled AlFeO$_3$ in the (a) P2$_1$2$_1$2$_1$ and (b) R -3c structures under field-cooled (FC) and zero-field cooled (ZFC) conditions. Magnetic hysteresis measured at 5 K is shown in the inset

Ball milling of Al$_{0.5}$Ga$_{0.5}$FeO$_3$ was done to reduce the particle size but dry milling resulted in interesting phase transition. Fig.1.4.15 shows the XRD patterns of ball milled Al$_{0.5}$Ga$_{0.5}$FeO$_3$ along with the bulk Al$_{0.5}$Ga$_{0.5}$FeO$_3$ and a mixture of (Fe$_2$O$_3$+Al$_2$O$_3$+Ga$_2$O$_3$) in the ratio (1:0.5:0.5). It can be seen that there is considerable difference in the XRD patterns. XRD pattern of the ball milled sample is quite different from bulk as well as from the mixture. This shows that the sample has not phase separated but have stabilized in some other phase which is probably a metastable phase.

The XRD pattern of the ball milled sample could be indexed to the *R-3c* space group with lattice parameters *a* = 4.970(1) Å and *c* = 13.509(3) Å (Fig.1.4.16). Annealing of the sample shows that this metastable phase is stable only upto 973 K. Further annealing of the sample to a temperature as high as 1473 K reverts it back to the bulk *Pna2$_1$* structure. Line broadening seen in the XRD pattern signifies that the

particle size have been reduced. Using Debye-Scherrer formula the crystallite size calculated was found to be 25 nm.
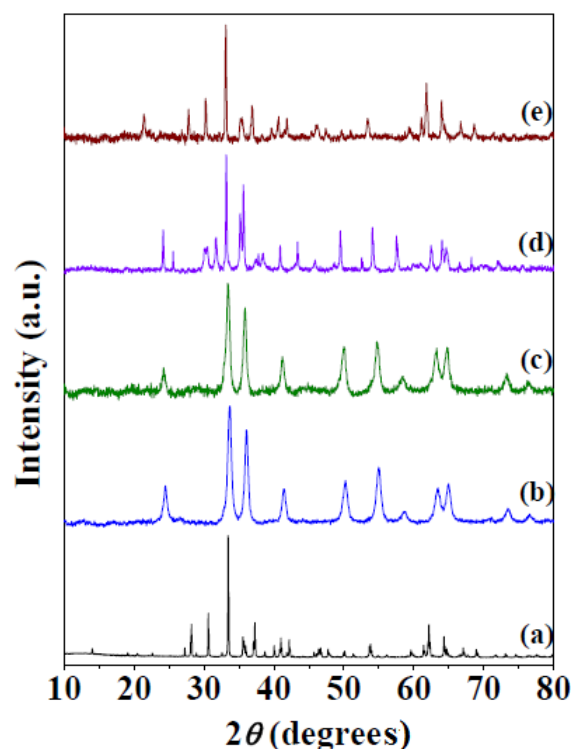
Fig.1.4.15: XRD patterns are shown for (a) the orthorhombic $Al_{0.5}Ga_{0.5}FeO_3$ sample, (b) ball-milled $Al_{0.5}Ga_{0.5}FeO_3$, (c) ball-milled $Al_{0.5}Ga_{0.5}FeO_3$ annealed at 973 K, (d) a mixture of $Fe_2O_3+Al_2O_3+Ga_2O_3$ (1:0.5:0.5), and (e) ball-milled $Al_{0.5}Ga_{0.5}FeO_3$ annealed at 1473 K.
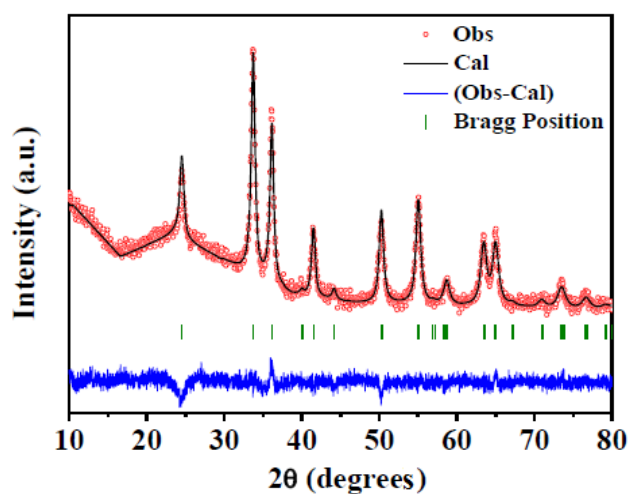
Fig.1.4.16: XRD pattern of ball-milled $Al_{0.5}Ga_{0.5}FeO_3$ in the R-3c structure along with profile fit, difference pattern and Bragg positions is shown.
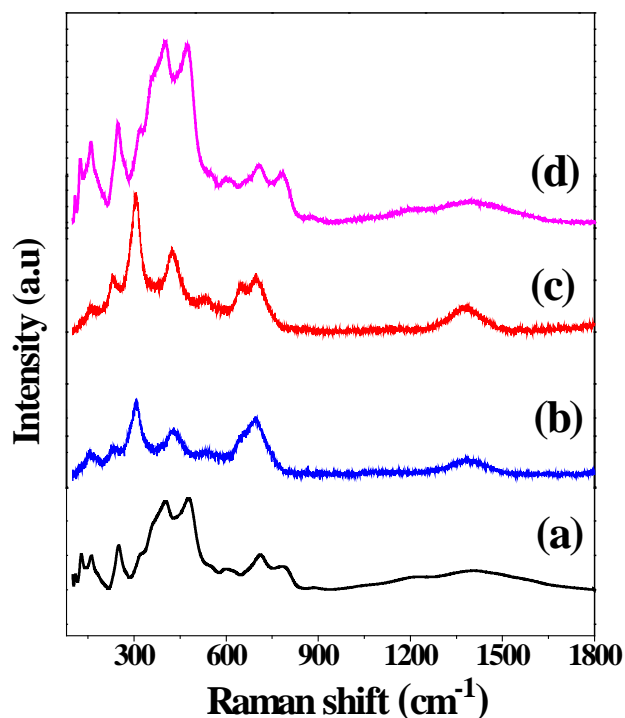
Fig.1.4.17: Raman spectra for (a) the orthorhombic Al$_{0.5}$Ga$_{0.5}$FeO$_3$ sample, (b) ball-milled Al$_{0.5}$Ga$_{0.5}$FeO$_3$, (c) ball-milled Al$_{0.5}$Ga$_{0.5}$FeO$_3$ annealed at 973 K and (d) ball-milled Al$_{0.5}$Ga$_{0.5}$FeO$_3$ annealed at 1473 K.

Raman analysis of the sample were done in LabRAM HR 800 high-resolution Raman spectrometer (HORIBA-Jobin Yvon) using a He-Ne laser (λ = 632.8 nm) to confirm the phase transition as well as the reversibility associated with it. It was in corroboration with the XRD results it shows that ball milled sample had a spectra different from that of the bulk, which on annealing to 1473 K reverts back to bulk spectra with some line broadening (Fig.1.4.17).

DC magnetization measurements were carried out under zero-field-cooled (ZFC) and field-cooled (FC) condition using a vibrating sample magnetometer in Physical Property Measurement System (PPMS) in the temperature range of 5 to 390 K under a magnetic field of 100 Oe. Magnetic hysteresis curves were recorded at 5 K. The magnetic behaviour is quite different from that of bulk Al$_{0.5}$Ga$_{0.5}$FeO$_3$ as we do not see the sharp ferrimagnetic transition at 220 K. Instead, we see a divergence

55

between FC and ZFC data below 320 K, with a narrower hysteresis at 5 K. In Fig. 1.4.18 the temperature dependence of magnetization of ball-milled $Al_{0.5}Ga_{0.5}FeO_3$ under FC (field-cooled) and ZFC (zero-field cooled) conditions is shown.
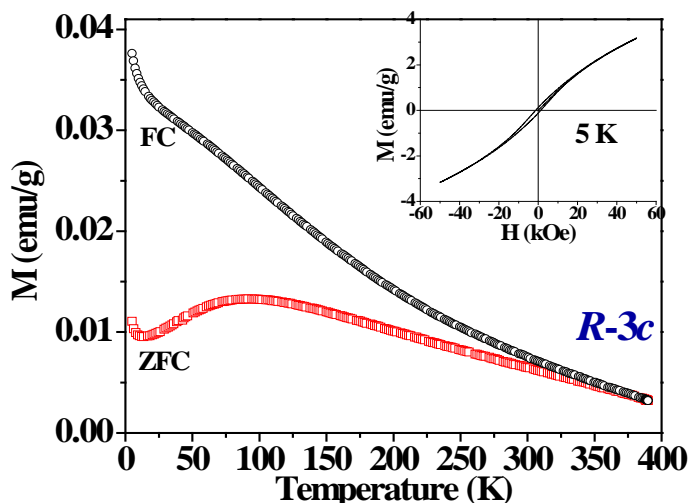
Fig.1.4.18: Temperature dependent magnetization of ball-milled $Al_{0.5}Ga_{0.5}FeO_3$ under field-cooled (FC) and zero-field cooled (ZFC) conditionsis shown. Magnetic hysteresis at 5 K is shown in the inset.

Ball milling of $AlFeO_3$ proceeds through two intermediate phases involving $P2_12_12_1$ and R-3c phases. $P2_12_12_1$ phase disappears as Ga^{3+} ions are introduced into the system. This shows the concentration of cations does have a role to play in dictating the pathway of phase transition.

Theoretically, Waghmare *et.al.,* predicts a similar phase transition involving intermediate phases possible when pressure is applied. It has also been pointed out that this critical pressure can reduce when disorder is incorporated into the system. Thus this phase transformation cannot be explained only by pressure effects but rather by disorder kinetics.

1.4.3. Effect of Doping of Mn ions in GaFeO₃

Site-specific doping of $GaFeO_3$ has been achieved by two step solid state reaction. In the first step, Mn^{3+} was introduced into the Fe or Ga site as the case may be. Mn doped in the Fe site could be indexed to α-Fe_2O_3 and Mn doped in Ga site could be indexed to β-Ga_2O_3 (Fig.1.4.19).
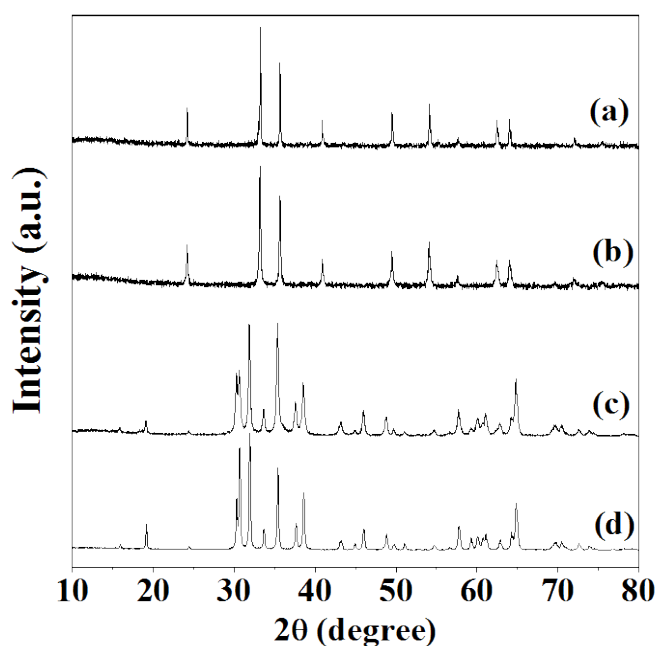
Fig.1.4.19: XRD patterns of (a) $(Fe_{0.9}Mn_{0.1})_2O_3$ (b) Fe_2O_3 (c) $(Ga_{0.9}Mn_{0.1})_2O_3$ and (d) Ga_2O_3.
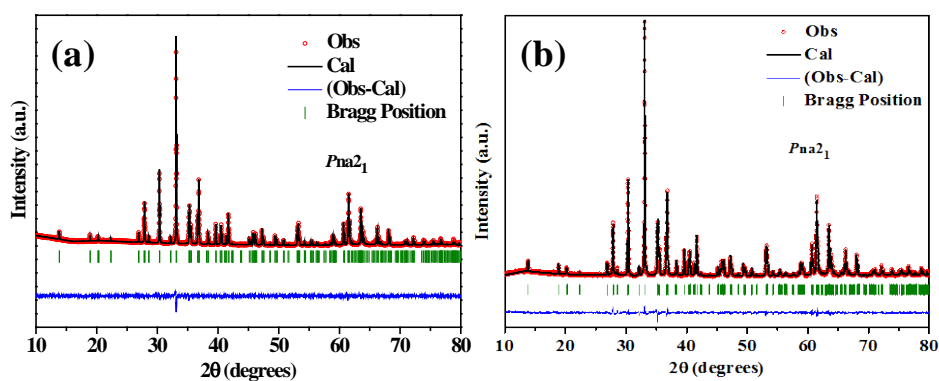
Fig.1.4.20: XRD patterns of (a) $GaFe_{0.95}Mn_{0.05}O_3$ and (b) $GaFe_{0.9}Mn_{0.1}O_3$ along with profile fits, difference patterns and Bragg positions.

In the second step, Mn-doped into the Fe site (x = 0.5, 1.0) is made to react with β-Ga$_2$O$_3$ (Fig.1.4.20) and Mn-doped into the Ga site (x = 0.5, 1.0) is made to react with α-Fe$_2$O$_3$ .This yielded phase pure compounds which could be indexed to the *Pna*2$_1$ space group in which GaFeO$_3$ crystallizes (Fig.1.4.21).
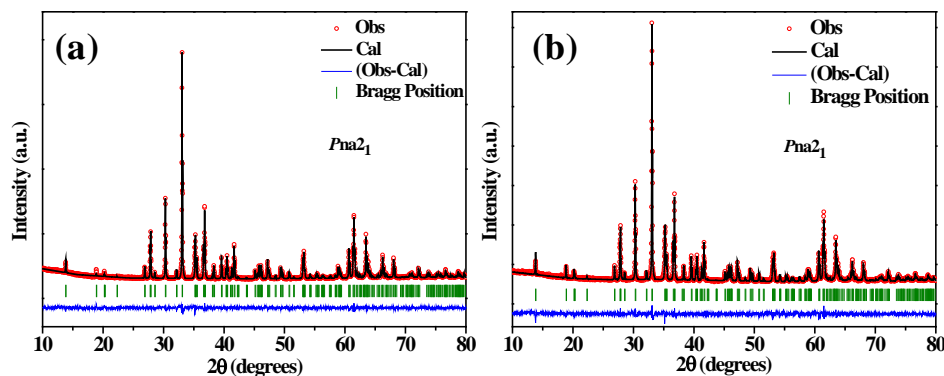
Fig.1.4.21: XRD patterns of (a) Ga$_{0.95}$Mn$_{0.05}$FeO$_3$ and (b) Ga$_{0.9}$Mn$_{0.1}$FeO$_3$ along with profile fits, difference patterns and Bragg positions.
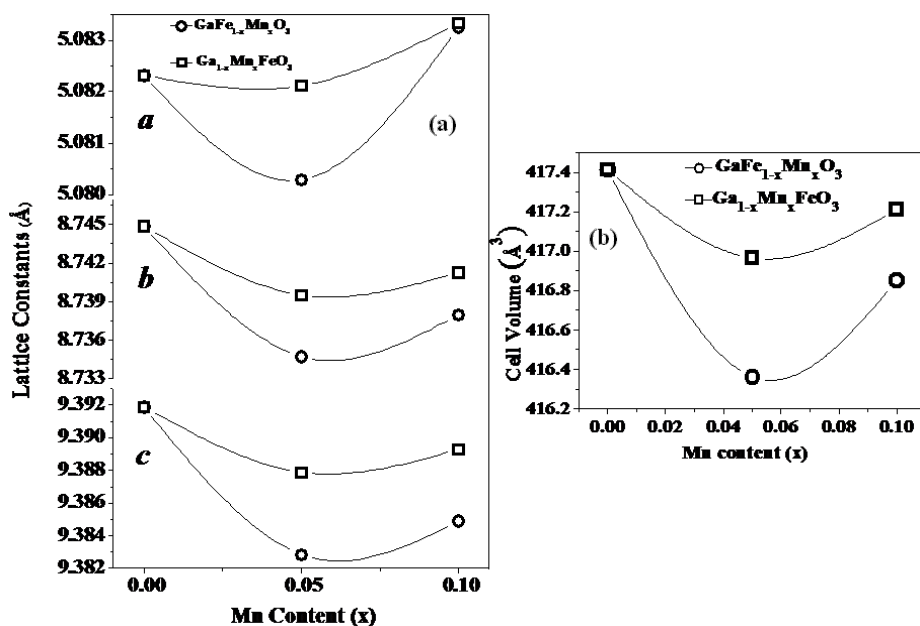
Fig.1.4.22: (a) Variation of lattice parameters is plotted as a function of Mn concentration for both Ga$_{1-x}$Mn$_x$FeO$_3$ and GaFe$_{1-x}$Mn$_x$O$_3$ (b) Unit cell parameters as a function of Mn content is shown.

Unit cell parameters of GaFe$_{1-x}$Mn$_x$O$_3$ and Ga$_{1-x}$Mn$_x$FeO$_3$ along with their unit cell volumes are plotted as a function of Mn content in Fig.1.4.22. The changes

in the lattice parameters indicate that the introduction of Mn^{3+} causes distortion in the lattice due to the difference in the ionic radii of Fe(III), Ga(III) and Mn(III). There are no observable trends in this variation. Ionic radii of Fe(III) in the high spin stat ($t_{2g}^3 e_g^2$) is found to be 0.645 Å and 0.55 Å in the low spin state ($t_{2g}^5 e_g^0$) . Ionic radii of Ga(III) is found to be 0.62 Å. The dopant Mn(III) has an ionic radii of 0.65 Å in the high spin state and 0.58 Å in the low spin state[55]. Thus, depending on the spin of the dopant the ionic size may vary and this can be a probable explanation for the absence of any trends in the unit cell parameters.

Introduction of Mn^{3+} in the system in Fe site is found to decrease the T_N of $GaFeO_3$ from 210 K to 162 K on 10 % doping (Fig.1.4.23). Saturation magnetization and remanant magnetization are also found to decrease as the amount of Mn increases. As Mn^{3+} ions are introduced, new magnetic interaction pathways namely, Mn^{3+}-O^{2-}-Mn^{3+} and Fe^{3+}-O^{2-}-Mn^{3+} are introduced[70]. These interactions are weaker than Fe^{3+}-O^{2-}-Fe^{3+} and therefore as Fe-Fe linkages reduces in number, T_N, saturation magnetization and remanant magnetization are liable to decrease.
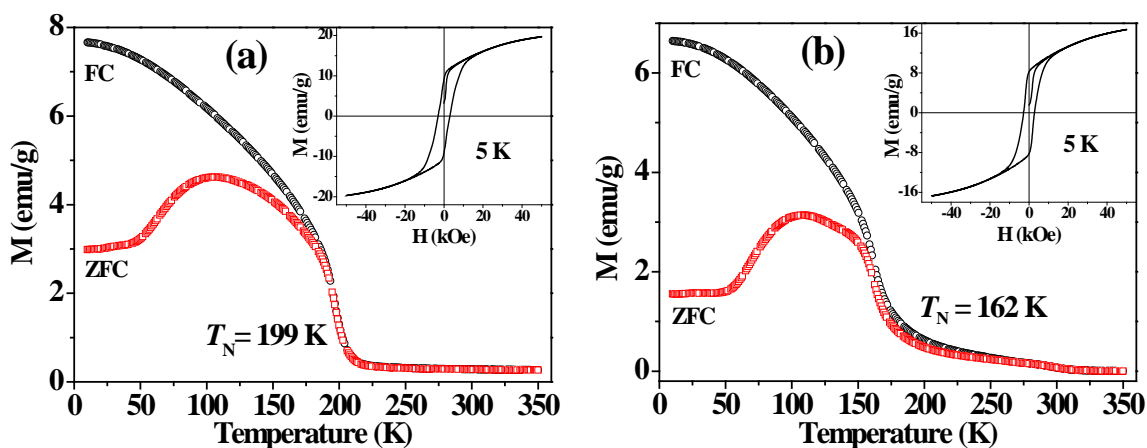
Fig.1.4.23: Temperature-dependent magnetization of (a) $GaFe_{0.95}Mn_{0.05}O_3$ and (b) $GaFe_{0.9}Mn_{0.1}O_3$ under field-cooled (FC) and zero-field-cooled (ZFC) conditions. Magnetic hysteresis at 5 K is shown in the inset.

On the contrary, introducing Mn^{3+} for Ga^{3+} will not significantly affect the magnetic properties as Ga^{3+} which is being replaced is non-magnetic (Fig.1.4.24). There will be as expected a small increase in saturation magnetization and remanant magnetization due to the introduction of magnetic Mn^{3+} ion (Fig.1.4.25).
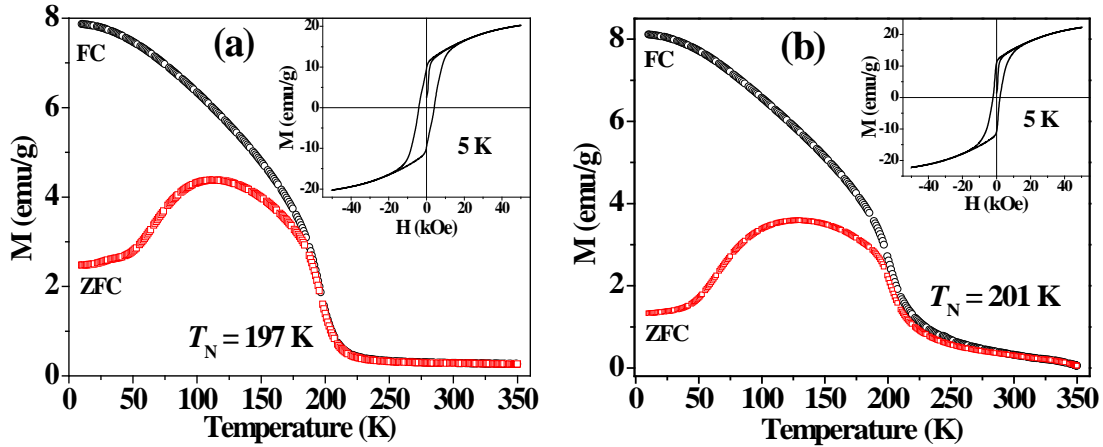
Fig.1.4.24: Temperature-dependent magnetization of (a) $Ga_{0.95}Mn_{0.05}FeO_3$ and (b) $Ga_{0.9}Mn_{0.1}FeO_3$ under field-cooled (FC) and zero-field-cooled (ZFC) conditions. Magnetic hysteresis at 5 K is shown in the inset.
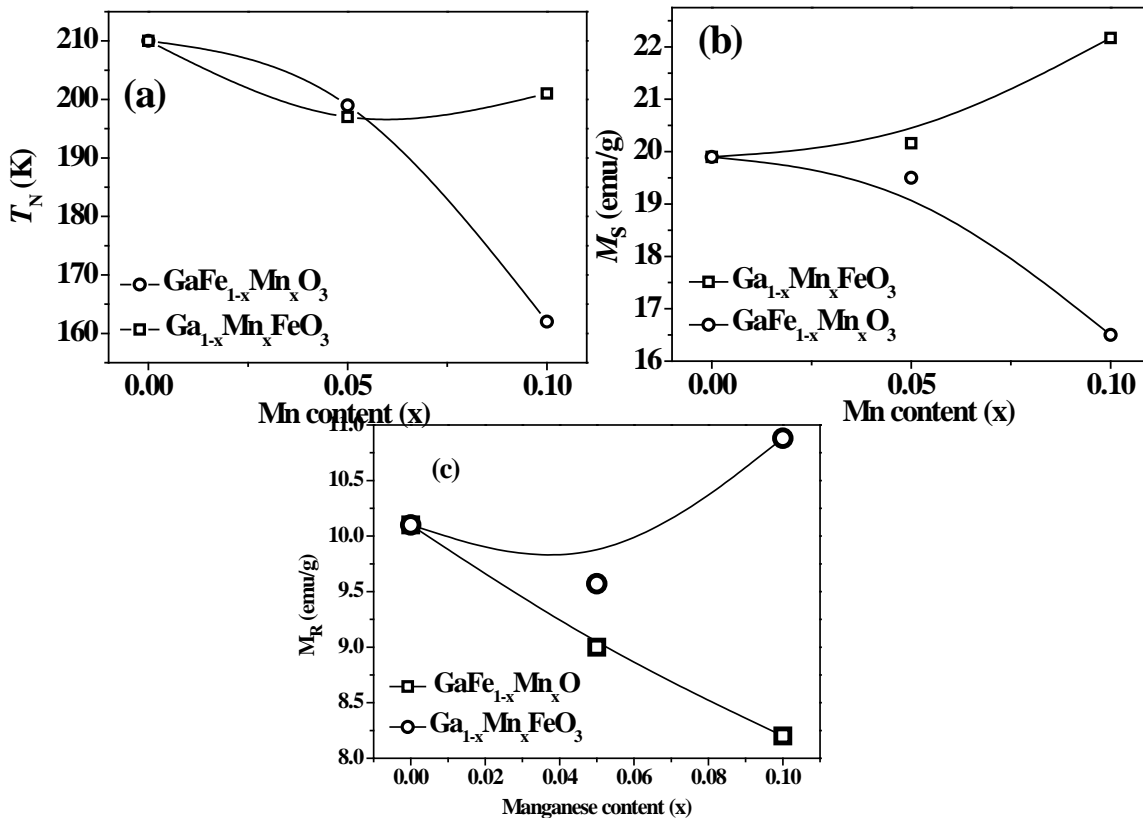
Fig.1.4.25: (a) Variation of the Néel temperature (T_N) with Mn concentration for

$GaFe_{1-x}Mn_xO_3$ (x = 0.05 and 0.1) and $Ga_{1-x}Mn_xFeO_3$ (x = 0.05 and 0.1) and (b) Variation of M_S with Mn concentration for $GaFe_{1-x}Mn_xO_3$ (x = 0.05 and 0.1) and $Ga_{1-x}Mn_xFeO_3$ (x = 0.05 and 0.1). (c) Variation of M_R with Mn concentration for $GaFe_{1-x}Mn_xO_3$ (x = 0.05 and 0.1) and $Ga_{1-x}Mn_xFeO_3$ (x = 0.05 and 0.1).

1.4.4. Magnetic and Electrical properties of $Al_{1-x-y}Ga_xFe_{1+y}O_3$ compounds

In an attempt to increase the T_N of these compounds, we were interested in increasing the Fe content. There has been a very old report by Schieber *et.al.*,[52] which states that $Al_{1-x}Fe_xO_3$ is stable in the orthorhombic phase for $0.6 < x < 1.0$ and $Ga_{1-x}Fe_xO_3$ in the range $0.8 < x < 1.2$. We were successful in getting only two compounds of the formula $Al_{1-x-y}Ga_xFe_{1+y}O_3$ with x = 0.2, y = 0.2 and x = 0.6, y = 0.2.

X-ray diffraction patterns of $Al_{0.6}Ga_{0.2}Fe_{1.2}O_3$ and $Al_{0.2}Ga_{0.6}Fe_{1.2}O_3$ could be indexed to orthorhombic *Pna*2_1 space group. Fig.1.4.26 shows the x-ray diffraction pattern along with the profile fits.
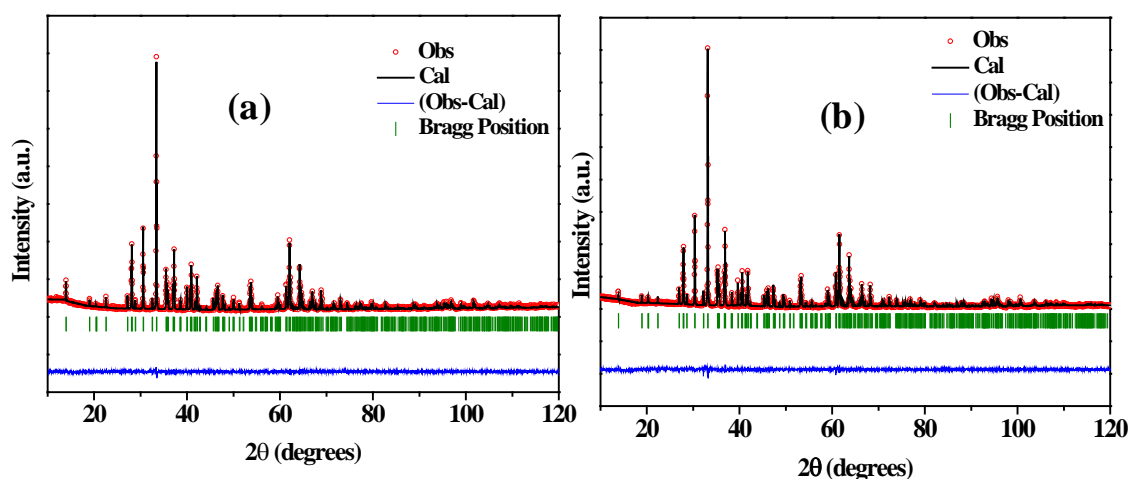
Fig.1.4.26: XRD pattern along with the profile matching for a) $Al_{0.6}Ga_{0.2}Fe_{1.2}O_3$ and b) $Al_{0.2}Ga_{0.6}Fe_{1.2}O_3$.

Lattice parameters of $Al_{0.6}Ga_{0.2}Fe_{1.2}O_3$ was found to be a = 5.0299 (1), b = 8.6425 (1), c = 9.3219 (1) and $\alpha = \beta = \gamma = 90°$ and that of $Al_{0.2}Ga_{0.6}Fe_{1.2}O_3$ was

found to be a = 5.0676 (1), b = 8.7201 (1), c = 9.3825 (1) and α = β = γ = 90°.Unit

cell volume computed from this gives a value of 405.231 $Å^3$ for $Al_{0.6}Ga_{0.2}Fe_{1.2}O_3$ and

414.612 $Å^3$ for $Al_{0.2}Ga_{0.6}Fe_{1.2}O_3$. It can be seen that with the introduction of higher

concentration of Ga^{3+} unit cell volume increases.

Magnetic studies were carried out on these samples and as expected ferrimagnetic transition temperature had increased to a value above room temperature.
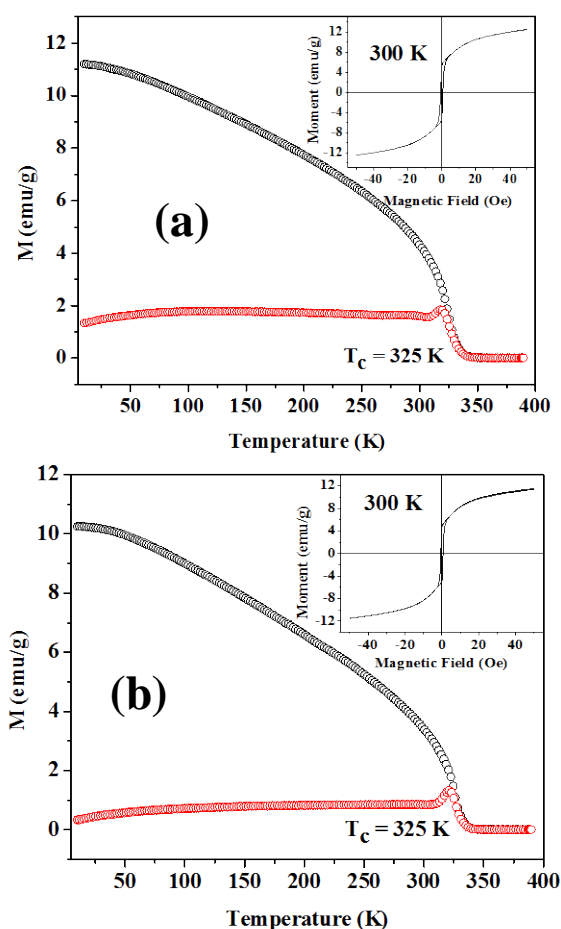
Fig.1.4.27: Variation of magnetization (M) data as a function of temperature for (a) $Al_{0.6}Ga_{0.2}Fe_{1.2}O_3$ and (b) $Al_{0.2}Ga_{0.6}Fe_{1.2}O_3$. Inset shows the M vs H plot at 300 K.

Fig.1.4.27 shows the magnetic data for $Al_{0.6}Ga_{0.2}Fe_{1.2}O_3$ and $Al_{0.2}Ga_{0.6}Fe_{1.2}O_3$. Both these compounds have the same transition temperature of

325 K probably because content of magnetic ion i.e., Fe^{3+} is same in both these compounds.

Magnetic hystereses were measured at room temperature for both these samples. $Al_{0.6}Ga_{0.2}Fe_{1.2}O_3$ has a saturation magnetization of 12.44 emu/g, remanant magnetization of 5.505 emu/g and coercive field of 0.6579 emu/g whereas $Al_{0.2}Ga_{0.6}Fe_{1.2}O_3$ has a saturation magnetization of 11.44 emu/g, remanant magnetization of 4.85 emu/g and coercive field of 0.57 emu/g. Introduction of Ga^{3+} is found to weaken the magnetic interaction which is reflected in the reduction of saturation magnetization and remanant magnetization.

Ferroelectricity in these oxides was explored using pyroelectric measurements. It was found that both these oxides were ferroelectric at low temperatures. $Al_{0.6}Ga_{0.2}Fe_{1.2}O_3$ shows a pyroelectric current maximum at 90 K and $Al_{0.2}Ga_{0.6}Fe_{1.2}O_3$ shows a pyroelectric current maximum at 80 K. Fig.1.4.28 shows the polarization (P) as a function of temperature for $Al_{0.6}Ga_{0.2}Fe_{1.2}O_3$ and $Al_{0.2}Ga_{0.6}Fe_{1.2}O_3$.
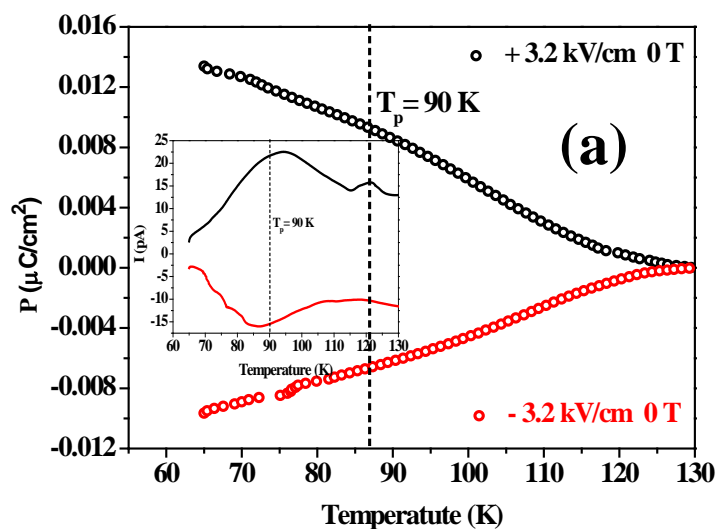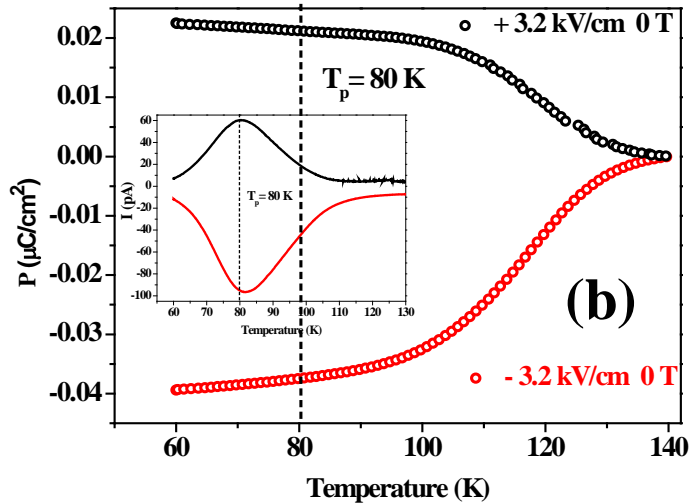
Fig.1.4.28: Variation of electric polarization (P) as a function of temperature at + ve and – ve poling for (a) $Al_{0.6}Ga_{0.2}Fe_{1.2}O_3$ and (b) $Al_{0.2}Ga_{0.6}Fe_{1.2}O_3$.

Magnetic field effect on polarization was studied on $Al_{0.6}Ga_{0.2}Fe_{1.2}O_3$ when it was positively poled (+ 3.2 kV/cm) (Fig.1.4.29).This shows a tremendous effect of magnetic field on polarization and hence reveals the magnetoelectric nature of this oxide. This reduction in presence of an applied magnetic field reinforces the magnetoelectric effect.
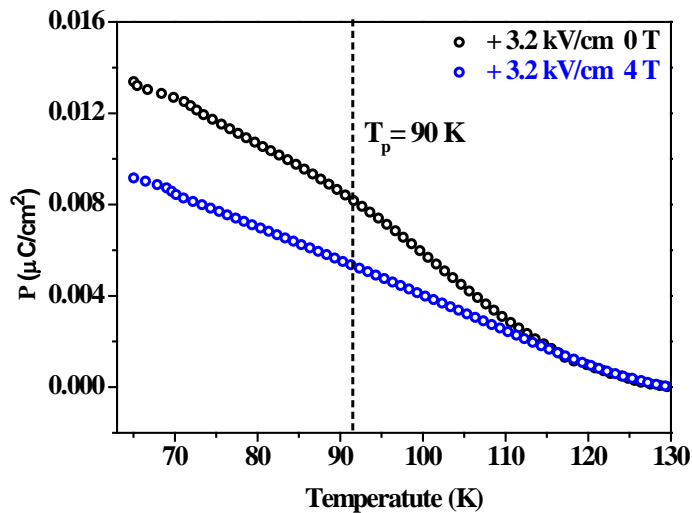
Fig.1.4.29: Variation of electric polarization (P) as a function of temperature at + ve for $Al_{0.6}Ga_{0.2}Fe_{1.2}O_3$ along with the effect of a 4 T magnetic field.

1.4.5. Dielectric and related properties of $Al_{1-x}Ga_xFeO_3$ (x=0.0, 0.5)
1.4.5.1. Ferroelectric Hysteresis measurements

Ferroelectric studies on $AlFeO_3$ and $Al_{0.5}Ga_{0.5}FeO_3$ show hysteresis loop at relatively low temperatures (around 200 K) but these hysteresis loops reflects the leaky nature of these materials. In Fig.1.4.30, hysteresis loop of $Al_{0.5}Ga_{0.5}FeO_3$ is shown. The maximum (saturation) polarization (P_m), remanant polarization (P_R) and coercive field of $Al_{0.5}Ga_{0.5}FeO_3$ are $P_m = 1.135 \ \mu C/cm^2$, $P_R = 0.55 \ \mu C/cm^2$ and $E_c = 3.22 \ kV/cm$ respectively, at 200 K for an applied voltage of 500 V. This value for $Al_{0.5}Ga_{0.5}FeO_3$ is better than the polarization values obtained for both parent compounds $AlFeO_3$ and $GaFeO_3$ [71].
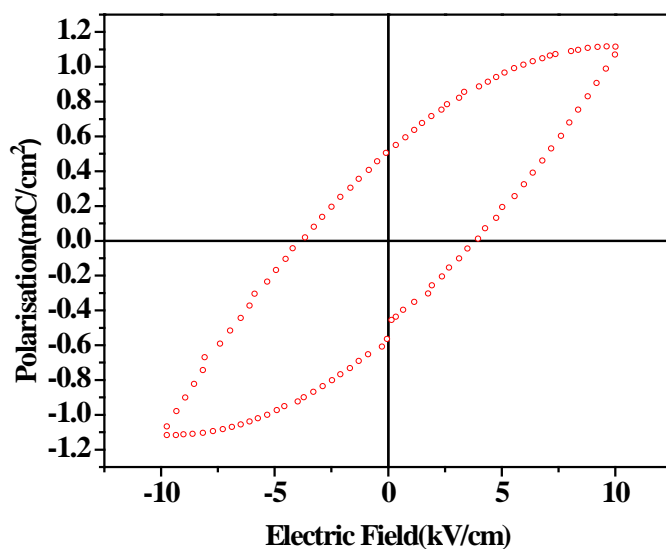
Fig.1.4.30: Ferroelectric hysteresis loop of $Al_{0.5}Ga_{0.5}FeO_3$ measured at 200 K (1 kHz).

1.4.5.2. Dielectric and Magnetodielectric Properties

Dielectric properties of $AlFeO_3$ and $Al_{0.5}Ga_{0.5}FeO_3$ were measured. These compounds showed dielectric dispersion below T_N and a rise in dielectric constant above T_N (Fig.1.4.31). This behavior is quite similar to that exhibited by relaxor

ferroelectrics. Application of magnetic field suppresses the dielectric constant value considerably which indicates that there exists magnetodielectric coupling.
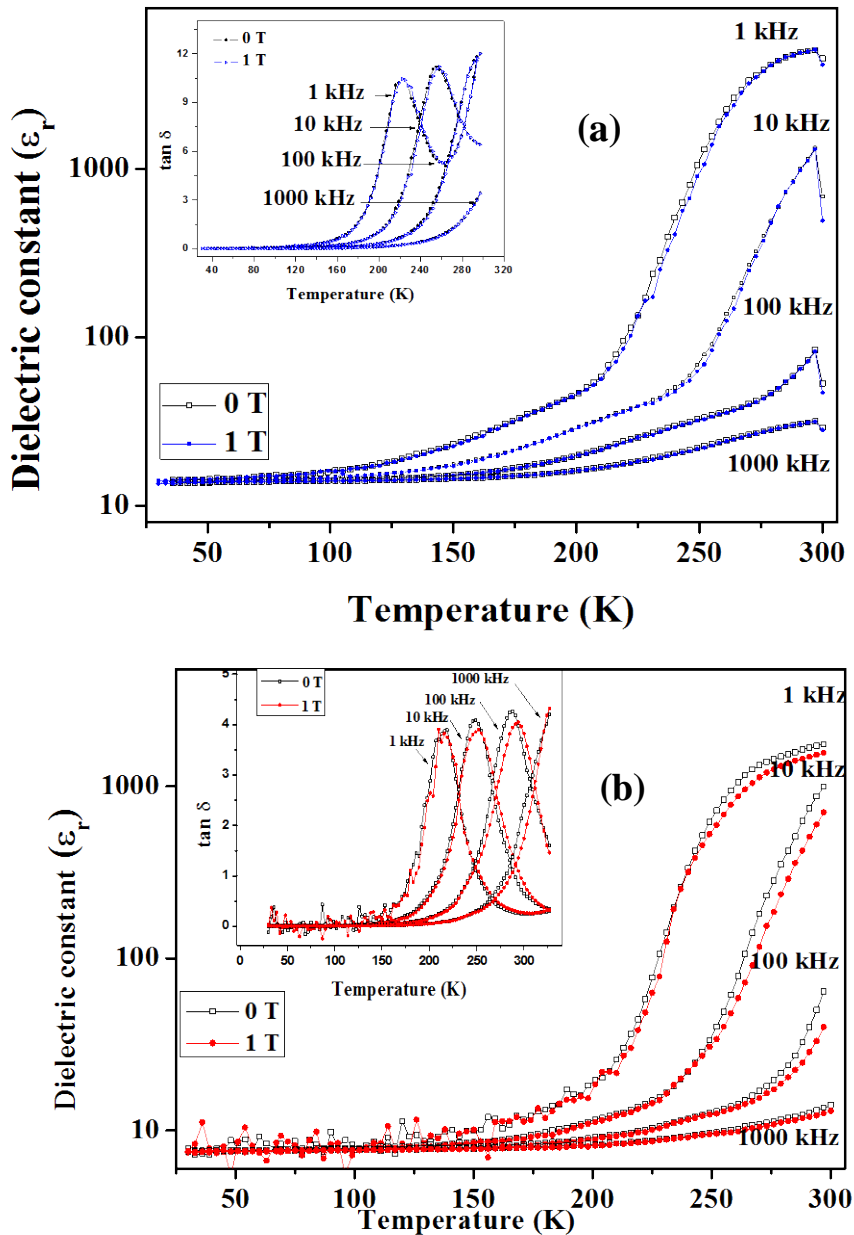
Fig.1.4.31: Variation of dielectric properties of (a) AlFeO$_3$ and (b) Al$_{0.5}$Ga$_{0.5}$FeO$_3$ with temperature is shown. Effect of 1 T is also shown for both (a) and (b).

Magnetodielectric coupling was monitored by measuring capacitance in the presence of an applied magnetic field. This showed significant magnetocapacitive effect. It is seen that these effects are more pronounced in Al$_{0.5}$Ga$_{0.5}$FeO$_3$ than in AlFeO$_3$. Magnetocapacitive effects of Al$_{0.5}$Ga$_{0.5}$FeO$_3$ reaches a value of 60% at room

temperature (Fig.1.4.32). This suggests that the disorder introduced by the introduction of Ga^{3+} can be a key factor which controls the coupling in these compounds. Theoretically it has been shown that spin-phonon coupling manifests more strongly in presence of disorder thereby enhancing the coupling between electric and magnetic order parameters.

Since the magnetodielectric effect can have magnetoresistive contribution, we have measured magnetoresistance as well. Negligible magnetoresistance at room temperature ensures that the magnetodielectric effect observed is not entirely due to magnetoresistive artifacts. Fig.1.4.33 shows the semi-conducting behaviour of resistance exhibited by Al$_{0.5}$Ga$_{0.5}$FeO$_3$ along with the negligible magnetoresistance.
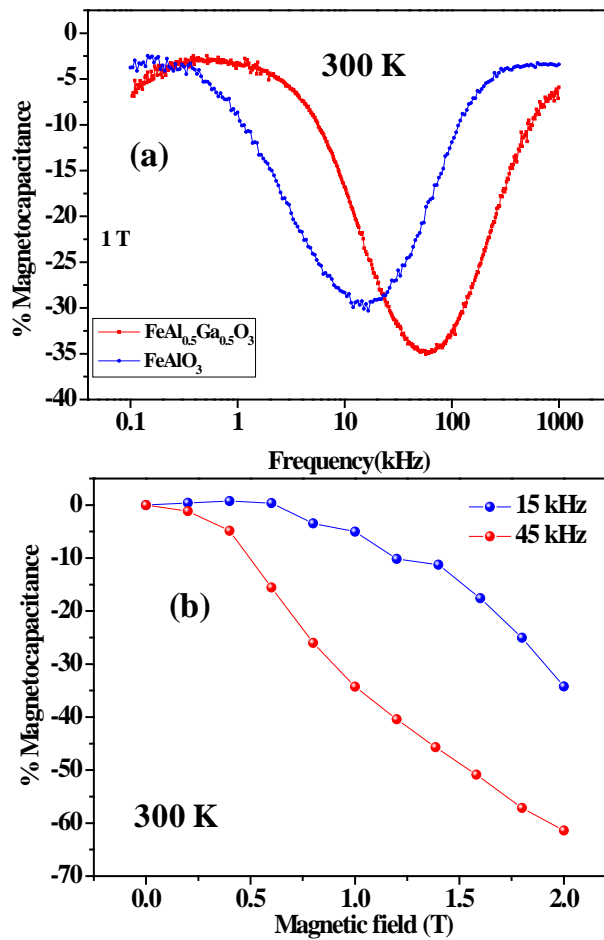
Fig.1.4.32: a): Variation of % magnetocapacitance with frequency for AlFeO$_3$ and Al$_{0.5}$Ga$_{0.5}$FeO$_3$ at a magnetic field of 1 T. (b): Variation of % Magnetocapacitance with magnetic field for AlFeO$_3$ (15 kHz, 300 K), and Al$_{0.5}$Ga$_{0.5}$FeO$_3$ (45 kHz, 300 K).
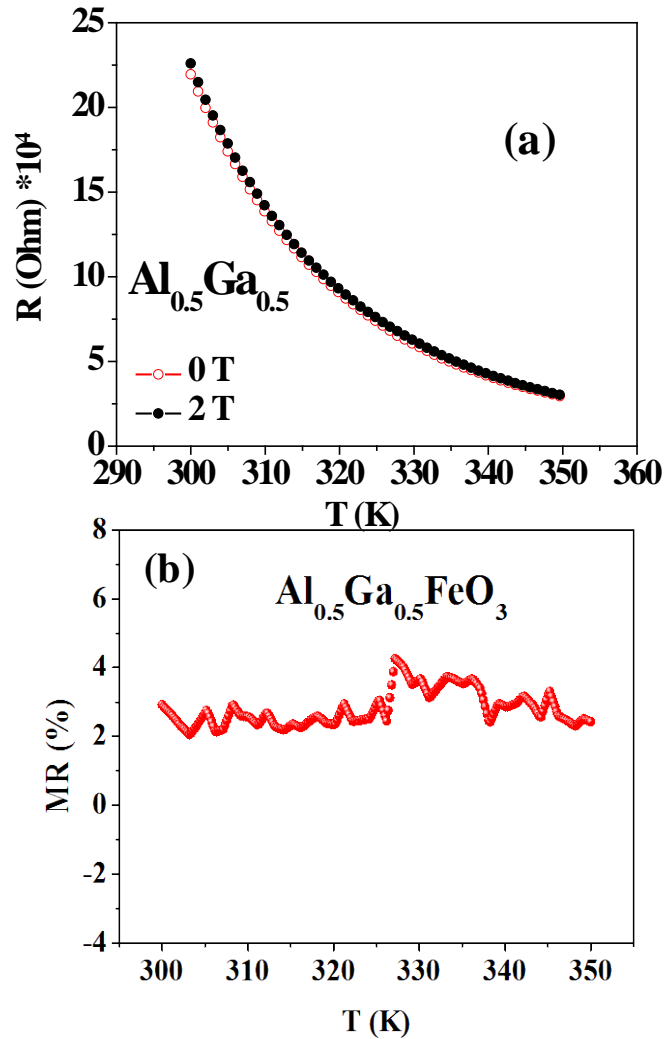
Fig.1.4.33.: (a) DC resistance is plotted against temperature for $Al_{0.5}Ga_{0.5}FeO_3$ at 0T and 2T. (b) % magnetoresistance of $Al_{0.5}Ga_{0.5}FeO_3$ as function of temperature is shown.

Waghmare *et.al.*, have theoretically explored the structure and magnetic properties of $AlFeO_3$ system. Their analysis based on the introduction of anti-site disorder between Fe2 and A2 site reveals that AFM ordering is the stable magnetic ground state (Table.1.4.7.). Fe^{3+} moment varies depending on the site and hence the material as experimentally observed is *ferrimagnetic* in nature.

Table 1.4.7: Energetics of magnetic configuration in $AlFeO_3$

order/ disorder	Total energy of magnetic configuration (eV)		
	$AlFeO_3$-FM	$AlFeO_3$-AFM	$GaFeO_3$-AFM
ordered	-297.02	-300.67	-270.75
disordered	-298.59	-300.09	-270.64

Fe^{3+} ion with an [Ar] $3d^5$ electronic configuration and an octahedral crystal field will have the d state split into t_{2g} and e_g states. For d^5 configuration, superexchange interaction via O is strongly anti-ferromagnetic, when Fe−O−Fe bond angles are close to 180^0. Ideally, such electronic structure should have given a magnetic moment of $5\mu_B$ per Fe ion, corresponding to the high-spin state. From simulation, in accordance with the neutron data, the observed moment value is about $4\ \mu_B$ per Fe ion (Fig.1.4.34). This is due to a strong hybridization between the d−states of Fe and the p−states of O.
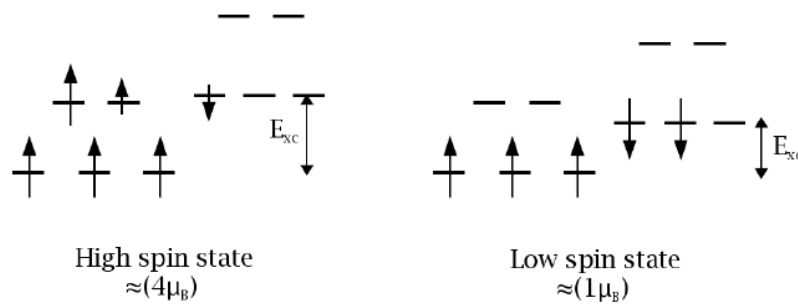
Fig.1.4.34: (a) High-spin and (b) low-spin states of Fe^{3+} ion is shown

Interestingly, it has been seen that bond lengths changes considerably with change in magnetic ordering. This signals to the presence of spin phonon coupling in these systems.

Since Al$_2$O$_3$ and Fe$_2$O$_3$ crystallize in the corundum phase the energetics of AlFeO$_3$ in perovskite and corundum structures (Fig.1.4.35) were compared. The energy of the cubic perovskite structure is 3 eV higher than the observed one. Hence AlFeO$_3$ in the corundum structure is higher in energy by about 84 meV/formula unit. Thus, the stability of the observed structure is attributable to the distinct sites available for Al and Fe.

Table 1.4.8.: Fe-O and Al-O bond lengths (Å)

state	Chemically ordered		Chemically disordered	
	L(Fe-O)	L(Al-O)	L(Fe-O)	L(Al-O)
FM	1.87	1.90	1.85	1.86
	1.87	1.92	1.93	1.87
	1.97	1.93	1.95	1.91
	2.04	1.96	1.97	1.95
	2.06	1.96	1.97	2.02
	2.11	2.02	1.99	2.05
AFM	1.83	1.88	1.90	1.85
	1.89	1.90	2.02	1.86
	1.99	1.92	2.02	1.90
	2.10	1.94	2.03	1.95
	2.18	1.95	2.05	2.05
	2.24	1.97	2.09	2.07
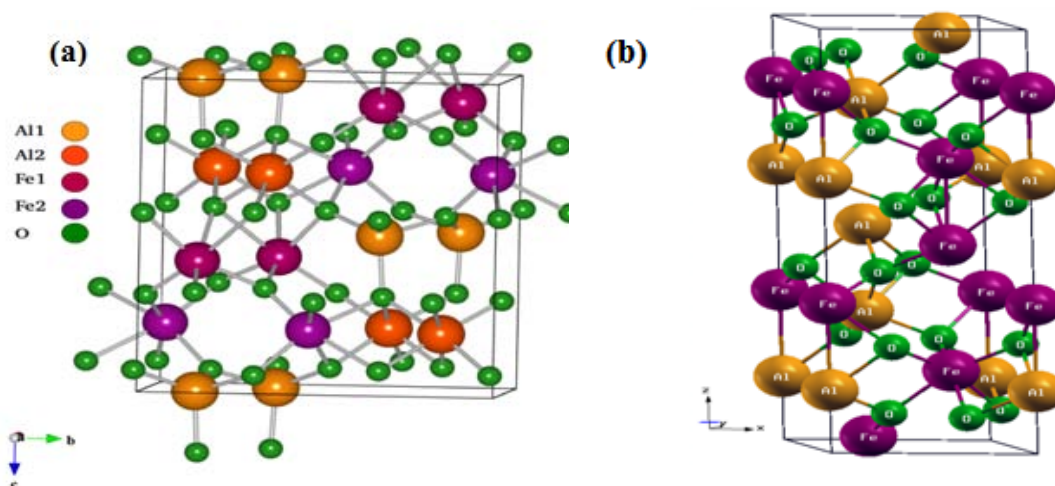
Fig.1.4.35: Structure of $AlFeO_3$ in (a) orthorhombic and (b) corundum structures

Disorder in $AlFeO_3$ is mainly due to mixed occupancy of cations arises from the size mismatch between Fe^{3+} and Al^{3+}. This increases as Ga^{3+} ion is introduced because the size of Ga^{3+} (0.62 Å) is comparable to Fe^{3+} (0.645 Å). Thus as observed experimentally magnetodielectric effects becomes more pronounced in $Al_{0.5}Ga_{0.5}FeO_3$ compared to $AlFeO_3$.

1.4.5.3. Pyroelectric measurements

In the scenario where ferroelectric hysteresis measurements are not satisfactory due to the leaky nature, to confirm the multiferroic nature of $AlFeO_3$ and $Al_{0.5}Ga_{0.5}FeO_3$, ferroelectricity in these oxides has to be established beyond doubt. Pyroelectric measurements are quite promising in this regard as switchable pyroelectric effect, if established, can be taken as a proof for ferroelectricity in these compounds. With this in view pyroelectric measurements were done on these compounds and the results established that these are indeed ferroelectric at very low temperatures (around 100 K) (Fig.1.4.36). This also shows the effect of an applied magnetic field of 4T on these compounds. Magnetic field seems to have a

pronounced effect on polarization thereby re-establishing magnetoelectric effect in these oxides.
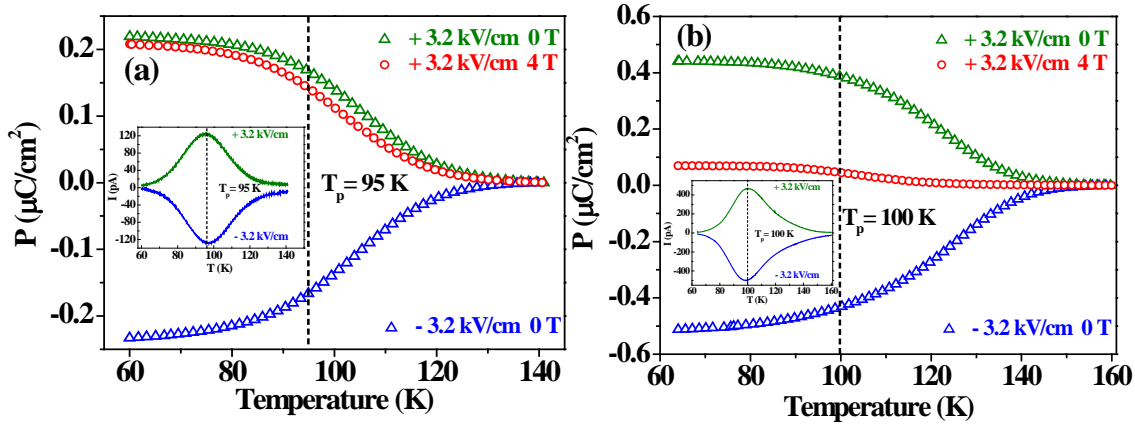
Fig.1.4.36: Variation of electric polarization (P) as a function of temperature at + ve and – ve poling for (a) $AlFeO_3$ and (b) $Al_{0.5}Ga_{0.5}FeO_3$ along with the effect of a 4 T magnetic field.

Origin of ferroelectricity in these compounds is also investigated theoretically taking $GaFeO_3$ (isomorphous with $AlFeO_3$) as a model system. From the symmetry considerations it can be argued that the compound crystallizing in the *Pna*2_1 space group without any site disorder can have a broken inversion centre along z-axis and a planar inversion in the 'xy' plane. Thus these compounds are likely to have a non-zero polarization along the z-direction whereas zero polarization along x and y directions. But polarization along the z-direction lacks switchability.

Experimentally it has been found that anti-site disorder is present in these compounds. In presence of this anti-site disorder and magnetic frustration, inversion symmetry in 'xy' plane is broken and hence the compounds are permitted to have non-zero polarization along x- and y- directions. Spin-phonon coupling adds to this non-zero P_x and P_y values by locally changing the structure. Thus, magnetostrictive effects are also significant in this family of oxides.

Thus, there are three possible contributing factors to the net polarization observed in a polycrystalline sample. Among these P_x and P_y are switchable whereas

P$_z$ remains unswitchable. Hence slight asymmetries in the positively and negatively poled polarization values are expected.

1.4.6. Raman studies

Raman studies were done on AlFeO$_3$ by Sood *et.al.*, AlFeO$_3$ has 40 atoms in the unit cell and 120 normal modes. Of this 117 are Raman modes and 3 are acoustic modes. In Fig.1.4.37 Raman spectra recorded at 5 K is shown revealing 18 modes in the spectral range 100 - 2200 cm^{-1}. An analysis of mode frequencies of the first order modes occurring below 810 cm^{-1} revealed that most of these modes show changes in the vicinity of magnetic transition (~250 K) (Fig.1.4.38). These changes are attributed to the strong spin-phonon coupling operative in the magnetic phase (below T$_N$).
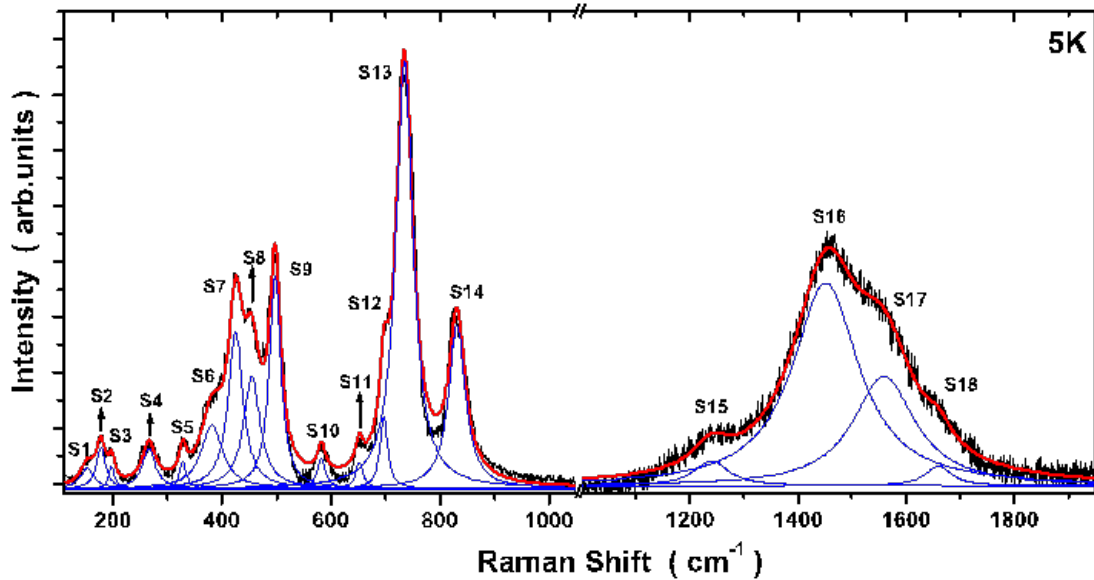
Fig.1.4.37: Raman spectra of AlFeO$_3$ recorded at 5 K.
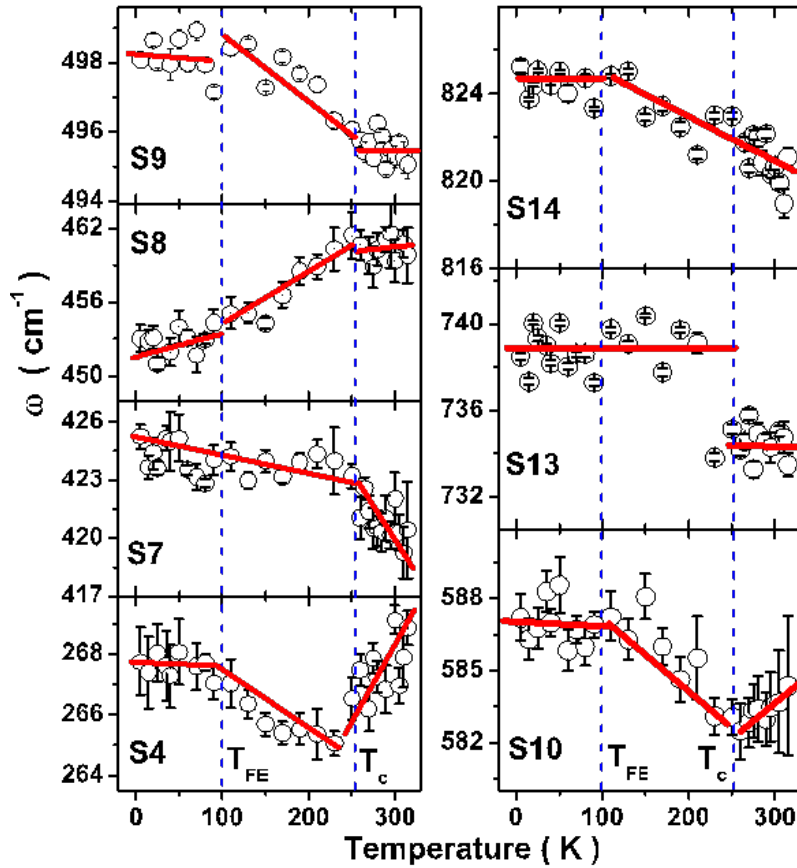
Fig.1.4.38: Temperature dependence of the first-order phonon mode frequencies.

Analysis of second order modes revealed that one of the modes, namely S15, looses intensity above T_N and hence is believed to be associated with two magnon Raman scattering. Nearest neighbour exchange coupling was estimated from the energy of this band and was found to be ~ 5.3 meV which is comparable to the theoretical estimate of 6 meV. Thus, these studies along with the theoretical calculations, uncover very interesting spin-phonon coupling present in the system.

1.5. Conclusions

In conclusion, $AlFeO_3$ and $Al_{0.5}Ga_{0.5}FeO_3$ crystallizes in an orthorhombic structure with $Pna2_1$ space group. The structure as determined from neutron diffraction experiments reveals the presence of four different cation sites namely Fe1, Fe2, A1 and A2.These cation sites shows anti-site disorder. Due to this unequal occupancy of Fe^{3+} in various sites, these oxides have a collinear ferrimagnetic structure.

Ball milling these oxides resulted in interesting phase transition stabilizing metastable corundum and $P2_12_12_1$ phases. Ball milling reduces activation energy probably by creating defects and thereby making this unusual phase transition possible. $AlFeO_3$ undergoes phase transition via two intermediate phases, namely, $P2_12_12_1$ and $R\text{-}3c$. $Al_{0.5}Ga_{0.5}FeO_3$ on the otherhand has only one intermediate phase, i.e, $R\text{-}3c$. The fact that the phase transition pathways changes as Ga^{3+} ions are introduced shows the importance of nature as well as the concentration of A-site cation

Mn^{3+} ions were introduced specifically in Fe site and A-site of $GaFeO_3$. These show different signatures in magnetism as different interaction pathways are affected depending on the site of doping. As Mn^{3+} ions are introduced in Fe site transition temperature is found to decrease. This is possibly because of thereduction

in the number of Fe-O-Fe linkages. On the other hand, introduction of Mn^{3+} in the Ga site does not show any significant changes. This might be attributed to the non-magnetic nature of Ga ions which are replaced here.

Ferroelectric hysteresis measurements show the possibility of ferroelectricity in these compounds at low temperature but were dominated by contributions from conductivity. Later, pyroelectric measurements confirmed ferroelectricity in these compounds around 100 K. Thus, multiferroic nature of $Al_{1-x}Ga_xFeO_3$ family of oxides was established experimentally and theoretically. Dielectric properties show dispersion below T_N and a rise in dielectric constant above T_N. Magnetic field is found to have remarkable effect on the dielectric properties making the sample magnetodielectric multiferroic. This effect increases on the introduction of Ga^{3+}. It reaches a value of 60% at room temperature for $Al_{0.5}Ga_{0.5}FeO_3$. Cation disorder and spin phonon coupling is predicted to be responsible for this magnetodielectric effect. Magnetodielectrics need not necessarily be magnetoelectric. To probe into this, we had applied magnetic field during pyroelectric measurements. This had shown that polarization gets suppressed when measured in presence of magnetic field. Thus, this family of oxides are not only magnetodielectric but also magnetoelectric in nature.

This oxide system is a new addition to the family of multiferroics wherein both magnetism and ferroelectricity arises from the anti-site disorder. This family of oxides is quite interesting because unlike in other ferrites with non-collinear magnetic structures this has been a collinear magnetic system interacting with electric order parameters. This opens up a new direction for designing multiferroic materials.

References

(1) Schmid, H. *Ferroelectrics* **1994**, *162*, 317.

(2) Hill, N. A. *J. Phys. Chem. B* **2000**, *104*, 6694.

(3) Morrish, A. H. *The Physical Principles of Magnetism, Wiley,New York* **1965**.

(4) Spaldin, N. A. *Magnetic materials - fundamentals and applications, Cambridge University Press,New York* **2010**.

(5) Valasek, J. *Phys. Rev.* **1921**, *17*, 475.

(6) Eerenstein, W.; Mathur, N. D.; Scott, J. F. *Nature* **2006**, *442*, 759.

(7) Khomskii, D.I. *J. Magn. Magn. Mater.* **2006**, *306*, 1.

(8) Kimura, T.; Kawamoto, S.; Yamada, I.; Azuma, M.; Takano, M.; Tokura, Y. *Phys. Rev. B* **2003**, *67*, 180401.

(9) Kimura, T.; Goto, T.; Shintani, H.; Ishizaka, K.; Arima, T.; Tokura, Y. *Nature* **2003**, *426*, 55.

(10) Hur, N.; Park, S.; Sharma, P. A.; Ahn, J. S.; Guha, S.; Cheong, S. W. *Nature* **2004**, *429*, 392.

(11) Higashiyama, D.; Miyasaka, S.; Kida, N.; Arima, T.; Tokura, Y. *Phys.Rev. B* **2004**, *70*, 174405.

(12) Ramesh, R. *Nature* **2009**, *461*, 1218.

(13) Teague, J. R.; Gerson, R.; James, W. J. *Solid State Commun.* **1970**, *8*, 1073.

(14) Wang, J.; Neaton, J. B.; Zheng, H.; Nagarajan, V.; Ogale, S. B.; Liu, B.; Viehland, D.; Vaithyanathan, V.; Schlom, D. G.; Waghmare, U. V.; Spaldin, N. A.; Rabe, K. M.; Wuttig, M.; Ramesh, R. *Science* **2003**, *299*, 1719.

(15) Sosnowska, I.; Neumaier, T. P.; Steichele, E. *J. Phys. C: Solid State Phys* **1982**, *15*, 4835.

(16) Seshadri, R.; Hill, N. A. *Chem. Mat.* **2001**, *13*, 2892.

(17) Moreira dos Santos, A.; Parashar, S.; Raju, A. R.; Zhao, Y. S.; Cheetham, A. K.; Rao, C. N. R. *Solid State Commun.* **2002**, *122*, 49.

(18) Belik, A. A.; Iikubo, S.; Kodama, K.; Igawa, N.; Shamoto, S.; Takayama-Muromachi, E. *Chem. Mat.* **2008**, *20*, 3765.

(19) Solovyev, I. V.; Pchelkina, Z. V. *New Journal of Physics* **2008**, *10*, 073021.

(20) Hill, N. A.; Battig, P.; Daul, C. *J. Phys. Chem. B* **2002**, *106*, 3383.

(21) Van Aken, B. B.; Palstra, T. T. M.; Filippetti, A.; Spaldin, N. A. *Nat. Mater* **2004**, *3*, 164.

(22) Huang, Z. J.; Cao, Y.; Sun, Y. Y.; Xue, Y. Y.; Chu, C. W. *Phys. Rev. B* **1997**, *56*, 2623.

(23) Lee, S.; Pirogov, A.; Kang, M.; Jang, K.-H.; Yonemura, M.; Kamiyama, T.; Cheong, S. W.; Gozzo, F.; Shin, N.; Kimura, H.; Noda, Y.; Park, J. G. *Nature* **2008**, *451*, 805.

(24) Lorenz, B.; Wang, Y. Q.; Sun, Y. Y.; Chu., C. W. *Phys. Rev. B* **2004**, *70*, 212412.

(25) Lottermoser, T.; Lonkai, T.; Amann, U.; Hohlwein, D.; Ihringer, J.; Fiebig, M. *Nature* **2004**, *430*, 541.

(26) Ren, C.-Y. *Phys. Rev. B* **2009**, *79*, 125113.

(27) Van den Brink, J.; Daniel, I. K. *J.Phys.: Condens. Matter* **2008**, *20*, 434217.

(28) Efremov, D. V.; van den Brink, J.; Khomskii, D. I. *Nat Mater* **2004**, *3*, 853.

(29) Efremov, D. V.; Khomskii, D. I. *Phys. Rev. B.* **2005**, *72*, 012402.

(30) Nandi, S.; Kreyssig, A.; Yan, J. Q.; Vannette, M. D.; Lang, J. C.; Tan, L.; Kim, J. W.; Prozorov, R.; Lograsso, T. A.; McQueeney, R. J.; Goldman, A. I. *Phys. Rev. B* **2008**, *78*, 075118.

(31) Goto, T.; Kimura, T.; Lawes, G.; Ramirez, A. P.; Tokura, Y. *Phys. Rev. Lett.* **2004**, *92*, 257201.

(32) Arima, T. *J. Phys. Soc. Jpn.* **2007**, *76*, 073702.

(33) Khomskii, D. I. *Physics* **2009**, *2*, 20

(34) Kimura, H.; Noda, Y.; Kohn, K. *J. Magn. Magn. Mater.* **2009**, *321*, 854.

(35) Hur, N.; Park, S.; Sharma, P. A.; Guha, S.; Cheong, S. W. *Phys. Rev. Lett.* **2004**, *93*, 107207.

(36) Rontgen, W. C. *Ann. der Phys.* **1888**, *35*, 264.

(37) Wilson, H. A. *Phil. Trans. R. Soc. A* **1905**, *204*, 129.

(38) Curie, P. *J. Phys. (Paris)* **1894**, *3*, 393.

(39) Dzyaloshinskii, I. E. *Zh.Eksp. Teor. Fiz. [Sov. Phys. JETP]* **1959**, *10*, 628.

(40) Astrov, D. N. *Sov. Phys. JETP* **1960**, *11*, 708.

(41) Astrov, D. N. *Sov. Phys. JETP* **1961**, *13*, 729.

(42) Rado, G. T.; Folen, V. J. *Phys. Rev. Lett.* **1961**, *7*, 310.

(43) Folen, V. J.; Rado, G. T.; Stalder, E. W. *Phys. Rev. Lett.* **1961**, *6*, 607.

(44) Woods, V. E.; Austin, A. E. *Int. J. Magn.* **1974**, *5*, 303.

(45) Lawes, G.; Ramirez, A. P.; Varma, C. M.; Subramanian, M. A. *Phys. Rev. Lett.* **2003**, *91*, 257208.

(46) Spaldin, N. A.; Fiebig, M. *Science* **2005**, *309*, 391.

(47) Spaldin, N. A.; Cheong, S.-W.; Ramesh, R. *Phys. Today* **2010**, *63*, 38.

(48) Remeika, J. P. *J. Appl. Phys.* **1960**, *31*, S263.

(49) F. Bouree; J.L. Baudour; E. Elbadraoui; J. Musso; C. Laurent; Rousset, A. *Acta. Crystallogr.* **1996**, *B52*, 217.

(50) Cotica, L. F.; De Medeiros, S. N.; Santos, I. A.; Paesano, A.; Kinast, E. J.; Da Cunha, J. B. M.; Venet, M.; Garcia, D.; Eiras, J. A. *Ferroelectrics* **2006**, *338*, 241.

(51) Cotica, L. F.; Santos, I. A.; Venet, M.; Garcia, D.; Eiras, J. A.; Coelho, A. A. *Solid State Commun.* **2008**, *147*, 123.

(52)   Schieber, M.; Frankel, R. B.; Blum, N. A.; Foner, S. *J. Appl. Phys* **1967**, *38*, 1282.

(53)   Majzlan, J.; Navrotsky, A.; Evans, B. J. *Phys. Chem. Minerals* **2002**, *29*, 515.

(54)   Nagai, T.; Hamane, D.; Devi, P. S.; Miyajima, N.; Yagi, T.; Yamanaka, T.; Fujino, K. *J. Phys. Chem. B* **2005**, *109*, 18226.

(55)   Bakr Mohamed, M.; Fuess, H. *J. Magn. Magn. Mater.* **2011**, *323*, 2090.

(56)   Kim, W.; We, J. H.; Kim, S. J.; Kim, C. S. *J. Appl. Phys.* **2007**, *101*, 09M515.

(57)   We, J. H.; Kim, S.; Kim, C. In *Magnetics Conference, 2006. INTERMAG 2006. IEEE International* 2006, p 990.

(58)   Naik, V. B.; Mahendiran, R. *J. Appl. Phys.* **2009**, *106*, 123910.

(59)   Han, M. J.; Ozaki, T.; Yu, J. *Phys. Rev. B* **2007**, *75*, 060404.

(60)   West, A. R. *Solid State Chemistry and its application, John Wiley & Sons* **2003**.

(61)   Adriaensen, P.; Moors, R. *XIOS Hogeschool Limburg* **2004-2005**.

(62)   http://www.ill.eu/sites/fullprof/.

(63)   J. Rodriguez-Carvajal, F., LLB CEA-CNRS. **2005**.

(64)   Foner.S. *Rev. Sci. Instrum.* **1959**, *30*, 548.

(65)   Cullity, B. D.; Graham, C. D. *Introduction to magnetic materials, A. Wiley & Sons, Inc. publication* **2009**.

(66)   Saha, R.; Shireen, A.; Bera, A. K.; Shirodkar, S. N.; Sundarayya, Y.; Kalarikkal, N.; Yusuf, S. M.; Waghmare, U. V.; Sundaresan, A.; Rao, C. N. R. *J. Solid State Chem.* **2011**, *184*, 494.

(67)   Saha, R.; Shireen, A.; Shirodkar, S. N.; Singh, M. S.; Waghmare, U. V.; Sundaresan, A.; Rao, C. N. R. *Inorg. Chem.* **2011**, *50*, 9527.

(68)   Levin, I.; Brandon, D. *J. Am. Ceram. Soc.* **1998**, *81*, 1995.

(69)   Fargeot, D.; Mercurio, D.; Dauger, A. *Mater. Chem. Phys.* **1990**, *24*, 299.

(70)   Bakr Mohamed, M. *Vom Fachbereich Material und Geowissenschaften der Technischen Universität Darmstadt* **2011**.

(71)   Shireen, A.; Saha, R.; Mandal, P.; Sundaresan, A.; Rao, C. N. R. *J. Mater. Chem.* **2011**, *21*, 57.

Part - 2

Dielectric properties of Narrow Nanotubes of BaTiO$_3$

*Summary**

BaTiO$_3$ is a classic ferroelectric with the ferroelectric phase transition above room temperature. Size effects in ferroelectrics have gained considerable interest in the recent years owing to miniaturization of gadgets. We have synthesized BaTiO$_3$ nanotubes of 3 - 4 nm wall thickness and have explored the magnetic, electric and magnetodielectric properties of these nanotubes. It has been found that these nanotubes are ferromagnetic at room temperature owing to surface defects. Dielectric properties showed two distinct anomalies which have been attributed to chiral and axial ordering as has been understood from MD simulations done in collaboration with Waghmare *et.al.* These BaTiO$_3$ nanotubes also show interesting hysteretic behavior due to spatial fluctuations and considerable magnetodielectric coupling.

2.1. Introduction

2.1.1. Dielectric materials

Dielectrics are insulating materials that can be polarized on the application of an external electric field. This polarization arises from the separation of positive and negatively charged centres in these materials. This charge separation occurring under an applied electric field is called ***dielectric polarization or polarizability***. This calls for a wide band gap in these materials to ensure low carrier density and high injection barrier at the junctions.

Total polarization can be divided into four parts involving different polarizable species. Response of different species occurs at different frequency regimes. At lower frequencies (10 – 10^4 Hz) polarization occurs due to inhomogenously distributed charge carriers. This so called ***Space charge polarization*** occurs at metal/dielectric interfaces, grain boundaries, domain walls etc. This is an extrinsic contribution to polarization and can predominate the behaviour of the dielectric at times. This is the so called ***Maxwell-Wagner polarization*** which plays the role of an important contributer in many of the dielectrics, ferroelectrics and multiferroics. In the frequency range 10^4 -10^8 Hz molecules with reorientable permanent dipole moment starts to respond to an applied electric field. This is hence

called ***Dipolar polarization***. Here electric field tries to orient the dipoles whereas thermal fluctuations try to perturb this orientation. At still higher frequencies (10^8 – 10^{12} Hz) atoms starts to respond to the applied electric field. This polarization known as the ***Ionic polarization*** is induced by lattice vibrations. Lattice vibrations induce relative atomic motions which result in separation between the positive and negative charge centers leading to polarization. At very high frequencies (10^{12} – 10^{16} Hz) electrons respond to electric field causing ***Electronic polarization***. Here the polarization arises because of the displacement of the electronic shell relative to the nucleus and hence is seen in all materials when placed in an electric field (Fig.2.1.1.)[1].
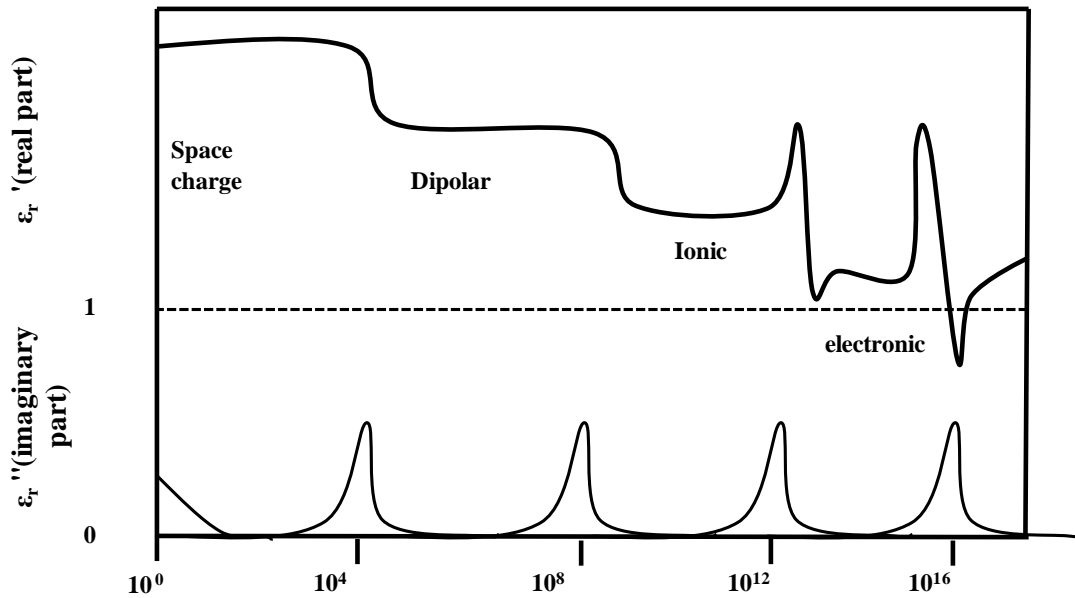
Fig.2.1.1: Frequency dependence of real and imaginary part of dielectric constant[2].

Thus, when a dielectric material is placed in an oscillating electric field, polarizable material inside the dielectric orient itself depending on the frequency of the applied field. Moreover the field forces the polarization to switch the direction, this happens with a certain relaxation time. This complex dielectric permittivity can thus be written as follows:

$$\varepsilon_r = \varepsilon_r^{'} - i\varepsilon_r^{''}$$

Where ε_r' signifies the ability of the dielectric to store charge and ε_r'' the ability to dissipate charge. Dielectric loss is given by

$$\tan \delta = \frac{\varepsilon_r''}{\varepsilon_r'}$$

This can be due to dipole reorientation or due to leakage current. Leakage current contribution is very critical and is seen mainly in lower frequency region. There are as many relaxation times as there are polarizable species as shown in Fig.2.1.1.above. There are two mechanisms for describing the relaxation mechanism, namely Debye relaxation and Maxwell-Wagner relaxation.
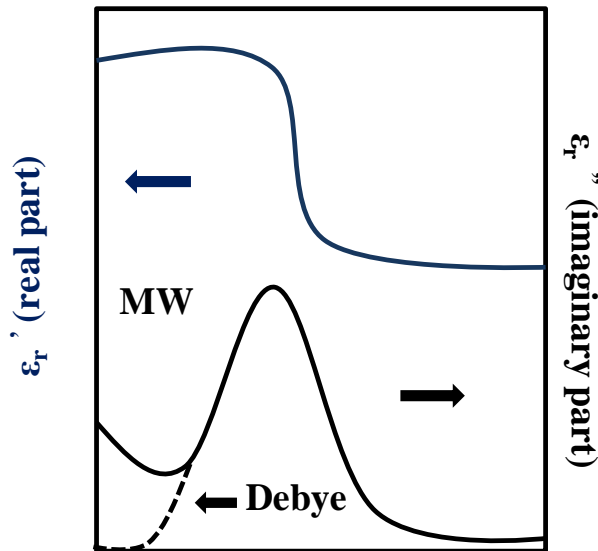
Fig.2.1.2: Frequency dependence of real and imaginary part of dielectric constant depicting Debye relaxation process and Maxwell-Wagner process[2].

Debye relaxation[3] is a simple phenomenon to explain the relaxation when there is only one polarizable entity or identical non-interacting dipoles with same waiting time. When a varying electric field is applied, entities try to follow the field but at higher frequencies they fail to do so and as a result of this a relaxation can be observed. It is given by

$$\varepsilon(\omega) = \varepsilon_\infty + \frac{\varepsilon_s - \varepsilon_\infty}{1 + i\omega\tau}$$

where ε_∞ denotes high frequency permittivity and ε_s denotes low temperature permitivitty (static). τ denotes the relaxation time. Time scale and shape of the relaxation depends on the shape and size of the entity involved in the relaxation process. Smaller molecules relax fast in 10^{-11} s whereas bulkier polar groups relax in $10^{-6} - 10^{-8}$ s.

Maxwell-Wagner relaxation[3] is caused by interfacial polarization in an electrically inhomogenous sample. These charges respond to applied AC field only at low frequencies. This normally occurs due to charge accumulation at the interfaces or at grain boundaries and follows Arrhenius law.

Dielectrics can have sub-classes which are superior in its electrical properties. They can be *piezoelectrics* when they develop spontaneous polarization in response to an applied stress. Other class of materials which develop spontaneous moment when temperature is changed are called *pyroelectrics.* Superior to all these are *ferroelectrics* which has electric dipole moment inherently in the system even in the absence of an external electric field. This polarization is switchable by the application of an external electric field. All ferroelectrics are normally piezo and pyroelectric but reverse is not true always[2].
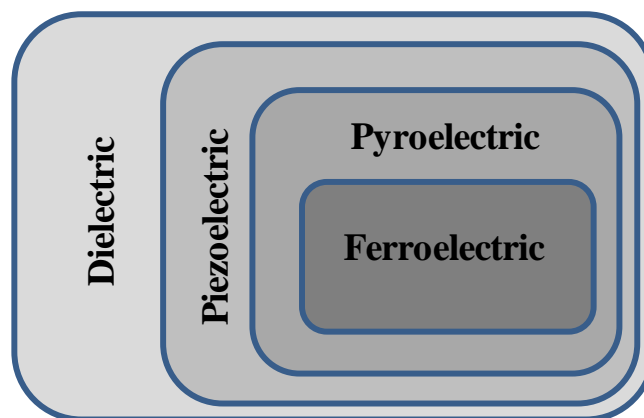
Fig.2.1.3: Schematic representing different classes of dielectric materials[2].

Dielectric properties of BaTiO$_3$ nanotubes

A material turns out to be a ferroelectric only when it does not have a centre of symmetry and when they have more than one polar axis. Due to lack of centre of symmetry in ferroelectrics, centre for positive and negative charges does not coincide in these materials. As the temperature is increased the structure is more likely to become a symmetric one and hence the polarisation disappears above a critical temperature called Curie temperature (T$_c$).This is the so called *ferroelectric phase transition*. Ferroelectrics have high dielectric constants and these phase transitions are also reflected as dielectric anomalies at T$_c$.

$$\boldsymbol{P_i = \chi_{ij}E_j}\text{ , where } \chi \text{ is dielectric susceptibility.}$$

Ferroelectric phase transition has signatures in various other thermodynamic properties like specific heat, elastic modulus, specific heat etc. Ferroelectrics can be classified into two classes – order-disorder type and displacive[1]. In order- disorder type ferroelectrics, permanent dipole moments get randomly oriented above T$_c$. In displacive ferroelectrics, ferroelectricity normally occurs due to off centering of certain ions. These ions move to symmetric positions above T$_c$ resulting in loss of spontaneous polarization. Displacive ferroelectrics are normally perovskites oxides like PbTiO$_3$, BaTiO$_3$, CaTiO$_3$ etc..

Perovskites

Cubic perovskites of the formula ABO$_3$ conventionally have A^{2+} cations sitting at the corners of the cube, B^{4+} ions at the centre of the cube and three O^{2-} ions per unit cell at the faces .Curiously, in violation to the Pauling's rule, in perovskites B^{4+} ions do not touch the neighbouring ions thereby allowing small displacements for this ion. These displacements are quite crucial as they allow polarization and changes in crystal symmetry possible.

(a)   **(b)**

P = 0   **P ≠ 0**
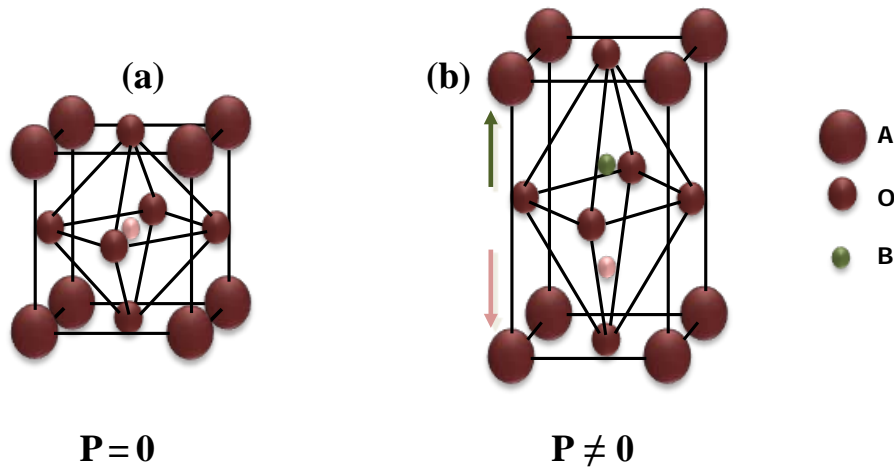
Fig.2.1.4: Crystal structure of BaTiO₃ (a) Paraelectric phase (b) Ferroelectric phase.

A classic example of perovskite ferroelectrics studied widely is $BaTiO_3$ as it has quite high dielectric constant value with very low loss tangent. Moreover, they are environmental friendly compared to their Pb counterpart $PbTiO_3$. In $BaTiO_3$, Ba^{2+} sits at the corners and Ti ions at the centre. Each Ba^{2+} ions are surrounded by 12 oxygen ions and each Ti by 6 oxygen ions. In turn each oxygen ion is surrounded by 4 Ba^{2+} and 2 Ti^{4+} ions. Bulk $BaTiO_3$ is tetragonal at room temperature and is ferroelectric (T_c = 393 K). Beyond this temperature, it undergoes a structural transition to cubic perovskite structure and becomes paraelectric. There are also many low temperature ferroelectric – ferroelectric phase transition in $BaTiO_3$ at 273 K and 183 K with polarization along [110] (orthorhombic) and [111] (rhombohedral), respectively[1].
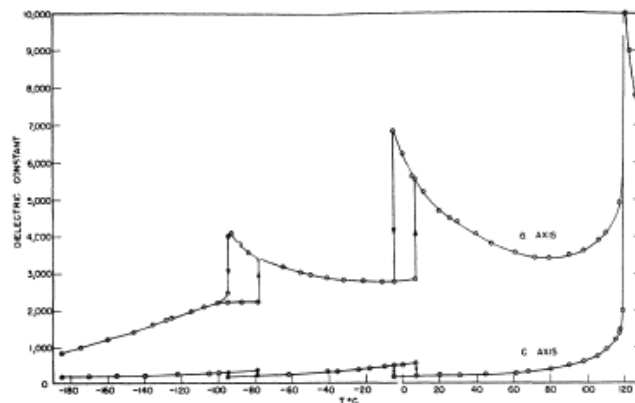
Fig.2.1.5: Dielectric constant of BaTiO₃ measured along different crystallographic constant[4] .

2.1.2. Finite size effects in ferroelectrics

Ferroelectricity in perovskite oxides of the type ABO$_3$ are believed to be associated with a critical size limit, below which ferroelectricity becomes unstable[5]. The reason for this is explained to be the development of *depolarizing field* which opposes ferroelectricity. In perovskite oxides, ferroelectricity arises as a result of movement of B cation towards one direction with respect to the anions. This movement results in accumulation of charges on the surfaces, which in turn causes the cations and anions to move back to the centrosymmetric position. This depolarizing field is screened in bulk ferroelectrics via metal electrodes whereas in nano ferroelectrics beyond a critical size the effective screening becomes difficult and hence ferroelectricity becomes unstable[5]. There are different critical size limits predicted for BaTiO$_3$. Wang et al predicted it to 44 nm[6] whereas Frey et.al. states it to be < 40 nm[7] for BaTiO$_3$ nanoparticles. When it comes to nanowires critical diameter is predicted to be 3.4 nm at room temperature and 1.2 nm at 0 K by Hong et.al.[8] and Genetse et.al[9]. The size effects which contribute to ferroelectricity can be either intrinsic or extrinsic. Extrinsic involves defects, incomplete screening of surface charges etc. Recent studies have shown that rather than an abrupt disappearance of ferroelectricity, there is a gradual decay with particle size.

Spanier et.al. in their paper have shown a new mechanism of stabilizing ferroelectricity in nanowires by means of adsorbing -OH and carboxylate adsorbates. Still their critical sizes are 3 nm (room temperature) and 0.8 nm (low temperature)[10].

Another factor which becomes crucial as the size reduces is surface tension. This surface tension causes internal pressure and hence affects ferroelectricity in 1D nanostructures. The resultant internal pressure is expected to increase the T$_c$ for axial polarisation and decrease for radial polarisation. Incorporating for the effects of
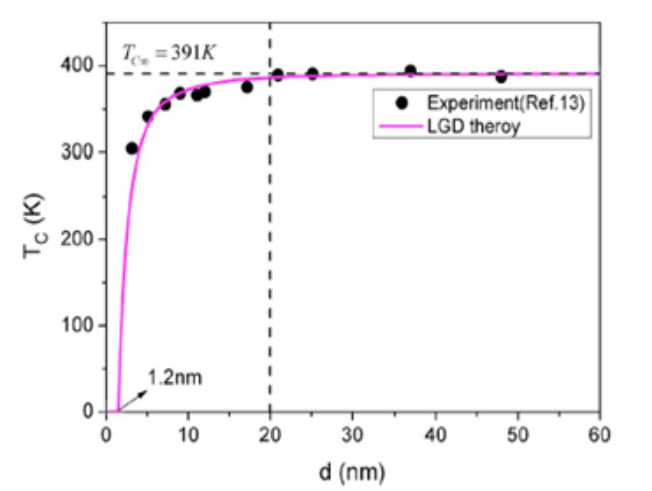
Fig.2.1.6: Decrease in ferroelectric transition temperature with diameter of BaTiO₃ nanowire[8].[reprinted with permission from ref.8]

surface tension, the results of Spanier et.al.[10] have been verified using Ginzburg-Landau Devonshire theory by Hong et. al. for polarization along the radial direction in a nanowire [8](Fig.2.1.6).
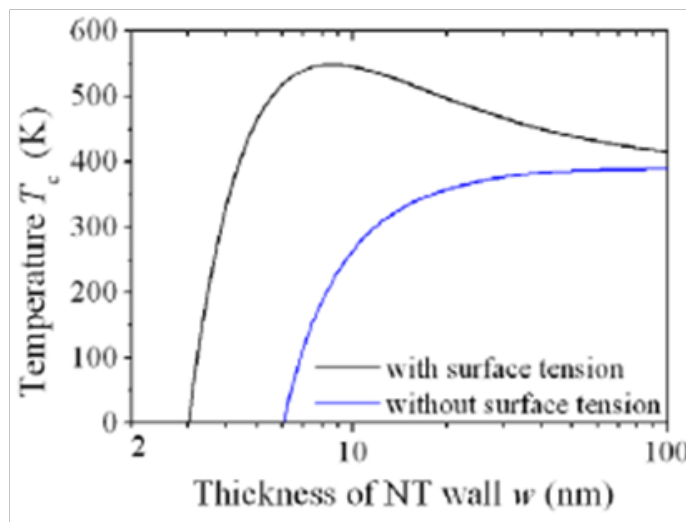
Fig.2.1.7: Ferroelectric phase transition temperature as a function of thickness of nanotubes with and without surface tension effects.[11].[reprinted with permission from ref.11]

Similarly in a nanotube Zheng et.al.[11] shows the effect of surface tension on BaTiO$_3$ nanotubes. The enhancement effect due to surface tension reaches a maximum around 8 nm below which it decreases (Fig.2.1.7). As evident from the graph the critical wall thickness is found to be 3.2 nm at 0 K.

2.1.3. Magnetism in nanoparticles

Magnetic ordering in materials are a result of inter- atomic quantum mechanical exchange interaction between neighbouring moments. These materials are differently classified based on their response to an external magnetic field. Those materials which develop positive and negative magnetization on the application of an external field, and loose it when the field is removed are named *paramagnetic* and *diamagnetic* materials respectively. Whereas, those which develop a field that persists even after the removal of the field are called *ferromagnetic* (positive magnetisation) and *antiferromagnetic* (negative magnetisation) materials. This magnetic interaction is given by Heisenberg's Hamiltonian:

$$H_{ex} = -2 \sum_{i<j} J_{ij} \vec{S_i}.\vec{S_j}$$

where *Si* and *S$_j$* are atomic spins and *J$_{ij}$* is the exchange constant which depends on the inter-nuclear distance. In bulk magnetic materials, the magnetic interaction remains uniform for a finite distance , which is called a domain. These domains in an attempt to minimize magnetostatic energy split up and form smaller domains oriented randomly with a size$\leq$ 100 nm. When an external field is applied it is the rotation of the domain walls which gives rise to finite moment in these materials.

The scenario is slightly different when it comes to nanomaterials. Here, the materials form single-magnetic domain structures[12].The critical size for the formation of single-magnetic domain structures is given by:

$$R_{SMD} = \frac{6\sqrt{AK}}{\mu_0 M_s^2}$$

where A is exchange stiffness, K is magnetic anisotropy, M_s the saturation magnetization and μ_0 permittivity of free space. Nanoparticles respond to external field via spin dynamical processes like spin rotation in contrast to their bulk counterparts which respond through domain-wall movements.

2.1.4. Surface ferromagnetism

Very recently ferromagnetism arose as a universal phenomenon in nanoparticles both magnetic and non-magnetic[13].Several oxides like Al_2O_3, CeO_2[14] , nitrides like GaN[15] and chalcogenides like CdS[15] have been proven to show room temperature ferromagnetism when their particle size is in the range of few hundreds of nanometers. There have been studies on superconductors like $YBCO$[16] and ferroelectrics like $BaTiO_3$[17] which also are in accord with the findings of universal ferromagnetism in nanoparticles. This observed ferromagnetism have been attributed to vacancies and defects which preside on the surface of the nanoparticles[14]. Using first-principles calculation, it has been shown that energy required for the formation of vacancies on the surface is comparatively lesser than that required to form the same kind of vacancies in the bulk[17].The concentration of vacancies on the surface should be sufficient to allow magnetic percolation. These vacancies carry magnetic moments which couple ferromagnetically over short distances[17].

In $BaTiO_3$, it has been shown recently that ferromagnetism and ferroelectricity coexist at room temperature making it a room temperature

multiferroic material[17] (Fig.2.1.8.). It has been shown theoretically that oxygen vacancies present on the surface, can populate the conduction band which has Ti *d*-character with two electrons per oxygen vacancy. These states being quite extended from the surface (> 1nm from the surface) facilitates mediation of magnetic interaction. Ferromagnetic coupling of these spins are found to be always favoured in energy than anti-ferromagnetic coupling [17].
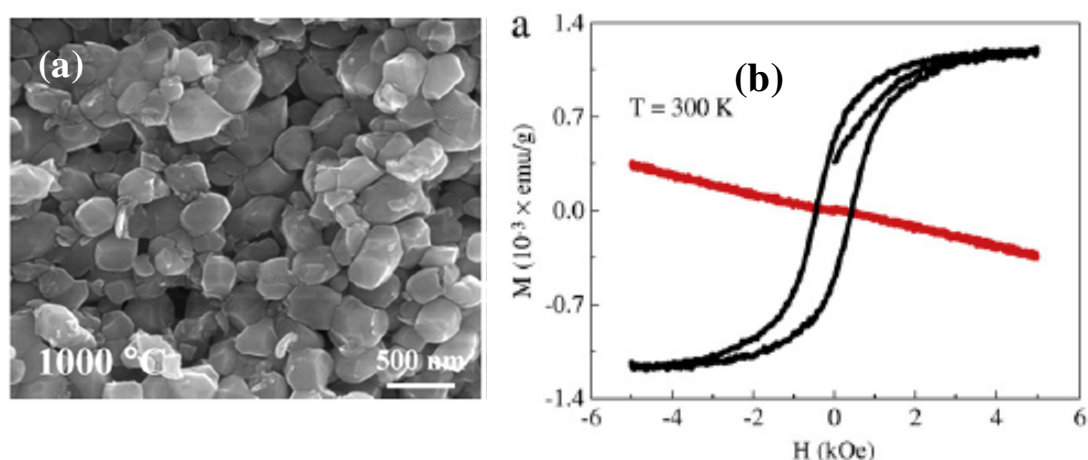
Fig.2.1.8: (a) FESEM image of BaTiO$_3$ nanoparticles heated to 1373 K and (b) room temperature hysteresis establishing ferromagnetic nature[17]. .[reprinted with permission from ref.17]

2.2. Scope of the present investigations

As the size of particles decreases, magnetic and electrical properties vary considerably. Oxide nanoparticles are known to exhibit ferromagnetism at room temperature. Ferroelectrics are also known to show interesting size effects as discussed above. One-dimensional confinement can cause constraints on displacive phase transitions usually feasible in BaTiO$_3$. We were interested in synthesizing nanotubes of BaTiO$_3$ below the theoretically critical size limit so as to study their dielectric behaviour.

2.3. Experimental Section

The procedure of the synthesis of the $BaTiO_3$ nanotubes involves two steps. TiO_2 powder was mixed with 10M NaOH solution under vigorous stirring in the first step[18,19]. This mixture was heated at 453 K for 3 days sealed inside a stainless steel jacketed teflon autoclave. The precipitate so obtained was washed thoroughly with 0.1 M HCl until the pH was neutral and dried at 333 K for 12 h. In the second step, the titanate nanofibres were mixed with $Ba(OH)_2.8H_2O$, taking a slight excess of $Ba(OH)_2.8H_2O$ and was refluxed over an oil bath for 72-80 h[20]. Inert conditions were strictly ensured and the pH of the suspension was maintained between 10-12.The product was washed with hot distilled water, followed by dilute citric acid to remove traces of $BaCO_3$ impurities, if any and was then oven dried.

Powder X-ray Diffraction pattern of the $BaTiO_3$ nanostructures samples were recorded using Bruker-D8 diffractometer. (Cu Kα radiation ($\lambda=1.54 \text{Å}$). Field Emission Scanning Electron Microscopy (FESEM) was done using NOVA NANOSEM 600 (FEI, The Netherlands). TEM images and electron diffraction patterns were recorded on a JEOL JEM-3010 electron microscope (300 kV applied voltage). High resolution images were recorded using a aberration corrected FEI TITAN^{3TM} 80-300 kV transmission electron microscope operated at 300 kV. Dielectric studies were carried out with an Agilent 4294A impedance analyzer in the frequency range 100 Hz to 1 MHz. DC magnetization measurements was done using the vibrating sample magnetometer in the Physical Property Measurement System (PPMS) under zero-field-cooled (ZFC) and field-cooled (FC) conditions in the temperature range of 10 –390 K. Magnetic hysteresis curves were also recorded at 5 K and 300 K.

2.4. Results and Discussion

2.4.1. Structural Determination

BaTiO$_3$ nanotubes gave an X-ray diffraction pattern with broad reflections which could be assigned to the cubic structure with $P\mathrm{m\bar{3}m}$ space group. Profile fitting of this pattern using FULLPROF software gave lattice parameters of a = 4.0406 Å. This shows the phase purity of the sample under investigation.
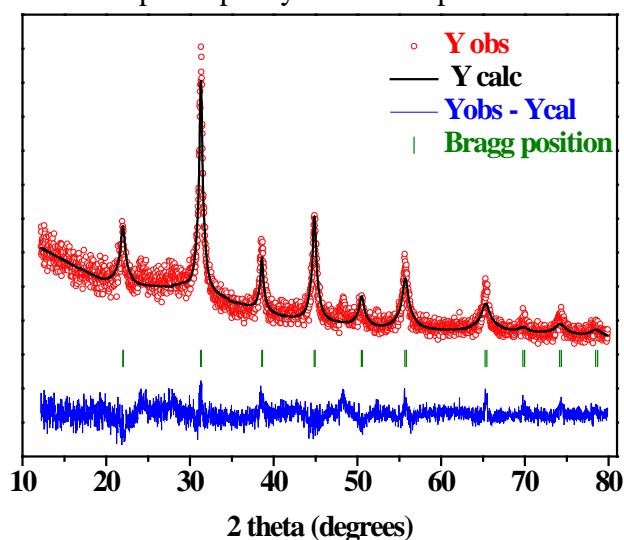
Fig.2.4.1: X-ray diffraction pattern along with profile fitting is given for BaTiO$_3$ nanotube.

2.4.2. Morphology Determination

The as-synthesized BaTiO$_3$ nanotubes where imaged using FESEM and TEM imaging techniques. In Fig.2.4.2b TEM image of the nanotubes is shown. From the image it can be seen that outer diameter of the nanotubes to be around 10 nm and the inner diameter to be around 4 nm to give a wall thickness of 3 nm. Electron diffraction pattern of the nanotubes shows that they are mostly single crystalline. High-resolution TEM image of a nanotube is also shown in Fig.2.4.2c. The image shows the 10-11 lattice fringes in the wall .The *d* spacing is of 0.28 nm that corresponds to the [110] planes [21,22].
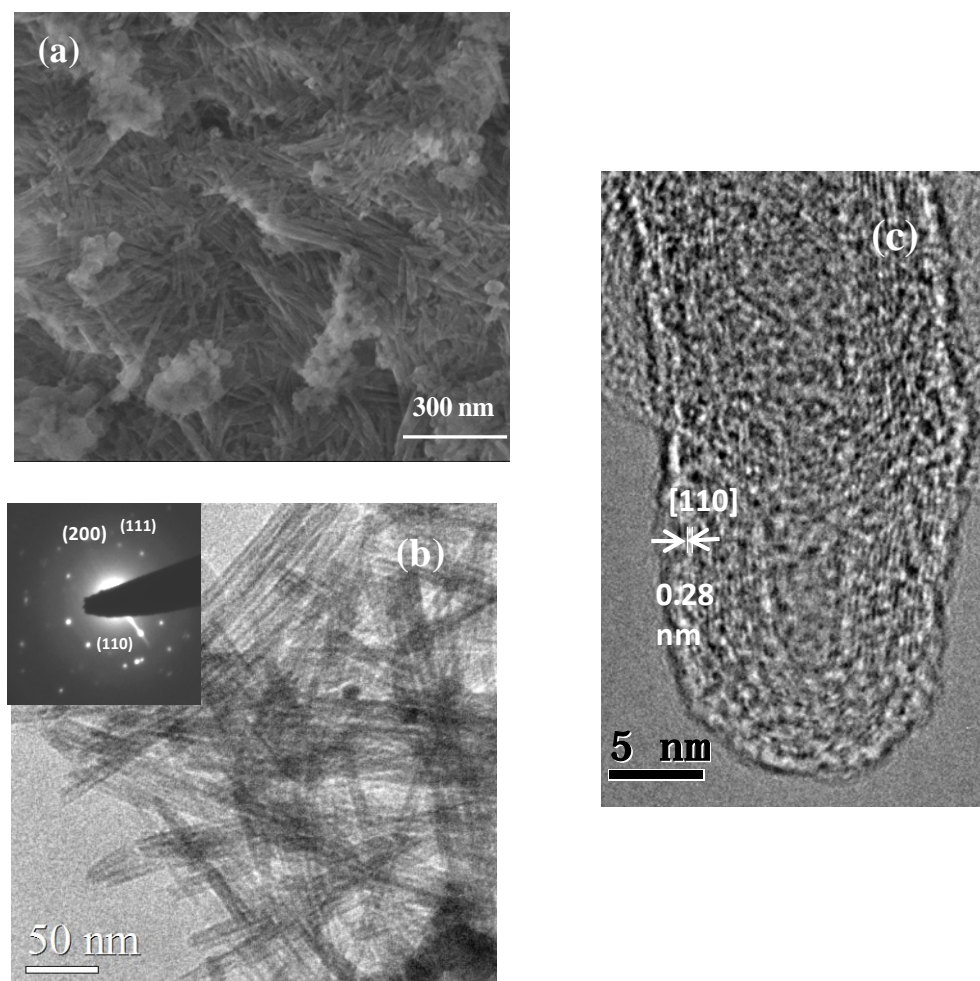
Fig.2.4.2: (a) FESEM image of as-synthesized BaTiO₃ nanotubes. (b) TEM images of BaTiO₃ nanotubes along with ED pattern in the inset. (c) High resolution image of BaTiO₃ nanotubes showing 10-11 lattice planes.

2.4.3. Magnetic Studies

Magnetic measurements were done on these samples under field-cooled and zero-field-cooled conditions. The samples show ferromagnetism at room temperature which can be explained based on the surface ferromagnetism usually exhibited by oxide nanoparticles due to the presence of defects[17]. As the energy required to form defects is less on the surface, they are more prone to have these defects. If the concentration of these defects is adequate enough for magnetic percolation, they tend to interact to give a resultant ferromagnetism in the material. In BaTiO₃

nanoparticles[17], it has been shown that anion vacancies are responsible for the ferromagnetism they exhibit.
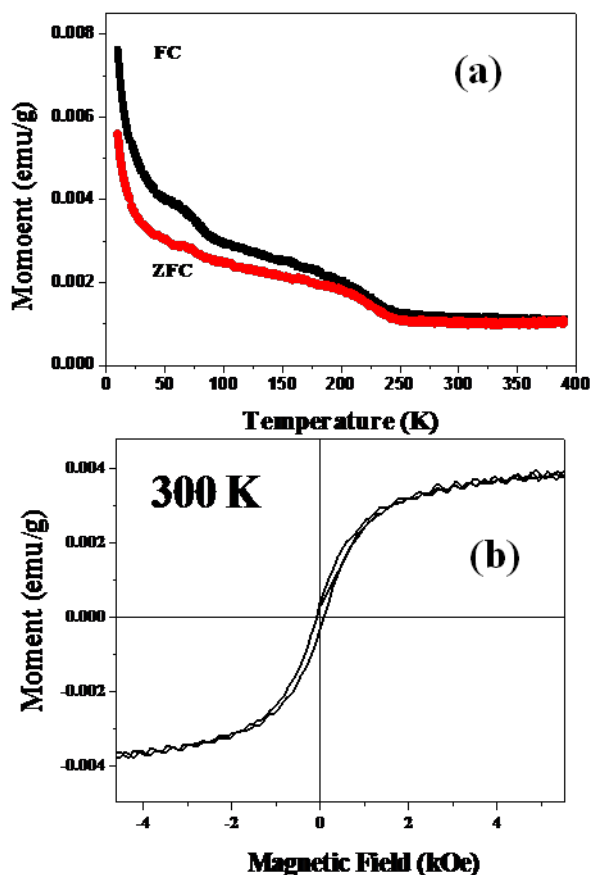
Fig.2.4.3: (a)Magnetization under Field cooled(FC) and Zero-field cooled (ZFC) is plotted as a function of temperature.(b) M-H curve measured at room temperature is shown revealing ferromagnetic character.

2.4.4. Dielectric Studies

Dielectric studies showed that the ferroelectric transition shown by bulk BaTiO₃ is suppressed to a temperature below room temperature. A broad transition appears around 270 K. This is in accordance with the X-ray diffraction pattern which shows the stabilization of cubic phase at room temperature. There was another small hump at 180 K which can be another transition. These dielectric

properties show unusual thermal hysteresis. On cooling the samples, they undergo no transition and approach the low temperature value smoothly. On reheating after allowing the sample to relax back for couple of hours shows the same behaviour observed initially.
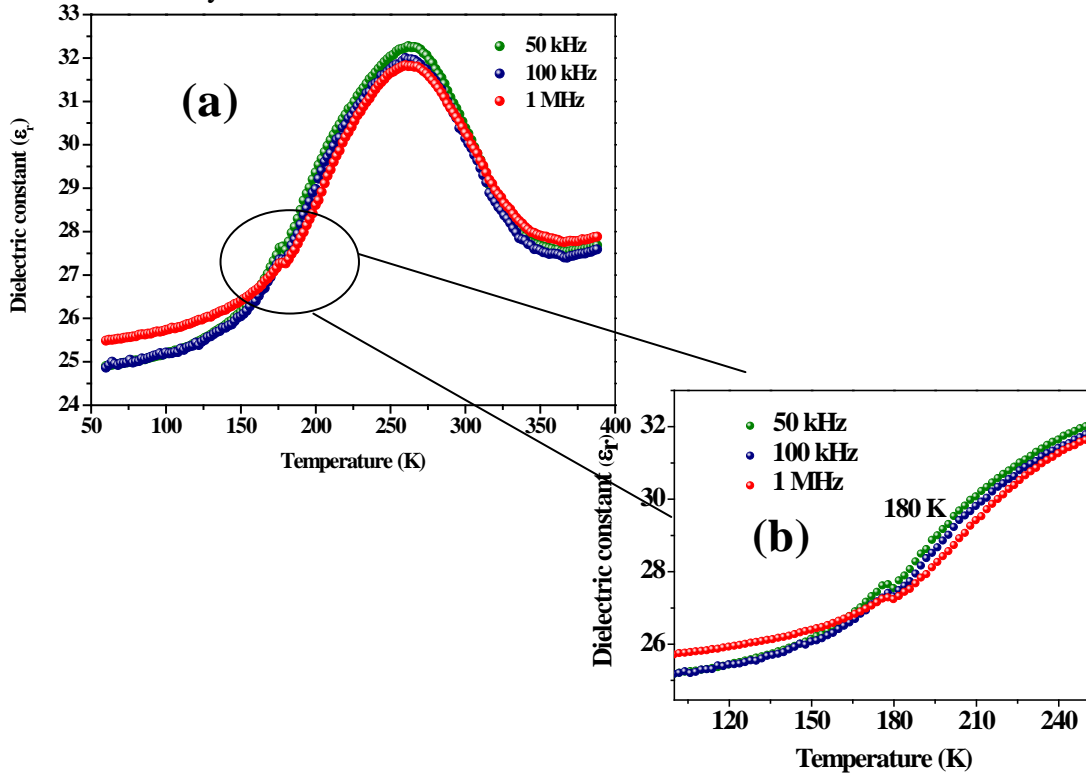
Fig.2.4.4: (a) Dielectric constant is plotted as a function of tempearutre showing two transitions (180 K and 270 K) and (b) enlarged plot of dielectric constant v/s temperature to show 180 K transition.
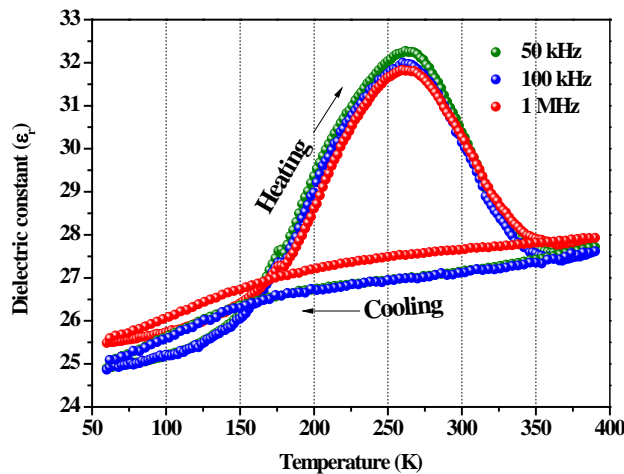
Fig.2.4.5:Dielectric constant is plotted as a function of temperature during heating and cooling cycles.

2.4.5. Magnetoelectric coupling

Magnetic and electric order parameters if simultaneously present are likely to couple. Mangalam et.al. reported a surface phonon mode which is likely to couple with magnetic order parameters. We had therefore studied the effect of a magnetic field of 2 T on BaTiO$_3$ nanotubes and had seen a magnetocapacitance of about 4% at around the transition temperature (270 K). This was almost frequency independent as shown in Fig. 2.4.6.
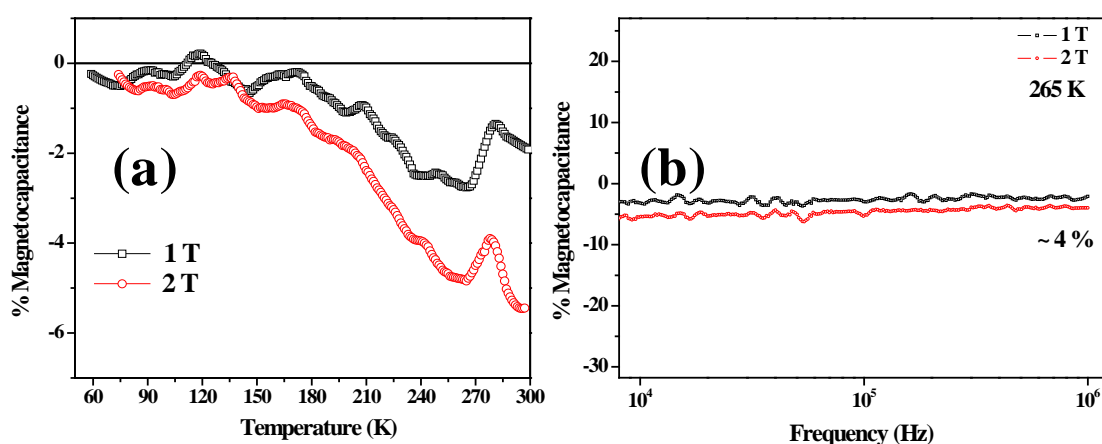
Fig.2.4.6: Magnetocapacitance plotted as a function of (a) temperature and (b) frequency.

2.5. Theoretical understanding

Molecular Dynamic simulation based on first-principles effective Hamiltonian done by Waghmare et.al. could efficiently reproduce the experimentally observed results and had offered an explaination for the unusual dielectric properties observed. From MD simulation, during the heating simulation they get two peaks in the dielectric constant which they relate to the experimentally observed braod peak at 270 K and minor peak at 180 K. Whereas the cooling simulation does not provide any such distinct features.

Dielectric properties of BaTiO₃ nanotubes

Theoretical studies show that in a nanotube there are two polarizations possible (Fig.2.4.7 and Fig.2.4.8) namely axial polarization and chiral polarization. These polarizations melt at two different temperatures giving two peaks in the dielectric plot. Chiral polarization is expected to melt at a lower temperature than axial polarization.
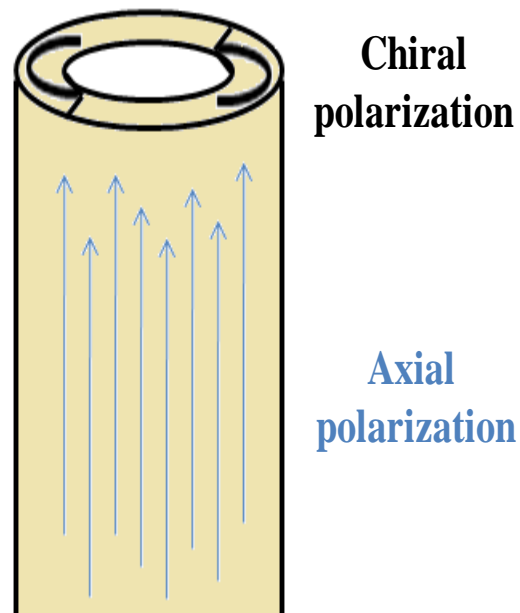
Fig.2.4.7: Two possible polarizations in a nanotube namely chiral and axial polarization.
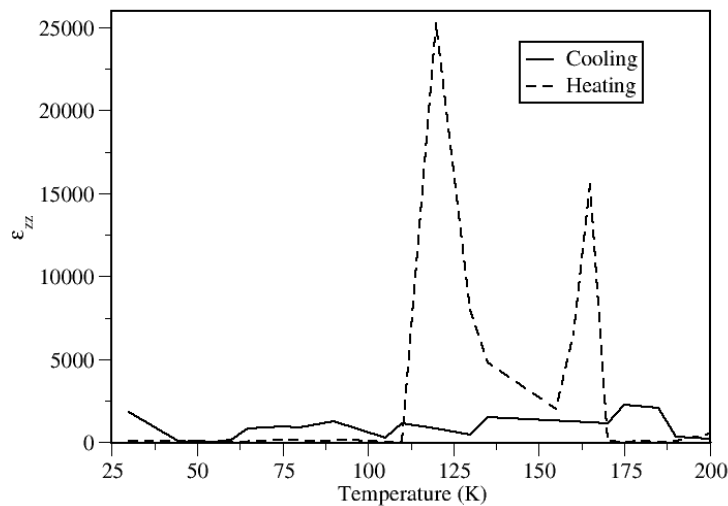
Fig.2.4.7:Dielectric constant plotted as a function of temperature.(results from simulations)

There is a difference in the temperature at which transitions occur in experiment and in theory. This is due to the shorter time span for which simulations

100

are done. MD snapshots showing axial and chiral polarizations were captured at 30 K. (Fig.2.4.8.)
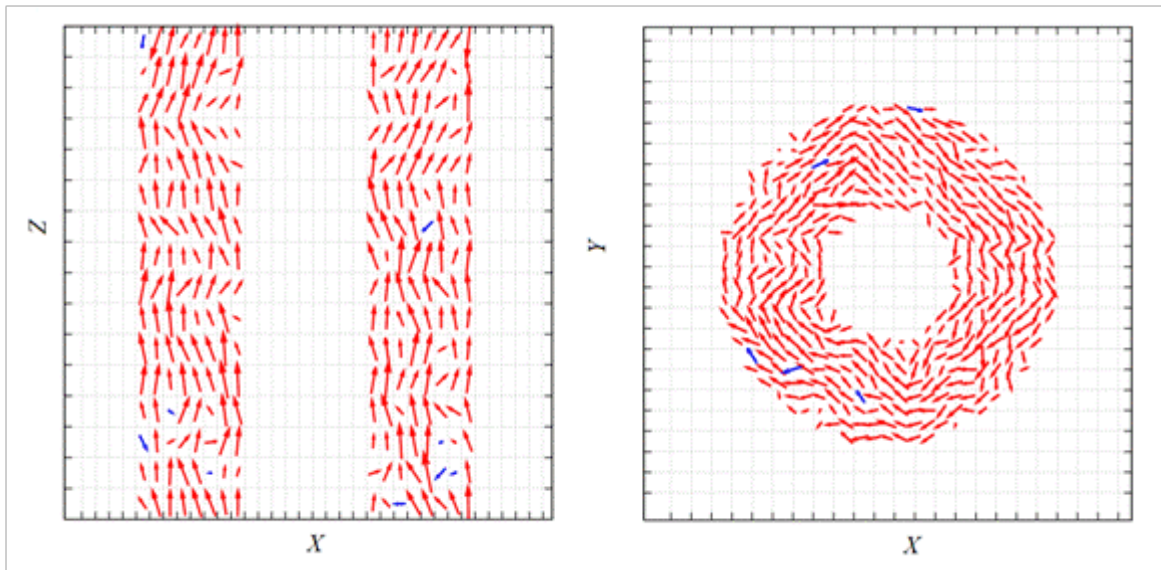
Fig.2.4.8.Polarizations ordering in BaTiO₃ nanotube axially (left) and chirally (right) at 75 K.

Unusual hysteretic behaviour observed experimentally is also reflected in the MD simulations. This is attributed to the spatially inhomogenous ordering occurring at higher temperature during cooling simulation unlike in heating simulation.

2.6. Conclusions

Dielectric and magnetic properties of BaTiO₃ nanotubes have been studied experimentally and theoretically. These nanotubes are ferromagnetic at room temperature but their dielectric order parameters seems to be quite different from their bulk counterpart. They seem to have two dielectric ordering melting at two different temperatures. MD simulations done gives an understanding that these can be attributed to melting of chiral and axial polarizations which are possible in a nanotubular structure. These nanotubes also show coupling between electric and magnetic order parameters.

References

(1) Kittel, C. *Introduction to Solid States Physics* **1956**, *Wiley, New York.*

(2) Arveux, P. E. *University of Bordeaux* **2009**.

(3) Jonsher, A. K. *Dielectric relaxation in solids* **1983**, *Chelsea Dielectrics Press, London.*

(4) Merz, W. J. *Phys. Rev.* **1949**, *76*, 1221-1225.

(5) Spaldin, N. A. *Science* **2004**, *304*, 1606-1607.

(6) Wang, Y. G.; Zhong, W. L.; Zhang, P. L. *Soild State Commun.* **1994**, *90*, 329.

(7) Frey, M. H.; Han, Z. X. P.; Payne, D. A. *Ferroelectrics* **1998**, *337*.

(8) Hong, J.; Fang, D. *Appl. Phys.Lett.* **2008**, *92*, 012906-3.

(9) Geneste, G.; Bousquet, E.; Junquera, J.; Ghosez, P. *Appl. Phys. Lett.* **2006**, *88*, 112906-3.

(10) Spanier, J. E.; Kolpak, A. M.; Urban, J. J.; Grinberg, I.; Ouyang, L.; Yun, W. S.; Rappe, A. M.; Park, H. *Nano Lett.* **2006**, *6*, 735-739.

(11) Zheng, Y.; Woo, C. H.; Wang, B. *J. Phys.: Cond. Matt.* **2008**, *20*, 135216 [doi:10.1088/0953-8984/20/13/135216].

(12) Georgia C, P. *Nano Today* **2009**, *4*, 438-447.

(13) Sundaresan, A.; Rao, C. N. R. *Nano Today* **2009**, *4*, 96-106.

(14) Sundaresan, A.; Bhargavi, R.; Rangarajan, N.; Siddesh, U.; Rao, C. N. R. *Phys. Rev. B* **2006**, *74*, 161306.

(15) Madhu, C.; Sundaresan, A.; Rao, C. N. R. *Phys. Rev. B* **2008**, *77*, 201306.

(16) Shipra; Gomathi, A.; Sundaresan, A.; Rao, C. N. R. *Solid State Commun.* **2007**, *142*, 685-688.

(17) Mangalam, R. V. K.; Ray, N.; Waghmare, U. V.; Sundaresan, A.; Rao, C. N. R. *Solid State Commun.* **2009**, *149*, 1-5.

(18) Lan, Y.; Gao, X.; Zhu, H.; Zheng, Z.; Yan, T.; Wu, F.; Ringer, S. P.; D.Song. *Adv. Mater.* **2005**, *15*, 1310.

(19) Maxim, F.; Vilarinho, P. M.; Ferreira, P.; Reaney, I. M.; Levin, I. *Cryst.Growth Des.* **2011**, *11*, 3358.

(20) Mao, Y.; Banerjee, S.; Wong., S. S. *Chem. Commun.* **2003**, 408.

(21) Yang, Y.; Xiaohui, W.; Changku, S.; Longtu, L. *Nanotechnology* **2009**, *20*, 055709.

(22) Bao, N.; Shen, L.; Srinivasan, G.; Yanagisawa, K.; Gupta, A. *J. Phys. Chem. C* **2008**, *112*, 8634-8642.

Part- III

Studies on Transparent Conducting Oxides

*Summary**

Transparent Conducting oxides are oxides which are conducting and transparent simultaneously. They are used extensively in flat panel displays, etc. Here we have made three compounds namely Ge-doped In_2O_3, Ge-doped Ga_2O_3 and Ge-doped $Ga_{1.4}In_{0.6}O_3$. They have been investigated for their optical and electrical properties. Though all three of these oxides have optical transpareny required for a TCO, only Ge-doped In_2O_3 had conductivity values comparable to that of Tin doped indium oxide, which is a widely used transparent conducting oxide.

3.1. Introduction

Materials which combine metal like electrical conductivity and optical transparency across the visible region, are called ***Transparent Conducting Oxides***. First report of this kind of material dates back to 1907 when CdO film was reported to be both transparent and conducting by Badekar[1]. Important TCO materials are doped ZnO, In_2O_3, SnO_2 and CdO, ternary compounds like Zn_2SnO_4[2], and multi-component oxides consisting of combinations of ZnO, In_2O_3 and SnO_2[3]. Detailed studies on transparency, conductivity and phase relationships have been carried out by various groups on ternary systems of Ga_2O_3-In_2O_3-SnO_2[4,5]; Ga_2O_3-In_2O_3-ZnO[6]; In_2O_3-SnO_2-ZnO[3] and Ga_2O_3-SnO_2-ZnO[7] which have resulted in the discovery of new TCO compounds and solid solutions. However, tin doped indium oxide (ITO) remained superior in terms of conductivity[8,9]. ITO has a conductivity of 1- 5 S cm^{-1} and transparency of 85-90% in thin films[8]. These materials have found interesting applications as transparent electrodes for flat panel displays, photovoltaic cells, low emissivity windows, window defrosters, transparent thin films transistors, light emitting diodes, and semiconductor lasers.

Metals with high density of free electrons can be good electrical conductors but at the same time they are poor transmitters of light in the visible region due to reflection or absorption of light by free electrons. And hence they are less likely to be transparent. On the other hand, insulators with wide band gap transmits almost all

light having energy less than the band gap but they lack conductivity due to the absence of charge carriers . These two properties namely optical transparency and electrical conductivity being mutually exclusive, band structure in these materials have to be unique for them to be simultaneously conducting and transparent.

Electrical conductivity is determined by the position of the bands in the energy diagram, which can be tuned via doping. Optical transparency is determined by fundamental band gap, selection rules like Moss–Burstein effect etc.[10].Moss-Burstein effect increases the apparent band gap of the material by preventing band-to-band transitions. This uniqueness can be seen in oxides of Zn, Cd, Sn, Ga, In etc..[10]

3.1.1. Electrical Properties

Conductivity in transparent conducting oxides can be explained based on the Drude free electron theory. Conductivity due to electrical charges can be given by

$$\sigma = ne\mu$$

where n gives the carrier concentration, e the electronic charge and μ the mobility. Thus, to tune the conductivity in these oxides two parameters that can be changed are carrier concentration and carrier mobility.

3.1.1.1. Carrier concentration

Carriers can be either anion vacancies or dopants. Anion vacancies are generally introduced during reduction and they act as two electrons in the lattice. On the other hand, doping of a higher valence metal into the lattice results in extra charge carriers which can contribute to electrical conductivity. Increase in carrier

concentration can increase conductivity but demands a compromise on the optical transparency and hence is not a solution beyond a threshold[11].

3.1.1.2. Carrier mobility

Carrier mobility (μ) is affected by various defects and disorder in the crystal/film. There are various scattering mechanisms that can affect carrier mobility. They are ***grain boundary scattering***, which occurs due to the interface between different grains present. They can also trap the carriers in them. Another mechanism can be ***ionized impurity scattering***. This is due to the electrostatic field of the charged impurities and hence increases as the number of carriers increases. Yet another mechanism for scattering is ***lattice scattering*** which is due to interaction of the carriers with the lattice vibrations. This scattering increases with increase in temperature. The last scattering mechanism which does not contribute much to reducing carrier mobility is ***electron-electron scattering*** which occurs due to electron-electron collisions. Various scattering mechanism contribute differently to conductivity based on synthesis conditions, temperature of synthesis etc[11].

3.1.2. Optical Properties

Optical properties can be understood if there is knowledge of band structure. Oxides having electronic configuration *(n-1) d^{10} ns^2* like In_2O_3, Ga_2O_3, ZnO, which are common TCOs investigated so far have, similar band structure (Fig.3.1.1). Interaction between O *2p* and M *s* orbital gives the band structure in these oxides. Valence band is made of bonding and non-bonding *2p* orbitals of oxygen whereas conduction band is made of antibonding *Ms-Op* interaction. In_2O_3 and Ga_2O_3 used as parent oxides here, have an indirect band gap of 2.88 eV and 4.86 eV respectively[12].

When undoped, Fermi level generally lies in the middle of the valence and conduction band. But as dopants are introduced, donor levels are created near the conduction band minimum and Fermi level will now lie in between these donor levels and the conduction band minima. Above a critical concentration of these donor atoms, donor states merge with the conduction band of the host. This shifts the Fermi level higher up and hence widens the band gap. This is called *Moss-Burstein shift*[13,14].

3.1.2. 1. Moss-Burstein effect
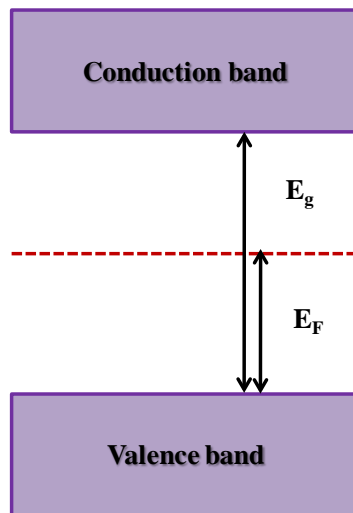
Fig. 3.1.2.: Schematic representation for band structure.

Band Gap is defined by the energy separation between top of the valence band and unoccupied levels in conduction band. In semiconductors with heavy n-doping, Fermi level lies in the conduction band and hence Pauli exclusion principle forbids transition into occupied state thereby blue shifting the absorption band edge into higher energy[13,14].
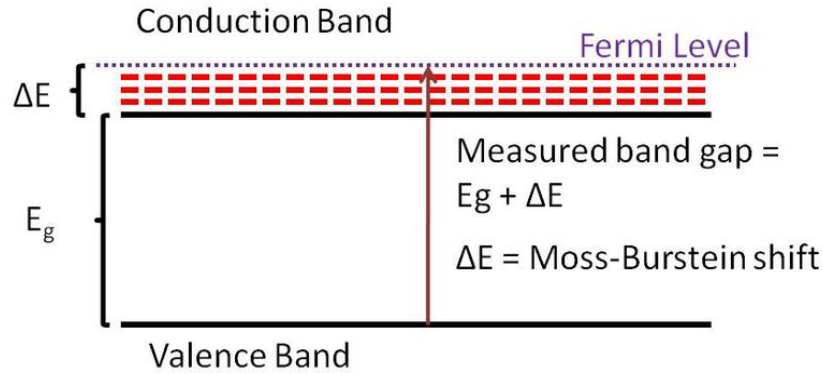
Fig.3.1.3: Schematic representation depicting Moss-Burstein shift.

An ideal TCO should have enough concentration of dopants such that the impurity levels form continuous level (*band*) facilitating electronic conduction without scattering. In such a scenario, Moss-Burstein shift plays a role in keeping the absorption away from the visible range, making the material transparent.

3.1.3. Crystal structure

3.1.3.1. In₂O₃

In$_2$O$_3$ crystallizes in body-centered cubic byxbite structure (space group $Ia\bar{3}$), which is a defective superstructure of fluorite structure. In^{3+} occupies two different crystallographic sites, one which is made of trigonally distorted oxygen atoms and other made of more distorted oxygen octahedral[10].

3.1.3.2. Ga₂O₃

Among the various polymorphs of Ga$_2$O$_3$ the most common one is β-Ga$_2$O$_3$ with monoclinic structure (space group *C2/m*). Here Ga^{3+} is present in two crystallographically non-equivalent sites, one of which is tetrahedrally and another octahedrally co-ordinated. This crystal structure is known to have some distortions from the ideal structure. It is a wide band gap material with E$_g$ > 4.5 eV[10].

(a)

(b)
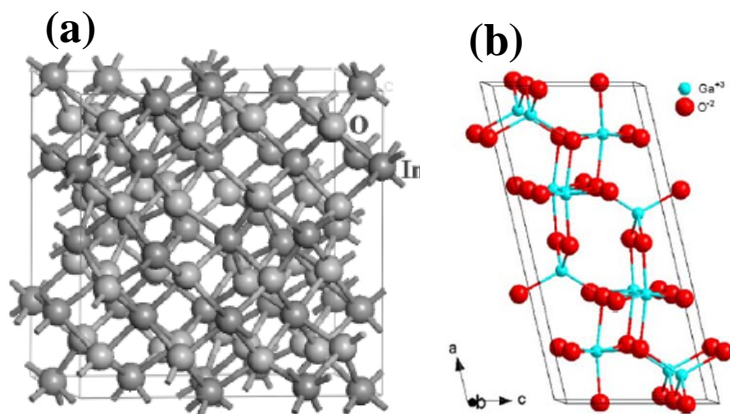
Fig. 3.1.4.: Crystal structure of (a) In_2O_3[15] (b) Ga_2O_3[16] [reprinted with permission from ref.15 and 16]

3.1.3.3. Role of Crystal structure

Crystal symmetry has a significant role to play in determining the electronic properties of TCOs[12]. Higher crystal symmetry is preferred for an unhindered conductivity. Lattice anisotropy affects the conductivity as it leads to non-uniform distribution of carrier donors. Apart from extended symmetry, local symmetry around the cation also contributes differently towards conductivity. Since conduction bands are formed from *s*-orbital of cations and *p*-orbital of anions, that anion polyhedra which facilitate maximal overlap is preferred. Oxygen octahedra is preferred over tetrahedra as it provides better *s-p* overlap. The cation's orbital contribution is also crucial. If anisotropic *p-* and *d-* orbitals of cations are lying close to conduction band minima and if they contribute, conductivity is found to decrease.

3.2. Scope of the Present Investigations

There have been various transparent conducting oxides which have been explored till date. Among all this, the most favourable TCO continues to be tin

doped indium oxide (ITO). We were interested in doping Ge into host oxides like In_2O_3, Ga_2O_3 and $Ga_{2-x}In_xO_3$ and have explored their electrical and optical properties.

3.3. Experimental Section

Ge-doped Ga_2O_3, Ge-doped $Ga_{2-x}In_xO_3$ and Ge-doped In_2O_3 were prepared by using the standard solid state methods. Appropriate ratios of In_2O_3 (Aldrich), Ga_2O_3 (Aldrich) and GeO_2 (Aldrich) were thoroughly ground in presence of isopropanol using mortar and pestle. The pelletized mixture was initially fired at 1423 K for 40 h on a platinum boat. Pelletization and firing with intermediate grinding was repeated at 1523 K for 40 h and 1673 K for 40 h until phase pure product was obtained. Percentage of weight loss was determined after each heating process. 10% and 20% GeO_2 precursor were used for doping in Ga_2O_3, $Ga_{1.6}In_{0.4}O_3$ and In_2O_3. ITO (6% Sn doped In_2O_3) was prepared as a reference sample. Oxygen vacancies were created by thermally quenching the final products (instantaneously taking out the pellet from 1673 K to room temperature). The obtained pellets were reduced under H_2 environment at 723 K for 5 h.

Powder x-ray diffraction (XRD) patterns of the products obtained after each round of heating were recorded with a Bruker-D8 X-ray diffractometer using Cu Kα radiation. Elemental compositions of the products were measured using inductively coupled plasma atomic emission spectroscopy (ICP-AES) on a Perkin Elmer's Optima 2100 DV spectrometer. Band gaps of the powdered products were measured using diffuse reflectance experiments performed on a Perkin-Elmer's Lambda 35 UV-visible spectrometer. Electrical resistivities of the samples were measured by employing the standard four-probe method using the resistivity option in the Physical Property Measurement System (PPMS), Quantum Design, USA.

3.4. Results and Discussion

3.4.1. X-ray Diffraction measurement

Ge doping was done in Ga_2O_3, $Ga_{1.4}In_{0.6}O_3$, In_2O_3. X-ray diffraction shows the phase purity of the compounds so formed (Fig.3.4.1). When Ga_2O_3 was doped with Ge, β-Ga_2O_3 structure (space group C2/m) was retained (Fig.3.4.1a)[17]. 10% and 20% doping of Ge showed impurity phases when heating was restricted to lower temperatures. Sintering temperature as high as 1673 K was inevitable for obtaining phase purity in these compounds. Even when 10% and 20% Ge precursors were used, ICP-AES measurement shows only 3.4% and 3.5% Ge. This shows the solubility of Ge to be less than 4% in Ga_2O_3.

Ge doping done in $Ga_{1.4}In_{0.6}O_3$ also shows 3.4 % and 3.3 % Ge on using 10% and 20% Ge precursors. These compounds also necessitate the need for higher sintering temperature and crystallized in *C2/m* space group. XRD peaks of $Ga_{1.4}In_{0.6}O_3$ are slightly shifted towards lower *2θ* values compared to pure Ga_2O_3 structure, which shows the incorporation of In^{3+} in the Ga_2O_3 lattice. Ge doping exhibits similar lattice parameters. X-ray Diffraction pattern of 3.3% Ge doped $Ga_{1.4}In_{0.6}O_3$ is shown in Fig.3.4.1a.

When 10% and 20% Ge was doped in In_2O_3, impurity phase ($In_2Ge_2O_7$) was retained until the temperature was raised to 1400 °C. Raveau et.al.[18] could not get pure phase on doping Ge in In_2O_3 probably because they didn't raise the temperature above 1573 K. The phase pure compound could be indexed with space group *Ia*-3 (Fig.3.4.1b) [19]. Here ICP-AES measurements show the presence of only 2.5% and 2.7% Ge when 10% and 20% Ge precursors were used, showing that solubility of Ge is not so high even in this case. Ours is one of the early reports of Ge in In_2O_3 lattice.
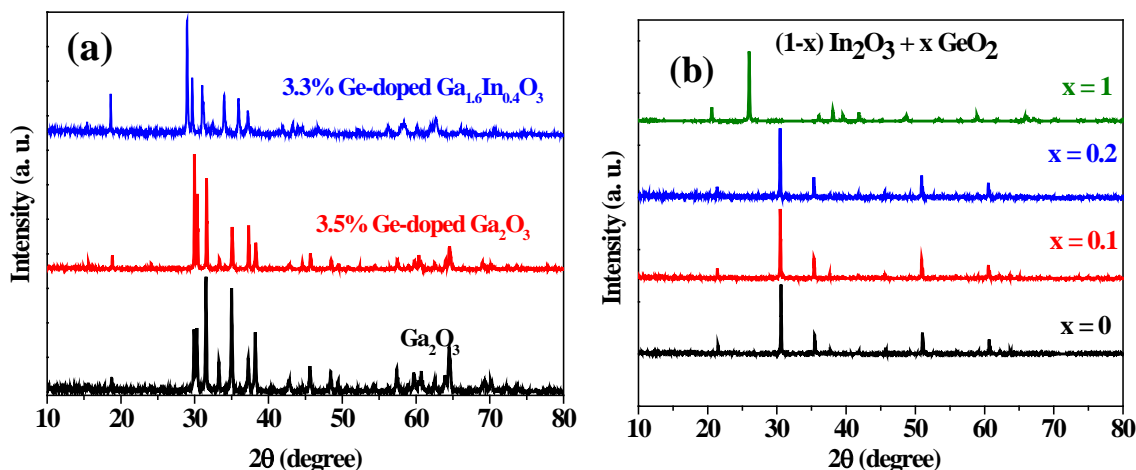
Fig. 3.4.1. (a) XRD pattern showing Ga$_2$O$_3$, 3.5% Ge-doped Ga$_2$O$_3$ and 3.3% Ge-doped Ga$_{1.4}$In$_{0.6}$O$_3$.(b) XRD patterns of Ge-doped In$_2$O$_3$ samples with 10% and 20% (x = 0:1 and 0.2) of Ge precursor.

3.4.2. Optical measurements

Diffuse reflectance measurements on solid samples were carried out at ambient conditions on Ge doped and undoped samples to determine the band gap of these compounds. On carrier doping, the band gap is likely to widen. In Ge doped Ga$_2$O$_3$ and Ga$_{1.4}$In$_{0.6}$O$_3$ there was no appreciable changes in the band edge, (Fig.3.4.2a) which remained almost as same as that of the host materials (4.59 eV and 3.92 eV for Ga$_2$O$_3$ and Ga$_{1.4}$In$_{0.6}$O$_3$ respectively). However, substantial change in the band gap was observed when Ge was doped in In$_2$O$_3$ (2.7 %). Band Gap increases from 2.88 eV in the host to 2.95 eV (Fig.3.4.2b) providing an evidence for Ge^{4+} doping in In$_2$O$_3$ lattice. This band gap widening can be attributed to the Moss-Burstein effect[13,14]. These materials do satisfy the necessary condition of transparency in the UV-Visible region.
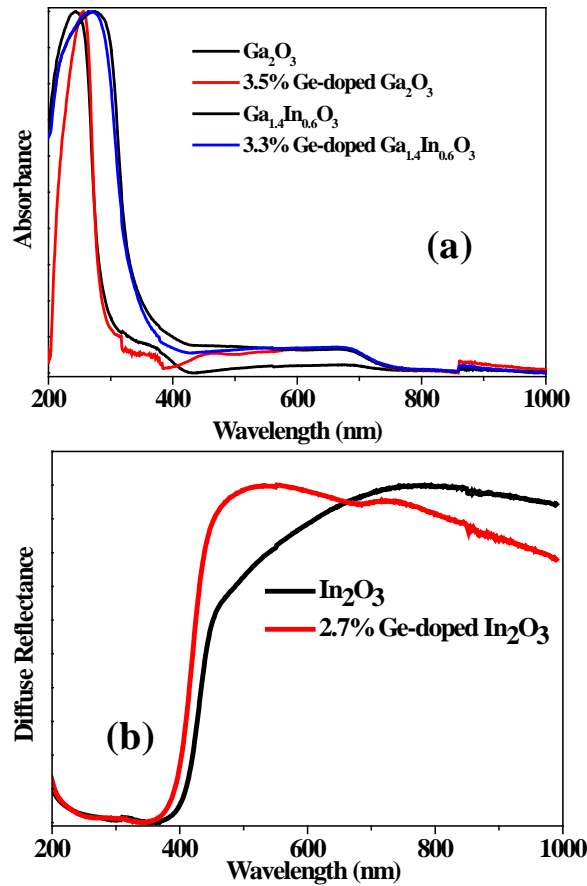
Fig.3.4.2: (a) Diffuse reflectance spectra for undoped and Ge-doped Ga_2O_3 and Ge-doped $Ga_{1.4}In_{0.6}O_3$ samples. (b) Diffuse reflectance spectra of In_2O_3 and Ge-doped In_2O_3.

3.4.3. Conductivity measurements

Four probe conductivity measurements were done on the host and Ge doped samples. These samples show a temperature dependence similar to that of a semiconductor and a decrease in resistivity as a result of doping. Ge doped Ga_2O_3 has resistivity in few tens of MΩ cm whereas Ge doped $Ga_{1.4}In_{0.6}O_3$ showed considerable improvement in its resistivity on H_2 reduction. Room temperature value of resistivity being 215 KΩ cm (3.3 % Ge doped). These samples show a temperature dependence similar to that of a semiconductor. . This is still far from that required for a TCO[8]. Among all the samples Ge doped In_2O_3 had the lowest resistivity values which improved on introduction of oxygen vacancies via thermal

quenching and H_2 reduction. The as-prepared sample has a resistivity of 13 mΩ cm at room temperature which shows subtle temperature dependence (16 mΩ cm at 10 K) unlike other Ga-based compounds (Fig.3.4.3a). This re-establishes the absence of $In_2Ge_2O_7$, impurity phase as this is highly insulating [18]. 2.7 % Ge doped samples when subjected to thermal quenching showed a decrease in resistivity to 5.7 mΩ at room temperature which remained unchanged in the entire temperature range (Fig.3.4.3a). Further reduction in resistivity was observed on subjecting the samples to H_2 reduction. Room temperature value reduced to ~1 mΩ cm with an interesting metallic behaviour. Thus resistivity further decreased as the temperature was reduced, reaching a value of 0.8 mΩ cm at 10 K (Fig.3.4.3a). This resistivity values shows that electrical conductivity has contributions from both dopant Ge^{4+} ions as well as from anion vacancies.
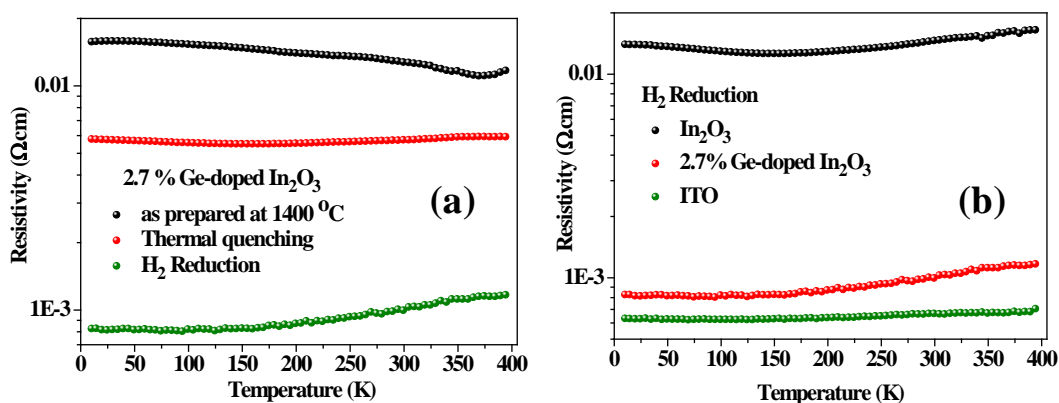
Fig.3.4.3: (a) Four-probe electrical resistivity vs. temperature plots of the 2.7% Ge-doped In_2O_3 sample reduced differently. (b) Four-probe electrical resistivity vs. temperature plots of In_2O_3, 2.7% Ge-doped In_2O_3 and ITO, after reducing in an H_2 environment.

We compare the 2.7% Ge doped In_2O_3 after H_2 reduction with In_2O_3 and ITO after H_2 reduction (Fig. 3.4.3b). This comparison shows us that resistivity of Ge

doped sample has sufficiently improved over the parent oxide (In_2O_3). It has reduced so much that it is close to that of ITO (~ 0.7 mΩ cm) and hence is a potential TCO material.

3.5. Conclusion

Employing standard solid state reactions at higher temperature, Ge doping was realized, though in small amounts ($\leq$ 3.5 %), in Ga_2O_3, $Ga_{1.4}In_{0.6}O_3$ and In_2O_3. Ge doping in Ga_2O_3 and $Ga_{1.4}In_{0.6}O_3$ was successful in getting highly transparent oxides but failed in making them conducting. The aim of obtaining a new transparent conducting oxide was met in the case of Ge doping done in In_2O_3 upon subjecting these samples to H_2 reduction. While we attribute shift in absorption band edge to Moss-Burstein effect, we find both dopants and anion vacancies responsible for imparting conductivity and behaviour to this material.

References

(1)   Badeker, K. *Ann. Phys* **1907**, *22*, 749.

(2)   Wu, X.; Coutts, T. J.; Mulligan, W. P. *J. Vac. Sci. Technol. A* **1997**, *15*, 1057.

(3)   Palmer, G. B. *Northwestern University* **1999**.

(4)   Edwards, D. D.; Mason, T. O.; Sinkler, W.; Marks, L. D.; Poeppelmeier, K. R.; Hu, Z.; Jorgensen, J. D. *J. Solid State Chem.* **2000**, *150*, 294.

(5)   Edwards, D. D.; Mason, T. O.; Goutenoire, F.; Poeppelmeier, K. R. *Appl. Phys. Lett.* **1997**, *70*, 1706.

(6)   Moriga, T.; Kammler, D. R.; Mason, T. O.; Palmer, G. B.; Poeppelmeier, K. R. *J. Amer.Ceram. Soc.* **1999**, *82*, 2705.

(7)   Palmer, G. B.; Poeppelmeier, K. R. *Solid State Sciences* **2002**, *4*, 317.

(8)   Hamberg, I.; Granqvist, C. G. *J. Appl. Phys.* **1986**, *60*, R123.

(9)   Granqvist, C. G.; Hultaker, A. *Thin solid films* **2002**, *411*, 1.

(10)   Aron, W.; Juarez, L. F. D. S.; Su-Huai, W. *J. Phys.: Cond. Matt.* **2011**, *23*, 334210.

(11)   Al-Dahoudi, N. *University of Saarland* **2003**.

(12)   Medvedeva, J. E.; Hettiarachchi, C. L. *Phys. Rev. B* **2010**, *81*, 125116.

(13)   Moss, T. S. *Proc. Phys. Soc.B* **1954**, *67*, 775.

(14)   Burstein, E. *Phys. Rev.* **1954**, *93*, 632.

(15)   Kong, X. Y.; Wang, Z. L. *Solid State Commun.* **2003**, *128*, 1.

(16)   Roehrens, D.; Brendt, J.; Samuelis, D.; Martin, M. *Journal of Solid State Chem.* **2010**, *183*, 532.

(17)   Geller, S. *J. Chem. Phys.* **1960**, *33*, 676.

(18)   Berardan, D.; Guilmeau, E.; Maignan, A.; Raveau, B. *Solid State Commun.* **2008**, *146*, 97.

(19)   Galasso, F. S. *Structure and properties of inorganic solids*, Oxford New York, Pergamon Press. **1970**.

PART 4

Brief Summary of studies in progress

4.1. Anion Doping in Zinc Oxide

Summary

Zinc oxide which is a wide gap semi-conductor is doped with nitrogen and fluorine employing a two-step synthetic procedure involving ammonolysis. X-ray photoelectron spectroscopy studies show the samples to be heavily doped. These samples as expected, reduced the band gap of ZnO to ~ 3.04 eV. Further studies are required to confirm this as well as to determine the chemical state in which the dopants are present in these samples.

4.1.1. Introduction

Zinc Oxide is a wide band gap semiconductor with a band gap of 3.37 eV[1] and has very interesting piezoelectric properties as it crystallizes in a non-centrosymmetric space group. Band gap of these wide band gap materials can be tuned by introducing dopants which form intermediate levels between valence and conduction band.

4.1.1.1. Properties of ZnO

Zinc Oxide cyrstallizes in a hexagonal wurtzite structure with space group $P6_3mc$. Wurtzite structure can be described as one in which Zn is tetrahedrally surrounded by oxygen and vice-versa. These are stacked along the c-axis alternatively. Zinc oxide does crystallize in other crystal structures as well, like zinc blend and rock salt structure, but at normal temperature and pressure wurtzite is the stable phase. Zinc oxide is largely ionic and the electronegativity values of Zn^{2+} and O^{2-} are 3.44 and 1.63 respectively.

Fig.4.1.1.1: Schematic showing the wurtzite structure of ZnO [2].[reprinted with permission from ref.2]

4.1.1.2. Optical properties of ZnO

Zinc oxide is a direct band gap semi-conductor (3.37 eV). ZnO is known to have two bands namely, UV emission band which is the band edge emission and broad defect emission band[1]. Band edge emission is known to occur in the range of 373 - 390 nm. In nanomaterials, band edge is known to shift as the concentration of defects increases. Thus the position of these bands will vary depending on factors like size, porosity etc. which decides the surface-to-volume ratio. Zinc oxide is known to have different types of defect emissions namely green, yellow and orange-red emission. The origin of some of these emissions like green emission is still under debate whereas yellow emission is almost certainly believed to be from oxygen interstitials.[1] Fig.4.1.1.2 shows some of the possible deep level emissions found in ZnO.
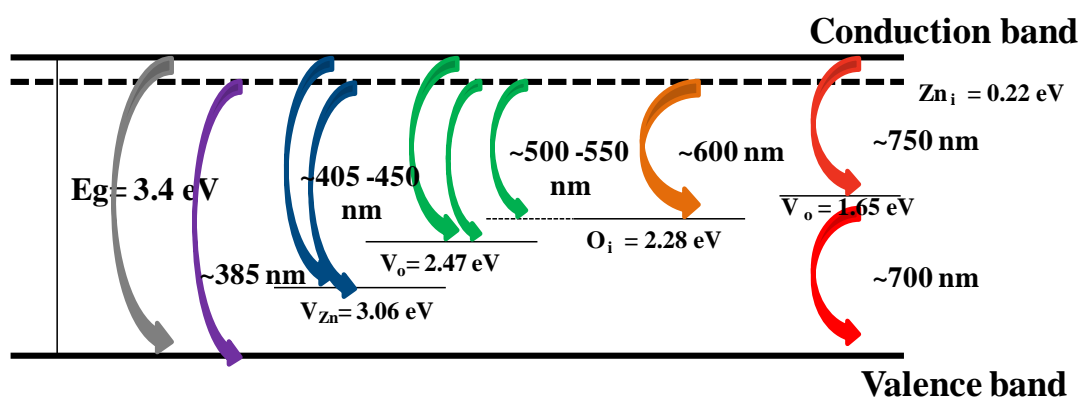
Fig.4.1.1.2: Schematic showing the possible deep level emissions in ZnO.[3-5]

4.1.1.3. Anion Doping in ZnO

Nitrogen has an electronegativity value and ionic radii that is comparable to that of oxygen and hence can be a possible substituent for oxygen. When nitrogen is substituted for oxygen, it forms a band which is N $2p$ in nature[6]. Due to the less

electronegativity of nitrogen, this band will lie above oxygen *2p* band. Thus the band gap can be tuned with the amount of nitrogen that is incorporated in the lattice.

Fluorine Doping

Fluorine also has ionic radius comparable to that of oxygen and is another potential anion dopant. But fluorine does not affect the band structure critically. It increases the surface acidity and the surface oxygen vacancies making the material more photochemically active[6].

Table 4.1.1: Table showing the ionic sizes and electronegativity values

Element	Ionic radii (Shannon-Perwitt)	Electronegativity (Pauling's scale)
Nitrogen	1.46	3.0
Oxygen	1.38	3.5
Fluorine	1.31	4.0

In recent years, co-doping (i.e, doping both p-type and n-type dopants) have been explored quite extensively[7-9] for band gap engineering mainly for catalytic purposes.

4.1.2. Scope of the present investigations

Band gap of zinc oxide is so large that it absorbs in the UV region only. If this band gap is reduced then ZnO can be made to absorb in the visible region and hence can be used as a potential photochemical catalyst. There are various attempts towards achieving this goal in literature. We are interested in substituting oxygen with nitrogen and fluorine so as to modify the band structure of ZnO.

4.1.3. Experimental section

Co-doping of ZnO was achieved in two step reaction. In the initial step, ammonium fluoride (NH_4F) (0.22g) was taken in 9.4 mL water and 5mL methanol (in order to maintain 60% volume of autoclave bomb). To the above solution, $ZnSO_4$ (0.89g) was added with vigorous stirring. The ratio of $Zn : NH_4F$ was varied to obtain series of samples. These as-prepared samples were kept in hot air oven for 24 hours at 180^0 C and then annealed at 723 K for 5 hrs. Finally they are subjected to ammonolysis at 773 K for 5 hrs yielding pale yellow coloured compounds.

The N-F –codoped ZnO was characterized by X-ray diffraction (XRD) in a Bruker-D8 diffractometer. X-ray photoelectron spectroscopy (XPS) measurements were done using Omicron ESCA using EAC 2000 SPHERA analyzer (dual source), inorder to determine quantitatively the amount of nitrogen and fluorine in the samples. Spectra were deconvoluted using Fityk software using Gaussian spectral shape. Optical and electronic properties were investigated using UV–Vis spectroscopy and fluorescence spectroscopy which were recorded using a Perkin Elmer Model Lambda 900 spectrophotometer and Perkin Elmer model LS 55 spectrophotometer.

4.1.4. Results and Discussion

4.1.4.1. Structure determination

Samples obtained after hydrolysis when heated at 723 K were found to be pure ZnO crystallizing in the wurtzite structure. These samples when ammonolysed retained the same structure and hence the phase purity. But these samples had a pale yellow colour uncharacteristic of pure ZnO. This signals a possibility of doping.
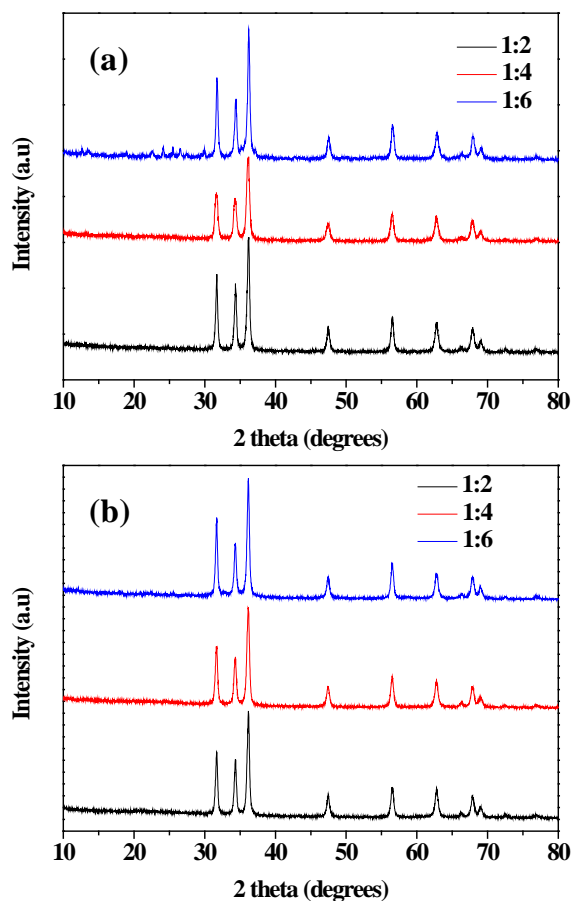
Fig.4.1.4.1: X-ray Diffraction pattern of the samples (a) before ammonolysis and (b) after ammonolysis.

4.1.4.2. X-ray Photoelectron Spectroscopy (XPS) analysis

Solid samples were analyzed after ammonolysis using x-ray photoelectron spectroscopy (XPS). This helps in determining the percentage of dopant, namely nitrogen and fluorine present in the sample. Fig.4.1.4.2 shows the XPS peaks along with the fitted curves for the sample having 1:2 ratio of $Zn : NH_4F$.
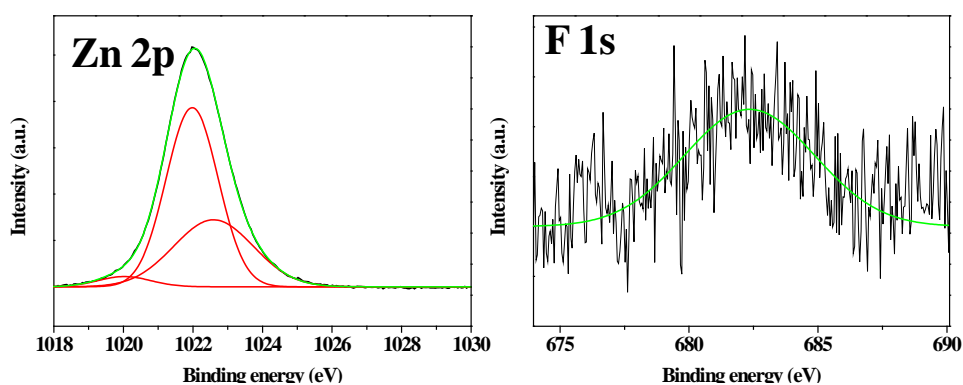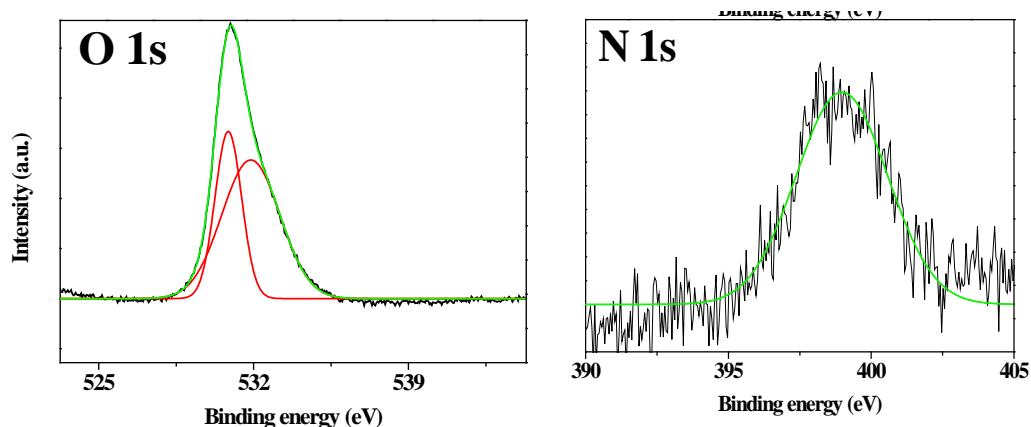
Fig.4.1.4.2: XPS peaks along with the peak fits for Zn 2p, F 1s, O 1s and N 1s for sample with Zn : NH₄F ratio 1:2.

Percentage of various ions present in the sample was computed and is shown in table. It can be seen that % N and % F was 4.7% and 3.2 % respectively.

Samples in which the ratio of NH₄F used in the hydrothermal reaction was doubled (1:4), had 8.1 % of fluorine and 9.8 % nitrogen (Fig.4.1.4.3 and table 4.1.4.2).
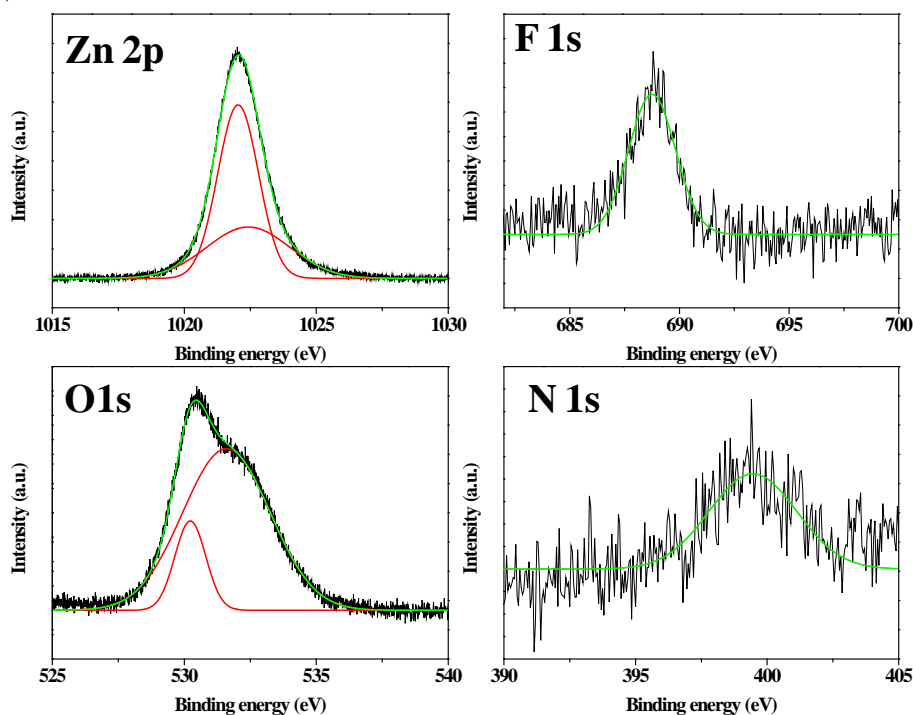
Fig.4.1.4.3: XPS peaks along with the peak fits for Zn 2p, F 1s, O 1s and N 1s for sample with Zn : NH₄F ratio 1:4.

Samples in which the ratio of NH_4F used in the hydrothermal reaction was further increased to a ratio of Zn : NH_4F to be 1:6, had 16 % of fluorine and 12 % nitrogen.
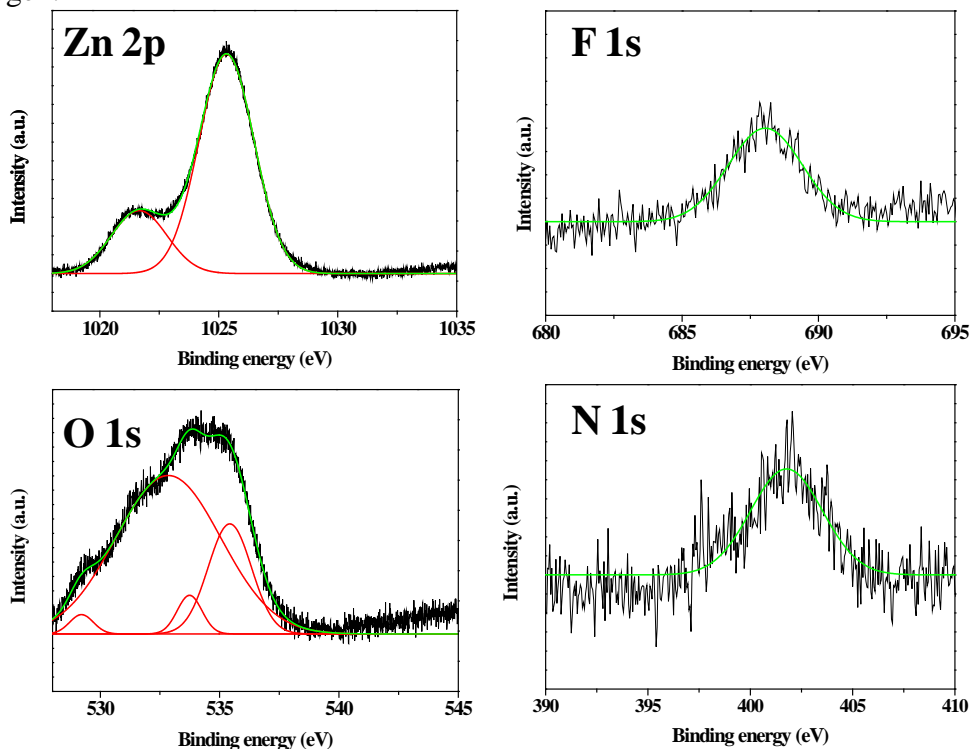
Fig.4.1.4.4: XPS peaks along with the peak fits for Zn 2p, F 1s, O 1s and N 1s for sample with Zn : NH_4F ratio 1:6.

From all the fitted spectra, it can be seen that Zn and O can be fitted with more than one peak indicating different chemical environments. Oxygen peaks in the range 529-530 eV are attributed to lattice oxygen, 530.7-531.6 ev to non-stoichiometric oxygen, 533 eV to hydroxyl groups etc.[10-12] The number peaks that can be fitted to O increases as we go from 1: 2 sample to 1: 6. The reason for this is not yet confirmed. N_o-Zn peak is assigned values like 397.7 eV - 396.4 eV[13] and $(N_2)_o$-Zn was assigned positions like 407 eV- 405.1 eV[13] (here N_o and $(N_2)_o$ are nitrogen atom and molecule occupying oxygen positions respectively). Since ammonia and ammonium fluoride are used as N sources, there is a possibility of N-H bonds also appearing in the sample which has a literature value of 400.4 eV.[14] We

have in our samples N peak having values 398.97 eV (1:2), 399.45 eV (1:4), 401.52 eV (1:6). This could be assigned to N_o-Zn as well as N-H bonds. But further confirmation is required in this regard.

4.1.4.3. Optical characterization

Nitrogen is less electronegative than oxygen and hence is expected to give a band above the valence band of oxygen. Fluorine substitution on the other hand does not alter the band structure much but is essential to maintain charge neutrality. N-F codoped samples obtained does shift the band edge of ZnO from 3.2 eV to ~ 3.04 e V. But there is a slight uncertainty in the results obtained as correlation between XPS and UV data is lacking. Further studies, extending this to higher concentrations are in progress to resolve this issue.
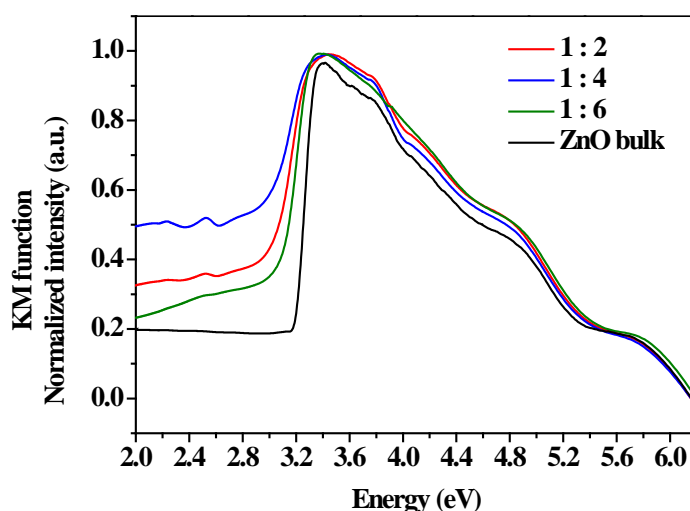
Fig.4.1.4.5: UV data showing red shift in band edge emission with doping.

Photoluminescence (PL) spectra were recorded on these samples at an excitation wavelength of 350 nm. Intrinsic band edge emission occurs around 390 nm. This band red shifts as the amount of the dopant increases whereas the broad defect bands remains almost unaffected due to doping. PL spectra show distinct features at 441 nm, 484 nm, 462 nm and 421 nm. These could be due to intrinsic

defects present in ZnO like oxygen vacancy, zinc vacancy, zinc interstitial etc.[1] But as N will act as acceptor impurity and F as donor impurity, transitions involving these levels may also contribute to defect spectra obtained. Assignment of different peaks to different transitions requires a detailed knowledge of the position and nature of the defect levels present in the system.
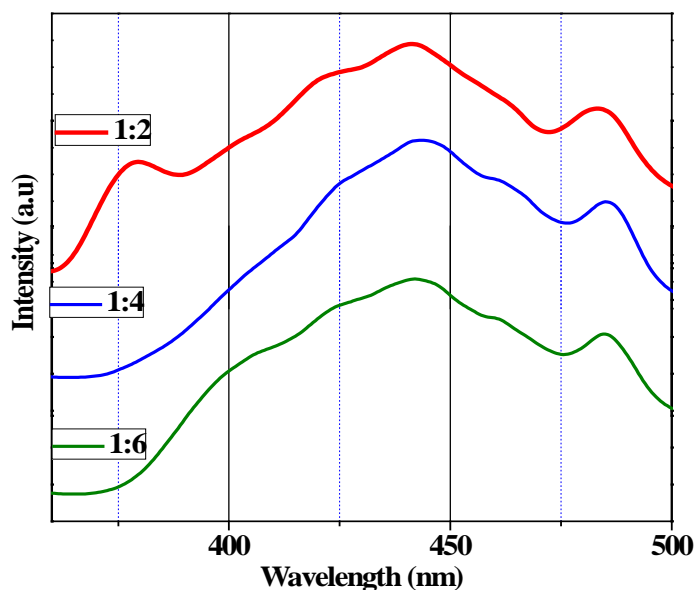
Fig.4.1.4.6: Photoluminescence spectra of doped ZnO recorded at an excitation wavelength of 350 nm showing red shift in band edge emission.

4.1.4.1: Table showing the PL band positions of N,F-co-doped ZnO

1:2	1:4	1:6	Literature explanations *
378.6 nm (s)	---- (Shifted to 387.6 nm)	---- (Shifted to 398.6 nm)	Band edge emission[1]
397.3 nm (w)	402.8 nm(w)	-	Zinc vacancy [15]
421.7 nm (m)	426.1 nm (m)	426.1 nm (m)	Zinc interstitial [16]
443.7 nm (s)	448.2 nm (s)	448.6 nm (s)	Shallow donor to valence band [17]
461.4 nm (m)	464.5 nm (m)	463.4 nm (m)	Oxygen and zinc vacancies/interstitials and complexes [18]

482.8 nm (m)	484.3 nm (m)	484.3 nm (m)	Transition b/w oxygen vacancy and oxygen interstitial.[19]
*s = strong, m = medium, w = weak			

We find that there is a definite variation in the relative intensities of PL emission on doping N and F in ZnO. But further studies to confirm this findings are required .

4.1.5. Conclusion

Zinc oxide has been doped with anion dopants like nitrogen and fluorine through a step process. These dopants are found to red-shift the band edge of ZnO. These are preliminary results obtained in this regard. Further tuning of band –edge, if successfully done, would make ZnO a potential photochemical catalyst .

References

(1)   Djurišić, A. B.; Leung, Y. H. *Small* **2006**, *2*, 944-961.

(2)   Ashrafi, A.; Jagadish, C. *J. Appl. Phys.* **2007**, *102*, 071101-12.

(3)   Ahn, C. H.; Kim, Y. Y.; Kim, D. C.; Mohanta, S. K.; Cho, H. K. *J. Appl. Phys.* **2009**, *105*, 013502.

(4)   Alvi, N. H.; ul Hasan, K.; Nur, O.; Willander, M. *Nanoscale Res. Lett.* **2011**, *6*, 130

(5)   Alvi, N. H. *Linköping University* **2011**.

(6)   Seibel II, H. A. *The Ohio State University* **2009**.

(7)   Seibel II, H. A.; Karen, P.; Wagner, T. R.; Woodward, P. M. *J. Mater. Chem.* **2009**, *19*, 471.

(8)   Li, D.; Haneda, H.; Hishita, S.; Ohashi, N. *Chem. Mater.* **2005**, *17*, 2588.

(9)   Li, D.; Haneda, H.; Hishita, S.; Ohashi, N. *Chem. Mater.* **2005**, *17*, 2596.

(10)   Brigg, D. E. *Handbook of X-ray and Ultraviolet Photoelectron Spectroscopy,* **1977**, *Heydon, London,*, 295.

(11)   Shinde, S. S.; Rajpure, K. Y. *J. Alloys Compd.*, *509*, 4603.

(12)   Lee, D.-H.; Chun, Y. S.; Park, K.-H.; Kim, S.; Lee, S. Y. *Trans. Electr. Electron. Mater.* **2011**, *12*, 200.

(13)   Jiao, S.; Lu, Y.; Zhang, Z.; Li, B.; Yao, B.; Zhang, J.; Zhao, D.; Shen, D.; Fan, X. *J. Appl. Phys.* **2007**, *102*, 113509.

(14)   Boqian, Y.; Peterxian, F.; Ashok, K.; Katiyar, R. S.; Marc, A. *J. Phys. D: Appl.Phys.* **2009**, *42*, 195402.

(15)   Wu, X. L.; Siu, G. G.; Fu, C. L.; Ong, H. C. *Appl. Phys. Lett.* **2001**, *78*, 2285.

(16)   Lin, B.; Fu, Z.; Jia, Y. *Appl. Phys. Lett.* **2001**, *79*, 943.

(17)   Xue, Z. Y.; Zhang, D. H.; Wang, Q. P.; Wang, J. H. *Appl. Surface Sci.* **2002**, *195*, 126.

(18)   Dai, L.; Chen, X. L.; Wang, W. J.; Zhou, T.; Hu, B. Q. *J. Phys.: Cond. Matt.* **2003**, *15*, 2221.

(19)   Mahamuni, S.; Borgohain, K.; Bendre, B. S.; Leppert, V. J.; Risbud, S. H. *J. Appl. Phys.* **1999**, *85*, 2861.

4.2. Synthesis and Characterization of EuZrO$_3$

Summary

Europium based oxides have interesting magnetic properties. EuZrO$_3$ was synthesized using sol-gel technique (with some amount of carbon impurity).Magnetic studies revealed antiferromagnetic transition at 4.1 K with a positive Weiss constant indicative of the co-existence of ferromagnetic and antiferromagnetic interactions. Further studies for exploring dielectric nature and magnetodielectric effect are in progress.

4.2.1. Introduction

Materials which combine magnetism and insulating properties are much in demand as they find application in spintronic devices, high-frequency oscillators and the like. Various materials are explored for these properties and among these Eu^{2+} containing compounds are quite interesting as they span a wide variety of magnetic properties. EuO was discovered to be a ferromagnet in 1960s[1]. Eu^{2+}M^{4+}O$_3$ (M = Nb, Ti, etc.) also have quite intriguing magnetic properties. EuNbO$_3$ is known to be a ferromagnetic metal but oxygen vacancies can make it a superconductor of T$_c$ = 6K[2-4]. EuTiO$_3$ is known to be an antiferromagnet with T$_N$ = 5.5 K and a quantum paraelectric material[5,6]. EuZrO$_3$ is also known to be an antiferromagnet with T$_N$ = 4.1 K[7-9]. These Eu^{2+} based compounds have quite interesting magnetic properties.

Magnetism arises from the coupling between spins in a magnetic material. This interaction is quantum mechanical in nature and can be given by Heisenberg's exchange integral.

$$H_{ij} = -J_{ij} \, S_i . S_j.$$

There are various magnetic exchange pathways possible in a magnetic material. They are namely i) Direct Exchange ii) Indirect exchange and iii) Superexchange[10-12].

i)   Direct exchange :

Direct exchange originates when there is an overlap of electronic wave function. This overlap is effective only when the spins are closely spaced and decays exponentially with distance. Since parallel spins tends to stay apart as dictated by Pauli's exclusion principle, direct exchange occurs between antiparallel spins.

ii)   Indirect exchange:

When the spins are separated from each other, then the magnetic interaction between them occurs via indirect exchange. In metals, this indirect exchange is facilitated by conduction electrons and is called RKKY (Ruderman, Kittel, Kasuya and Yoshida) interaction. Here, magnetic ions spin polarize the conduction electrons in their vicinity and this is in turn felt by another magnetic ion within the range .This interaction has a damped oscillatory nature. Thus the interaction between the spins can be ferromagnetic /anti-ferromagnetic depending on the distance between them.

In rare earth oxides, were *4f* electrons are well shielded by *5s* and *5p* electrons, direct exchange between them is not favoured. But indirect exchange is possible between them via 5d electrons. It is believed that 4f electrons are excited to 5d levels and they interact with the neighbouring ions.

iii)   Superexchange

Superexchange mechanism first proposed by Kramers and formulated by Anderson operates when magnetic ions are quite far apart and are connected via ligands or anions. This interaction depends on the type of the transition metal and the bond angle between them. It can be tuned from anti-ferromagnetic to ferromagnetic by changing the bond angle from 180° to 90°. This has been evolved to be used in transition metal oxides mainly by Goodenough and Kanamori.

If Fe^{3+} ions are connected by an oxygen anion, then the oxygen can transfer a *2p* electron to Fe^{3+} .Since it is covalent mixing, the spin on Fe^{3+} will be parallel to that of O^{2-} . But as the spins on O^{2-} are anti-parallely arranged according to Pauli's exclusion principle, the other Fe^{3+} will be in turn anti-parallel to the first one.

4.2.1.1. Magnetic mechanism in Eu²⁺ compounds

Europium is a rare earth element and is magnetic in nature. Eu^{2+} has an electronic configuration of $1s^2\ 2s^2p^6\ 3s^2p^6d^{10}\ 4s^2p^6d^{10}f^{\ 7}\ 5s^2p^6$ .Since *4f* electrons remains shielded here, direct exchange cannot be effective. Therefore the possible exchange mechanism is indirect exchange or superexchange[12].

i)   Indirect exchange

Eu^{2+} based insulators like $EuTiO_3$, interact through the overlap of 5d orbitals. The exchange constant is given by

$$J \sim J_{intra}\ b^2/U^2,$$

where J_{intra} is the intra-atomic exchange parameter, *b* the transfer integral between Eu^{2+} ions and *U* the energy separation between *4f* and *5d* states. Thus exchange constant depends on the energy difference between *4f* and *5d* states in different Eu compounds and distance between Eu^{2+} centres.   In Eu^{2+} based semiconductors, indirect exchange operative is RKKY interaction. The exchange constant here is given by,

$$J \sim \frac{\cos(2k_F\ R)}{(k_FR)^3}$$

where k_F is the Fermi wave function.

ii) **Superexchange**

Superexchange in Eu-based compounds are more involved and complicated than that of transition metals. There are different possible interactions. Kasuya[13] proposed three competing mechanisms :

i)   The Kramers-Anderson superexchange (J_{KA}) : Here the *4f* electrons couple to *2p* electrons of oxygen similar to that seen in transition metals. This exchange is quite weak.

ii)   *d−f* exchange interaction (J_{df}) : Here *2p* electrons are excited to the *5d* levels and then these electrons couple to nearby Eu ions through *d-f* exchange.

iii)   Combination of J_{KA} and J_{df} : Here bonding and anti-bonding levels are formed between O 2p and Eu 5d states. An electron excited to the anti-bonding level 2p-5d interacts with the *4f* levels of the neighbouring Eu ions.

4.2.1.2. Magnetodielectric effect in Eu-based compounds

Coupling between magnetic and electric order parameters are quite important from the technological point of view. These materials are called ***magnetoelectric materials*** if they have spontaneous polarization and are called ***magnetodielectrics*** if this condition is not met. Among Eu^{2+} based compounds, $EuTiO_3$ is a very prominent example for magnetodielectric compound. It is a well known quantum paraelectric. The dielectric data shows anomaly at the magnetic transition temperature though it is not ferroelectric as such. Thus, the ferroelectricity is possibly suppressed by quantum-mecahnical fluctuations at this low temperature[14]. Dielectric properties are related to a soft-phonon mode whose frequency decreases to zero as temperature

decreases to zero. This mode depends largely on the electron density of the Ti-O bond. Thus in a compound with similar structure Eu^{2+}M^{4+}O$_3$, change in the electron density of the M-O bond should have signatures on the dielectric properties and more importantly on the magnetodielectric coupling[8].

4.2.2. Scope of the present investigations

EuTiO$_3$ being a celebrated quantum paraelectric with quite high magnetodielectric effect (7% at 1.5T) [5], we were interested in studying other Eu^{2+}M^{4+}O$_3$ systems. In this section, preliminary results obtained for EuZrO$_3$ is discussed.It is proposed to study EuHfO$_3$ as well.

4.2.3. Experimental section

Europium zirconate was made by sol-gel method. Here Eu$_2$O$_3$ was taken as the Eu source and Zr(OC$_4$H$_9$)$_4$ as the zirconium source. Europium nitrate was made by dissolving Eu$_2$O$_3$ in nitric acid. To this solution Zr(OC$_4$H$_9$)$_4$ in 1-butanol (Aldrich) dissolved in 1-butanol was added in the molar ratio 1 : 2 (Eu$_2$O$_{3:}$ Zr(OC$_4$H$_9$)$_4$). This was mixed thoroughly by stirring and then citric acid solution was introduced to facilitate gel formation. This was kept at a temperature of 323 K until it formed a thick clear gel and was kept in an oven set at 363 K for 3 days. The resulting compound was heated at 623 K and 773 K for 10 h each in air. This was then heated in H$_2$ atmosphere upto 1473 K in intermediate steps.

The samples so formed were analyzed using Bruker-D8 diffractometer. (Cu Kα radiation (λ=1.54Å)).   FESEM and EDAX were done on this sample using NOVA NANOSEM 600 (FEI, The Netherlands).Magnetic measurements were done using MPMS SQUID VSM, Quantum Design, USA. Further studies are in progress.

4.2.4. Results and Discussion

4.2.4.1. Structure Determination

The phase purity of the sample was determined by profile fitting the XRD data. EuZrO$_3$ was believed to crystallize in cubic *Pm-3m* space group[15] but recent reports have been supporting that it crystallizes in *Pbnm*[7,9] space group. Our data is found to fit almost well with both the space groups as shown in Fig.4.4.1. When fitted with cubic *Pm-3m* space group, it gives a = 4.1048(6) whereas when fitted with *Pbnm* space group it gives lattice parameters of: a = 4.1048 (7), b = 4.1062(6), c = 4.1057(9). It can be seen that a,b,c, values are quite close to each other. To resolve the space group better XRD data or neutron data are required. Further studies in this regard are under progress.
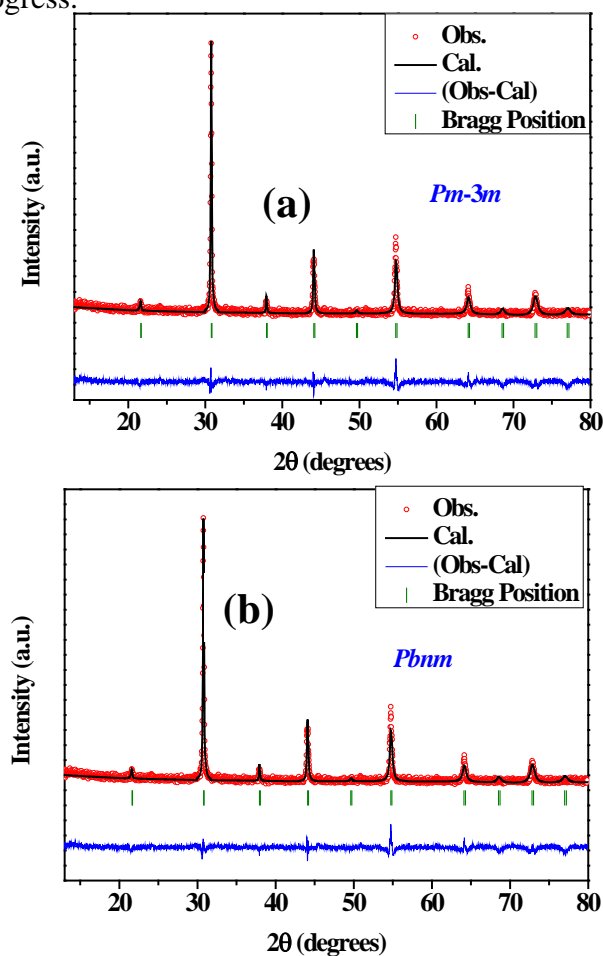

Fig.4.2.4.1.: X-ray diffraction pattern profile matched for space group a) Pm-3m b) Pbnm are shown.

Though the sample was pure from XRD analysis it had both black and yellow coloured particles. While the literature reports states that EuZrO$_3$ is yellow in colour. Thus Energy dispersive x-ray spectroscopy (EDAX) was done on the sample and it showed carbon as an impurity as shown in Fig.4.4.2. This would be an outcome of the organic precursors used during the sol-gel synthesis.
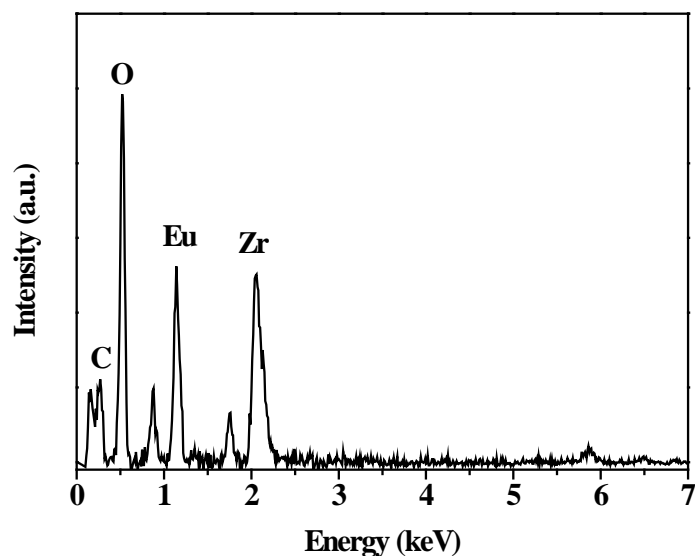
Fig.4.2.4.2: EDX spectra for EuZrO$_3$.

4.2.4.2. Magnetic studies

Since amorphous carbon is a non-magnetic impurity, magnetic studies were done on this sample using SQUID magnetometer. Field cooled (FC) and Zero field cooled (ZFC) measurements done at 100 Oe shows a kink around 4.1 K which is the antiferromagnetic transition temperature. Magnetic moment as a function of magnetic field was done at a temperature of 2 K. This hysteresis was observed by Zong et.al. as well and have attributed this behaviour to the flipping of Eu^{2+} moments gradually into a ferromagnetic arrangement [7]. Magnetization plotted as a function of magnetic field (Fig.4.4.3 b) shows a saturation magnetization value of about ~ 4 μ_B. Theoretical spin-only magnetic moment for Eu^{2+} is 7 μ_B (S = 7/2). The dilution in the magnetization value is expected to be due to the presence of carbon impurity.

Linear fitting the data of inverse molar susceptibility yields Weiss temperature (θ_W) of + 0.15 K (Fig.4.4.4). This positive value of θ_W shows the co-existence of both ferromagnetism and anti-ferromagnetism in the system[7,8].
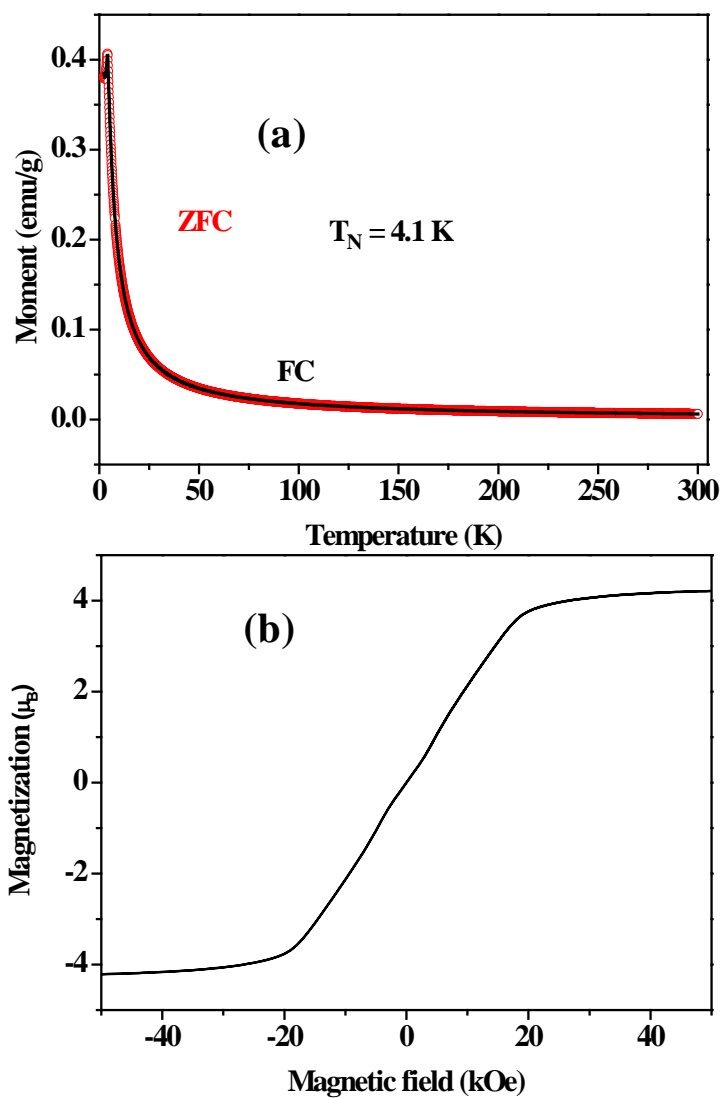
Fig.4.2.4.3: (a) Magnetizaion data as a function of temperature along with an inset showing χ plotted as a function of temperature and (b) magnetization measured as a function of field at 2 K.
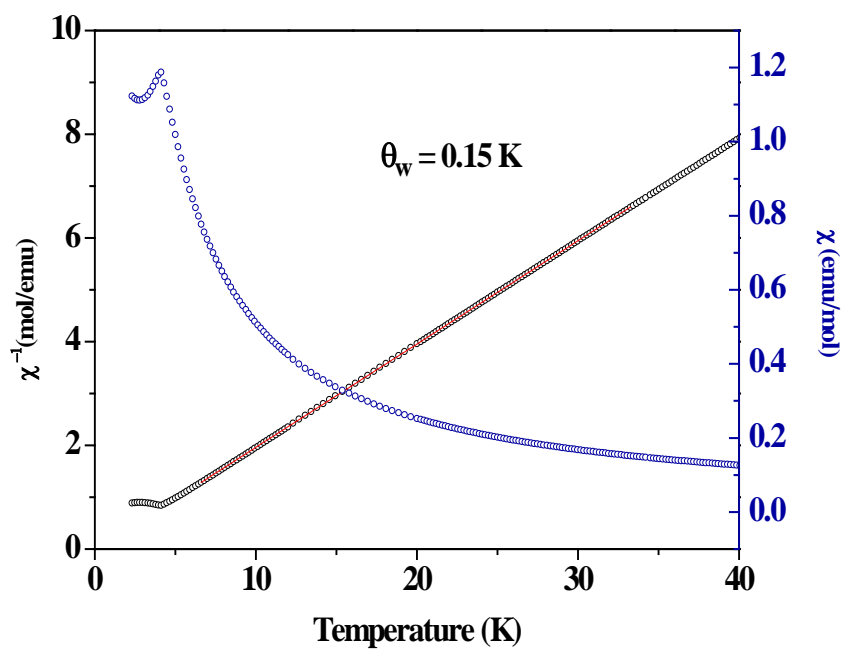
Fig.4.2.4.4.: Plot of molar magnetic susceptibility χ and χ^{-1} as a function of temeprature

4.2.5. Conclusion

EuZrO$_3$ was made via sol-gel method and magnetic properties were studied. This is an anti-ferromagnet with T$_N$ = 4.1 K. Since carbon is present as an impurity in the sample further studies of electric and magnetoelectric properties willbe done only after removing the traces of carbon.

References

(1)   Matthias, B. T.; Bozorth, R. M.; Van Vleck, J. H. *Phys. Rev. Lett.* **1961**, *7*, 160.

(2)   Zubkov, V. G.; Tyutyunnik, A. P.; Pereliaev, V. A.; Shveikin, G. P.; Kohler, J.; Kremer, R. K.; Simon, A.; Svensson, G. *J. Alloys Compd.* **1995**, *226*, 24.

(3)   Ishikawa, K.; Adachi, G.; Shiokawa, J. *Mater.Res.Bull.* **1981**, *16*, 419.

(4)   Strukova, G. K.; Shovkun, D. V.; Zverev, V. N.; Batov, I. E.; Zver'kov, S. A.; Khasanov, S. S. *Physica C* **2001**, *351*, 363.

(5)   Wu, H.; Shen, W. Z. *Solid State Commun.* **2005**, *133*, 487.

(6)   Katsufuji, T.; Takagi, H. *Phys.Rev.B* **2001**, *64*, 054415.

(7)   Zong, Y.; Fujita, K.; Akamatsu, H.; Murai, S.; Tanaka, K. *J. Solid State Chem.* **2010**, *183*, 168.

(8)   Kolodiazhnyi, T.; Fujita, K.; Wang, L.; Zong, Y.; Tanaka, K.; Sakka, Y.; Takayama-Muromachi, E. *Appl. Phys. Lett.* **2010**, *96*, 25290.

(9)   Viallet, V.; Marucco, J. F.; Saint, J.; Herbst-Ghysel, M.; Dragoe, N. *J. Alloys Comp.* **2008**, *461*, 346.

(10)   Spaldin, N. A. *Magnetic materials - fundamentals and applications , Cambridge University Press,New York* **2010**.

(11)   Cullity, B. D.; Graham, C. D. *Introduction to magnetic materials, A. Wiley & Sons, Inc. publication* **2009**.

(12)   Zong, Y. *Kyoto University* **2010**.

(13)   Kasuya, T. *IBM J. Res. Dev.* **1970**, *14*, 214.

(14)   Rajeev, R.; Hasan Sadat, N.; Rossitza, P. *J. Phys.: Cond. Matt.* **2007**, *19*, 406217.

(15)   Shafer, M. W. *J. Appl. Phys.* **1965**, *36*, 1145.

Part -5

Other work done by the author

Other work done by the author

Next article is reproduced by permission of The Royal Society of Chemistry
(http://pubs.rsc.org/en/content/articlelanding/2010/dt/b927355g)

One-step synthesis of high-purity fluorous-capped inorganic nanoparticles†

Rakesh Voggu, Ajmala Shireen and C. N. R. Rao*

Making use of the fact that perfluorohydrocarbon, and hydrocarbon solvents become miscible at high temperatures, highly pure inorganic nanoparticles capped with fluorous labels have been generated in a one-step synthesis. The procedure involves taking the reactants in a hydrocarbon+perfluorohydrocarbon mixture along with a fluorous reagent and carrying out the reaction at elevated temperatures. On cooling the reaction mixture, fluorous-capped inorganic nanoparticles dispersed in the perfluorohydrocarbon are obtained.

Fluorous chemistry is a novel method employed for the synthesis and purification of organic materials.[1] In this method, one attaches a fluorous reagent label such as a perfluoroalkanethiol or amine to a substrate and extracts the adduct into a perfluorohydrocarbon. Such separation is favored by fluorine-fluorine interaction between the fluorous reagent and the perfluorohydrocarbon, perfluorohydrocarbons being immiscible with water as well as hydrocarbons at room temperature. There are a few reports in the literature related to the preparation of nanoparticles capped with fluorous capping agents.[2,3] Such fluorous-capped nanoparticles tend to be highly pure because of the method employed. Fluorous separation is generally employed as a post-synthetic technique for the purification of materials. The method generally employed requires two steps, one involving the synthesis of the desired product in a hydrocarbon or an aqueous medium and the second involving the transfer to a fluorocarbon medium after attaching the fluorous-label to the product (nanoparticles). Fluorous-capped nanoparticles are of special interest due to their high purity as well as the superhydrophobic nature.[2c,4] Furthermore, the perfluorohydrocarbon medium with a very low refractive index of 1.23 enables the generation of inorganic nanomaterial in the most nonpolar medium possible. In this communication, we describe a novel fluorous chemical procedure for the one-step synthesis cum purification of inorganic nanoparticles. For this purpose, we have made use of the fact that perfluorohydrocarbons (PFC) and hydrocarbons become miscible at high temperatures and become biphasic only on cooling to room temperature.[1] We have prepared inorganic nanoparticles in a boiling mixture of a hydrocarbon and a PFC in the presence of a fluorous reagent which acts as the capping agent. The reaction mixture, on cooling, becomes biphasic with the PFC layer containing the fluorous-capped nanoparticles as shown in Fig. 1. By employing this procedure, we have prepared
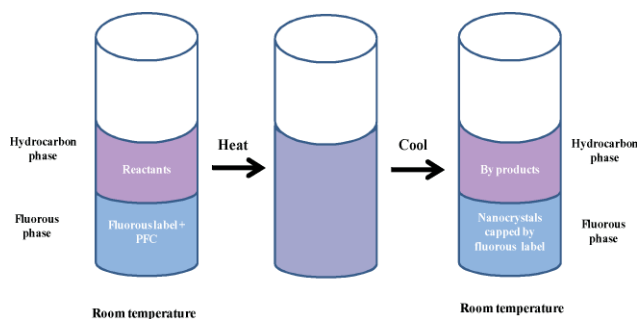
Chemistry and Physics of Materials Unit, New Chemistry Unit and CSIR Centre of Excellence in Chemistry, Jawaharlal Nehru Centre for Advanced Scientific Research, Jakkur P. O., Bangalore, 560064, India. E-mail: cnrrao@jncasr.ac.in; Fax: +91 80 22082760
† Electronic supplementary information (ESI) available: X-ray diffraction patterns of nanoparticles. See DOI: 10.1039/b927355g

Fig. 1 Schematic showing the thermomorphic nature of fluorous and hydrocarbon solvents. (Note that colors of different phase are given for visualization purpose only).

nanoparticles of metal chalcogenides such as CdSe, CdS, PbSe, ZnSe, of metal oxides such as γ-Fe$_2$O$_3$ and ZnO and of bimetallic FePt.

A TEM image of perfluorodecanethiol-capped CdSe nanoparticles dispersed in perfluorohexane obtained by the procedure reported in the synthesis part† is shown in the Fig. 2a. The TEM image shows a narrow size distribution of nanoparticles, the average diameter of nanoparticles being around 4 nm. The photograph shown as an inset of Fig. 2a reveals a reddish brown solution of the fluorous-capped CdSe nanoparticles in the perfluorohexane layer. Fig. 3a shows the UV-visible absorption spectrum and the photoluminescence spectrum of the 4 nm CdSe nanoparticles. The absorption spectrum shows a band at 545 nm and the PL spectrum shows a band at 554 nn (excitation at 430 nm) characteristic of the 4 nm particles.[5] The narrow PL band reflects the nearly monodisperse nature of the sample. The absorption and PL bands of the CdSe nanoparticles are red-shifted due to the highly nonpolar nature of the perfluorohydrocarbon.
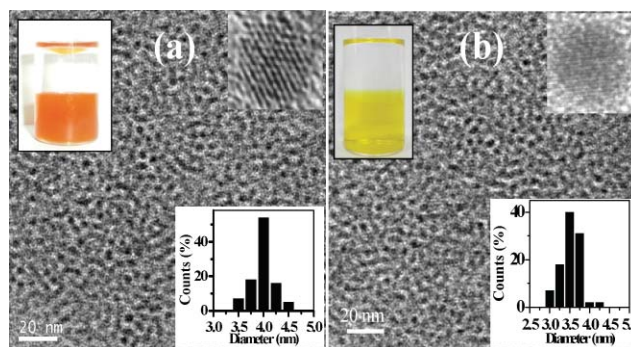

Fig. 2 TEM images of (a) 4 nm CdSe and (b) 3.5 nm CdS nanoparticles with size distribution histograms as inset. Photographs of the dispersions of the nanoparticles in PFC are also given as insets. HRTEM images are also shown as insets.
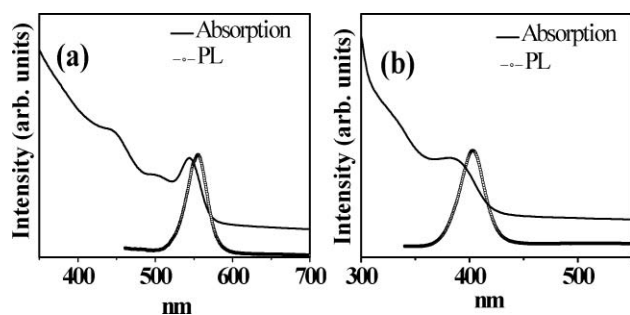
Fig. 3 UV-visible absorption and photoluminescence spectra of (a) 4 nm CdSe and (b) 3.5 nm CdS nanoparticles.

A TEM image of CdS nanoparticles capped with perfluorode-canethiol, prepared by a procedure similar to that of CdSe‡ is shown in Fig. 2b. The average diameter of the nanoparticles is around 3.5 nm. The photograph of the solution in perfluorohexane in the inset of Fig. 2b reveals the yellow color of the dispersion. The UV-visible absorption spectrum and the PL spectrum of the CdS nanoparticles are shown in Fig. 3b. The absorption spectrum, characteristic of 3.5 nm CdS particles, shows a band at 395 nm while the PL spectrum shows a band at 403 nm (excitation at 320 nm).[6]

We have obtained 12.5 nm PbSe and 5 nm ZnSe nanoparticles by employing a procedures similar to those for the Cd chalcogenide nanoparticles.‡ The absorption spectrum of the PbSe nanoparticles shows a first exciton peak around 1680 nm.[7] The UV-visible absorption spectrum of the 5 nm ZnSe nanoparticles shows a band at 400 nm and a photoluminescence band at 407 nm.[8]

By the thermal decomposition of $Fe(CO)_5$, we have obtained perfluorodecanoic acid-capped γ-Fe_2O_3 dispersed in perfluorohexane.‡ A TEM image of the nanoparticles is shown in Fig. 4(a). The as prepared γ-Fe_2O_3 nanoparticles are monodisperse
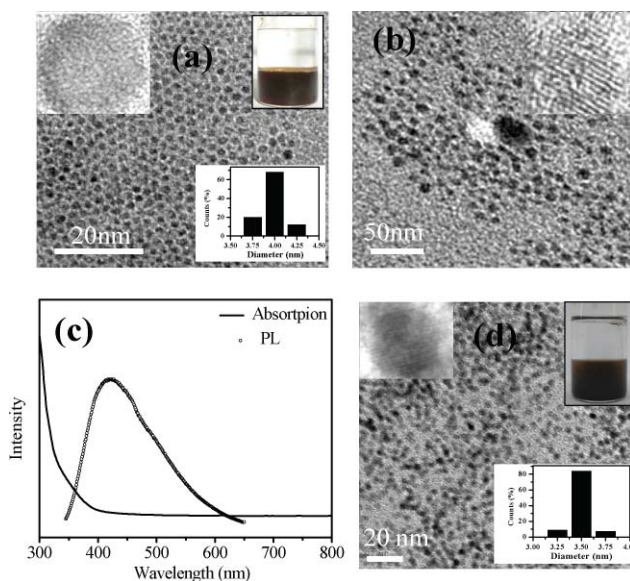

Fig. 4 (a) TEM image of 4 nm γ-Fe_2O_3. (b) TEM and (c) UV-visible absorption and photoluminescence spectra of 8 nm ZnO nanoparticles. (d) TEM image of 3.5 nm FePt nanoparticles. Photographs of the dispersions of the nanoparticles in PFC are also given as insets in PFC are given as insets in (a) and (d). HRTEM images are also shown as insets.

with a diameter around 4 nm. Magnetic susceptibility measurements show divergence between field-cooled (FC) and zero field-cooled (ZFC) measurements with a blocking temperature of 23 K (at 100 Oe) as shown in the Fig. 5(a).[9] Below the blocking temperature, the particles show magnetic hysteresis.
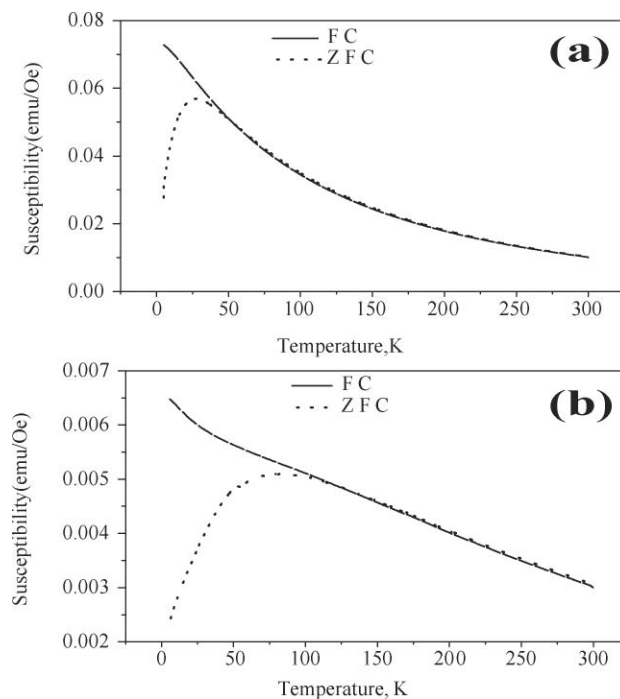

Fig. 5 Zero-field cooled (ZFC) and field cooled (FC) magnetic susceptibility data as a function of temperature for (a) Fe_2O_3 and (b) FePt nanoparticles.

Heptadecafluorodecylamine-capped ZnO nanoparticles were prepared by the nonhydrolytic decomposition of zinc acetyl acetonate.‡ In Fig. 4b we show a TEM image of ZnO nanoparticles with an average diameter of 8 nm dispersed in perfluorohexane. The UV-visible absorption spectrum in Fig. 4c shows an absorption band edge around 330 nm.[10] The PL spectrum shows a broad blue-green emission band at above 430 nm. A broad blue-green emission band above 430 nm is attributed to a singly charged oxygen vacancy, which results from the recombination of a photogenerated hole with a charge state of the specific defect, such as oxygen vacancies, or resulted from the surface deep traps.

In Fig. 4d, we show a TEM image of 3.5 nm Heptadeca-fluorodecylamine-capped FePt nanoparticles.‡ FePt nanoparticles show superparamagnetic behavior at room temperature and divergence between FC and ZFC measurements with a blocking temperature of 75 K (at 100 Oe) as shown in Fig. 5(b) in agreement with the literature value.[11] The particles show magnetic hysteresis below the blocking temperature.

All the nanoparticles were characterized by X-ray diffraction (see Figs. S1 and S2 in the electronic supplementary information, ESI†). The patterns of CdSe, CdS and ZnSe were indexed on the cubic zinc blende structure where as PbSe was indexed on the rock salt structure. The XRD pattern of iron oxide was indexed as magahmite. The FePt nanoparticles show XRD patterns corresponding to the FCC structure where as ZnO nanoparticles had the wurtzite structure

In conclusion, it has been possible to synthesize pure fluorous-capped inorganic nanoparticles by a one step procedure. This procedure conveniently uses the fact that hydrocarbons and perfluorohydrocarbons become fully miscible at high temperatures. This feature has enabled us to extract fluorous-capped inorganic nanoparticles in perfluorohydrocarbons, having prepared them in mixture of hydrocarbon and perfluorohydrocarbon at high temperatures. It is noteworthy that the nanoparticles are nearly monodisperse and highly pure. The purity is assured because only the nanoparticles which are capped by the fluorous label get extracted by the fluorocarbon. The fluorous label gets attached to only the desired products in the synthesis. The method can be used for the synthesis of variety of fluorous-capped inorganic nanostructures dispersed in perfluorohydrocarbons.

Notes and references

‡ Synthesis: The synthetic procedure involves first taking appropriate metal precursors and other reagents in a hydrocarbon solvent such as toluene. To this mixture, the required quantity of the fluorous label (which caps the product) is added along with perfluorohexane. The reaction is carried out under solvothermal or refluxing conditions. We have used perfluorodecanethiol as the capping agent for metal chalcogenides, heptadecafulorodecylamine for ZnO, and perfluorodecanoic acid for γ-Fe_2O_3 and FePt.

In a typical procedure to prepare fluorous-capped metal chalcogenides (CdSe, CdS, PbSe and ZnSe), the metal cupferronate or acetylacetonate (0.07 mmol) is taken along with selenium or sulfur (0.07 mmol), tetralin (7.5 μL) and a small quantity of perfluorodecanethiol (200 μL) in a mixture of 10 ml toluene and 10 ml perfluorohexane.[12] The reaction mixture which was biphasic at room temperature was sealed in a stainless steel 30 ml teflon-lined autoclave and placed in an air oven preheated to 250 °C for 5 h. After the reaction was complete, the autoclave was allowed to cool to room temperature and the contents were then transferred to a vial. The resulting product consisted of two layers with the perfluorodecanethiol-capped nanoparticles present in the perfluorohexane layer (Fig. 1).

Synthesis of fluorous-capped γ-Fe_2O_3 nanoparticles was carried out by the following procedure.[9] Around 0.2 ml of $Fe(CO)_5$ (1.5 mmol) was added to a mixture of 10 ml of dioctyl ether, 10 ml of perfluorohexane and 1 g of perfluorodecanoic acid at 100 °C. The resulting mixture was heated to 250 °C and kept at that temperature for 2 h. During this time, the initial orange color turned black. The reaction mixture was allowed to cool to room temperature. The iron nanoparticles in perfluorohexane upon exposure to air got oxidized to γ-Fe_2O_3 nanoparticles.

Fluorous-capped ZnO nanoparticles[10] were prepared starting with a mixture of 7.5 mg of $Zn(acac)_2$ with 150 mg of heptadecafluorodecylamine in the presence of 7.5 ml toluene and 10 ml perfluorohexane. The mixture was sealed in a stainless steel 25 ml teflon-lined autoclave placed for 20 h in an air oven preheated to 250 °C. On cooling, ZnO nanoparticles capped with heptadecafluorodecylamine dispersed in the denser fluorocarbon medium were obtained.

Fluorous-capped FePt nanoparticles were prepared as follows.[11] Under a flow of nitrogen, $Pt(acac)_2$ (0.5 mmol) was mixed with benzyl ether (10 ml) and heated to 100 °C. To this mixture, $Fe(CO)_5$ (1 mmol), heptadecafluorodecylamine (5 mmol, 500 μL) perfluorodecanoic acid (5 mmol) and perfluorohexane (10 ml) were added under a flow of nitrogen. The mixture was heated to 250 °C at a heating rate of ~15 °C min^{-1} to assure complete decomposition of $Fe(CO)_5$, and then mixture was refluxed for 1 h. The reaction mixture was then cooled to room temperature to obtain pure FePt particles capped with heptadecafluorodecyl amine and perfluorodecanoic acid dispersed in perfluorohexane.

All the fluorous capped nanoparticles were characterized by transmission electron microscopy (TEM) by employing a JOEL JEM 3010 instrument. Photoluminescence spectra were recorded with a Fluorolog-22(Horiba-jobin Yvon) spectrofluorometer fitted with a Xenon lamp excitation source while the absorption spectra were recorded with UV/VIS/NIR Perkin-Elmer spectrometer. Magnetic measurements were carried out with a vibrating sample magnetometer option in the Physical Properties Measuring System (PPMS, Quantum Design, USA). The samples were examined by X-ray diffraction using Cu-Kα radiation ($\lambda = 1.54056$ Å) using a Rigaku-99 instrument.

1 (a) A. Gladyz, D. P. Curran and I. T. Horvath, *Handbook of Fluorous Chemistry*, Wiley-VCH Verlag GmbH, Weinheim, Germany, 2004; (b) A. Studer, S. Hadida, S. Y. Ferrito, P. Y. Kim, P. Jeger, P. Wipf and D. P. Curran, *Science*, 1997, **275**, 823; (c) D. P. Curran, *Angew. Chem., Int. Ed.*, 1998, **37**, 1174; (d) W. Zhang, *Chem. Rev.*, 2009, **109**, 749.
2 (a) T. Yonezawa, S.-y. Onoue and N. Kimizuka, *Adv. Mater.*, 2001, **13**, 140; (b) M. Tristany, J. Courmarcel, P. Dieudonné, M. Moreno-Mañas, R. Pleixats, A. Rimola, M. Sodupe and S. Villarroya, *Chem. Mater.*, 2006, **18**, 716; (c) Y. Ofir, B. Samanta, P. Arumugan and V. M. Rotello, *Adv. Mater.*, 2007, **19**, 4075; (d) A. Das, R. Guo, J. B. Tracy, R. Balasubramanian, A. D. Douglas and R. W. Murray, *Langmuir*, 2008, **24**, 310; (e) M. Mugisawa and H. Sawada, *Langmuir*, 2008, **24**, 9215; (f) A. O'Donnell, K. Yach and L. Reven, *Langmuir*, 2008, **24**, 2465.
3 R. Voggu, K. Biswas, A. Govindaraj and C. N. R. Rao, *J. Phys. Chem. B*, 2006, **110**, 20752.
4 K. Biswas and C. N. R. Rao, *J. Colloid Interface Sci.*, 2009, **333**, 404.
5 B. K. H. Yen, N. E. Stott, K. F. Jensen and M. G. Bawendi, *Adv. Mater.*, 2003, **15**, 1858.
6 W. W. Yu and X. Peng, *Angew. Chem., Int. Ed.*, 2002, **41**, 2368.
7 J. S. Steckel, S. Coe-Sullivan, V. Bulovinc and M. G. Bawendi, *Adv. Mater.*, 2003, **15**, 1862.
8 M. A. Hines and P. Guyot-Sionnest, *J. Phys. Chem. B*, 1998, **102**, 3655.
9 L. E. Euliss, S. G. Grancharov, S. O'Brien, T. J. Deming, G. D. Stucky, C. B. Murray and G. A. Held, *Nano. Lett.*, 2003, **3**, 1489.
10 (a) N. Pinna, G. Garnweitner, M. Antonietti and M. Niederberger, *J. Am. Chem. Soc.*, 2005, **127**, 5608; (b) Y. S. Fu, X. W. Du, S. A. Kulinich, J. S. Qiu, W. J. Qin, R. Li, J. Sun and J. Liu, *J. Am. Chem. Soc.*, 2007, **129**, 16029.
11 M. Chen, J. P. Liu and S. Sun, *J. Am. Chem. Soc.*, 2004, **126**, 8394.
12 (a) U. K. Gautam, M. Rajamathi, F. Meldrum, P. Morgan and R. Seshadri, *Chem. Commun.*, 2001, 629; (b) U. K. Gautam, R. Seshadri and C. N. R. Rao, *Chem. Phys. Lett.*, 2003, **375**, 560.